SPRINGER BRIEFS IN APPLIED SCIENCES AND TECHNOLOGY · COMPUTATIONAL MECHANICS

Marcelo J.S. de Lemos

Thermal Non-Equilibrium in Heterogeneous Media

Springer

SpringerBriefs in Applied Sciences and Technology

Computational Mechanics

More information about this series at http://www.springer.com/series/8886

Marcelo J.S. de Lemos

Thermal Non-Equilibrium in Heterogeneous Media

Springer

Marcelo J.S. de Lemos
Departamento de Enegia—IEME
Instituto Tecnológico de Aeronáutica—ITA
São José dos Campos, São Paulo
Brazil

ISSN 2191-530X ISSN 2191-5318 (electronic)
SpringerBriefs in Applied Sciences and Technology
ISSN 2191-5342 ISSN 2191-5350 (electronic)
SpringerBriefs in Computational Mechanics
ISBN 978-3-319-14665-2 ISBN 978-3-319-14666-9 (eBook)
DOI 10.1007/978-3-319-14666-9

Library of Congress Control Number: 2015949447

Springer Cham Heidelberg New York Dordrecht London

Printed on acid-free paper

Springer International Publishing AG Switzerland is part of Springer Science+Business Media (www.springer.com)

The true sign of intelligence is not knowledge but imagination.

Albert Einstein

To my lovely wife Magaly

Preface

This is the second book of Springer Briefs in Applied Sciences and Technology, Series in Computational Mechanics by Springer, which I contribute with pleasure. As a comment for future work at the end of "Turbulent Impinging Jets into Porous Materials", ISBN 978-3-642-28276-8, Springer Briefs in Computational Mechanics, 2012, two suggestions for extending the model therein were mentioned, namely the inclusion of chemical reactions in the fluid phase and the movement of the solid phase. Following it, this book fulfills that aspiration and I hope that the material herein can be of interest to the readers.

This work is way overdue as I had in mind finishing it by the middle of last year (2014). My sincere apologies to the publishers for postponing the delivery of this manuscript as unexpected difficulties arose. As in the previous issue, here again I am thankful to Professor Dr.-Ing. Andreas Öchsner, Editor-in-Chief of the Springer book series on "Advanced Structured Materials" and Dr. Christoph Baumann, Springer Senior Engineering Editor.

Once more the continuous support from our research funding agencies in Brazil, namely, CNPq, CAPES, and FAPESP, is grealy appreciated. In this volume, most of the presented material is related to graduate research work done by my former students, in particular those conducted by Dr. M.B. Saito, Dr. A.C. Pivem, and Master graduate J.E.A. Coutinho. To them and to all my other former students who have contributed to our efforts over the last 15 years, my sincere thanks. Last but not least, I would like to express my appreciation to Mrs. Ingrid Maiara Souza Chagas for her careful and skillful typing of the manuscript.

São José dos Campos — Marcelo J.S. de Lemos
July 2015

Contents

Nomenclature

Latin Characters

A_i	Interface total area between the fluid and solid
c_F	Forchheimer coefficient
c_p	Fluid specific heat
C_ℓ	Volumetric molar concentration
c_p	Specific heat
D_ℓ	Diffusion coefficient
$\mathbf{D}_{disp}$	Mass dispersion
$\mathbf{D}_{disp,t}$	Turbulent mass dispersion
$\mathbf{D}_t$	Turbulent mass flux
Da	Darcy number, $Da = K/H^2$
D	Square rods of lateral size
$\mathbf{g}$	Gravity acceleration vector
h_i	Interfacial convective heat transfer coefficient
H	Channel height, Periodic cell height
$\mathbf{I}$	Unit tensor
$\mathbf{J}_\ell$	Mass diffusion coefficient
K	Permeability
k_f	Fluid thermal conductivity
k_s	Solid thermal conductivity
$\mathbf{K}_{disp}$	Dispersion tensor
$\mathbf{K}_{f,s}$	Thermal conductivity tensor in fluid phase
$\mathbf{K}_{s,f}$	Thermal conductivity tensor in solid phase
$\mathbf{K}_t$	Turbulence conductivity tensor
$\mathbf{K}_{disp,t}$	Turbulent dispersion tensor
k	(1) Thermal conductivity; (2) Turbulent kinetic energy per unit mass, $k = \overline{\mathbf{u}' \cdot \mathbf{u}'}/2$
$\langle k \rangle^i$	Intrinsic (fluid) average of k
k_{eff}	Effective thermal conductivity

L	Channel length
ℓ	Chemical species
m_ℓ	Mass fraction of component ℓ
M_ℓ	Molar weight of component ℓ
Nu	Nusselt number $Nu = \frac{h_i D}{k_f}$
P	Pressure
P^*	$P^* = \frac{P - P_{\min}}{P_{\max} - P_{\min}}$, Nondimensional Pressure
Pr	$Pr = \nu/\alpha$, Prandtl number
Pr_t	Turbulent Prandtl number
Pe_D	Peclet number based on D and the macroscopically uniform velocity
$\langle p \rangle^i$	Intrinsic (fluid) average of pressure p
p	Thermodynamic pressure
q_w	Integral wall heat flux
q_w^ϕ	Integral wall heat flux will porous layer
Re_D	Reynolds number based on D and the macroscopically uniform velocity
Re	Reynolds number based on the jet width, $Re = \rho\ v_0 B/\mu$
S_φ	Source term
Sc_t	Turbulent Schmidt number
T	Temperature
T_{ms}	Bulk temperature of the solid phase
T_{mf}	Bulk temperature of the fluid phase
$\mathbf{u}$	Local instantaneous velocity
u_B	Bulk velocity
$\bar{\mathbf{u}}_D$	Darcy velocity vector (volume-time average of $\mathbf{u}$)
$\mathbf{u}_\ell$	Velocity of species ℓ
$\langle \mathbf{u} \rangle^i$	Intrinsic (fluid) average of $\mathbf{u}$
x, y	Cartesian coordinates
X	$X = x/H$, Dimensionless longitudinal coordinate
Y	$Y = y/H$, Dimensionless transversal coordinate

Greek Characters

β	Thermal expansion coefficient
β_C	Salute expansion coefficient
β_ϕ	Macroscopic thermal expansion coefficient
β_{C_ϕ}	Macroscopic salute expansion coefficient
ΔV	Representative elementary volume
ΔV_f	Fluid volume inside ΔV
μ	Fluid Dynamic viscosity
μ_t	Eddy viscosity
μ_{t_ϕ}	Macroscopic eddy viscosity
ν	Fluid kinematic viscosity

ρ	Bulk density of fluid or mixture
ρ_ℓ	Mass density of species ℓ
θ	$\theta_{(s,f)} = \frac{T_w - T}{T_w - T_{inlet_{(s,f)}}}$, Dimensionless local temperature
Θ	$\Theta_{(s,f)} = \frac{T_{m_{(s,f)}} - T_{inlet_f}}{T_{inlet_s} - T_{inlet_f}}$, Dimensionless bulk temperature
ϕ	$\phi = \Delta V_f / \Delta V$, Porosity
α	Fluid thermal diffusivity
ρ	Density
v	Kinematic viscosity
$\sigma_{t\phi}$	Macroscopic turbulent Prandtl number
ε	Dissipation rate of k
$\langle\varepsilon\rangle^i$	Intrinsic (fluid) average of ε

Special Characters, Subscripts and Superscripts

φ	General variable
$\langle\varphi\rangle^i$	Intrinsic average
w	Wall
o	Inlet conditions
$\langle\varphi\rangle^v$	Volume average
${}^i\varphi$	Spatial deviation
ϕ	Macroscopic
β	Buoyancy
B	Bulk
C	Concentration
D	Particle or rod diameter
h_i	Interfacial heat transfer coefficient
i	Intrinsic (fluid) average
v	Volume (fluid + solid) average
s,f	Solid, fluid
t	Turbulent

List of Figures

List of Tables

Overview

Often thermal equipment characterized by a solid permeable structure and a moving working fluid are used in advanced materials manufacturing and in energy production processes. The advantages of having a clearer picture of how distinct temperatures of each phase behave is beneficial to the design and optimization of engineering equipment. Or say, the ability to more accurately analyze transport processes in such devices can be of advantage in developing a more efficient and reliable thermal machinery, including gasifiers for biomass or coal, direct reduced iron (DRI) equipment for steel production, porous burners for household heating, hydrogen production reactors, moving bed based devices, and nuclear reactor core, to mention a few applications.

More specifically, this volume presents, in a self-contained fashion and organized way, a series of studies on flow and heat transfer in porous media, in which distinct energy balances are considered for the porous matrix and for the permeating fluid. Detailed mathematical modeling is presented considering both volume and time averaging operators simultaneously applied to the local instantaneous governing equations. Besides presenting a correlation for interstitial heat transfer between phases, examples of systems involving combustion in the gaseous phase, moving bed, and double-diffusion mechanism are analyzed here. Numerical results are then presented for each case. In the end, this book contains the description of a tool that might benefit engineers in developing and designing more efficient thermal equipment.

Chapter 1
Heterogeneous Media

1.1 Introduction

This book presents, in a self-contained fashion, a series of studies on flow and heat transfer in porous media, in which distinct energy balances are considered for the porous matrix and for the permeating fluid. Detailed mathematical modeling is presented considering both volume and time averaging operators simultaneously applied to the governing equations. System involving combustion in the gaseous phase, moving bed and double-diffusion mechanism are also here presented by. On the overall, this book contains the description of a tool that might be interesting to engineers in developing more efficient thermal equipment such as gasifiers (Fig. 1.1a), porous household combustors (Fig. 1.1b) and reactors for production of a hydrogen reach (Fig. 1.1c).

Accordingly, for analyzing heat transfer in porous media there are two approached to follow. One can assume thermal equilibrium between the solid matrix and the working fluid (Local Thermal Equilibrium Model—LTE), or else, one can analyze each phase with an independent energy balance equation (Local Thermal Non-equilibrium Model—LTNE). Figure 1.2a illustrates the idea of a Representative elementary volume (R.E.V.), over which volume average are obtained. If the averaging process is taken over the fluid phase, then one can obtain an average temperature $\langle T_f \rangle^i$ where the superscript "i" denotes the intrinsic average over the volume occupied by phase "i". The same reasoning applies for the solid temperature leading to $\langle T_s \rangle^i$, where the superscript "i" in this case would refer to the volume occupied by the solid matter. On the other hand, if properties values also present a fluctuation with time, the employment of statistical tools can be used to find time-mean values over an interval of time Δt (Fig. 1.2b). In this case, an overbar commonly used in the literature to represent time averaging would result in $\langle \bar{T}_f \rangle^i$ and $\langle \bar{T}_s \rangle^i$ (see for example [1] for details). In the literature, thermal equilibrium is assumed when $\langle \bar{T}_f \rangle^i \approx \langle \bar{T}_s \rangle^i \approx \langle \bar{T} \rangle^i$, or say, when the time-volume average value for temperature on each phase does not differ substantially from the other.

M.J.S. de Lemos, *Thermal Non-Equilibrium in Heterogeneous Media*,
SpringerBriefs in Computational Mechanics,
DOI 10.1007/978-3-319-14666-9_1

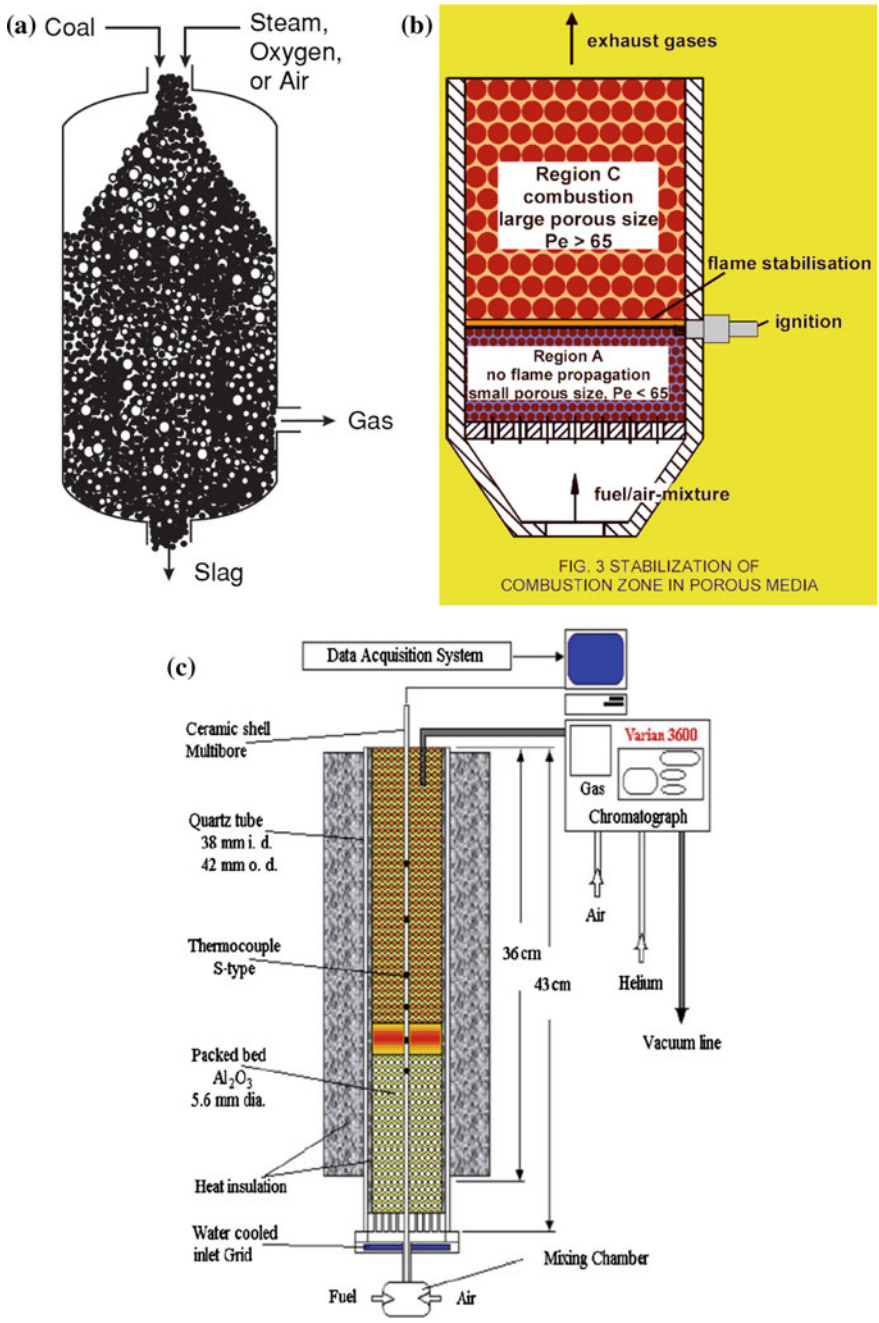

Fig. 1.1 Applications of heterogeneous media modeling: **a** Gasifiers. **b** Porous Combustors. **c** Hydrogen reactors

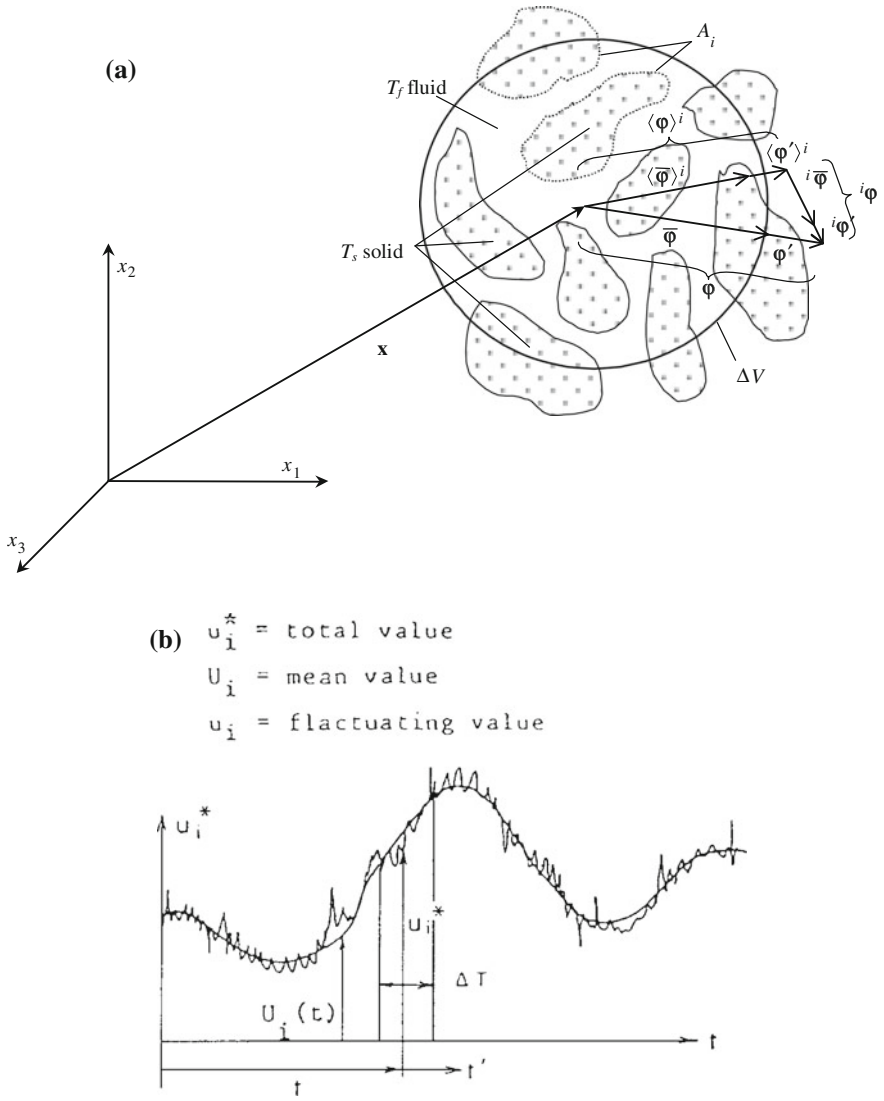

Fig. 1.2 Averaging operators: **a** Volume average over a representative elementary volume (R.E. V.). **b** Time averaging over an interval of time Δt (see [15])

However, the hypothesis of local thermal equilibrium (LTE) demands several constraints that have been considered by a number of authors [2–7]. For instance, the LTE hypothesis is no longer valid when the particles or pores are not small enough, when the thermal properties differ widely, or when convective transport is not important. Also, most recent papers on the effects of local thermal non-equilibrium deal with unsteady situations [8, 9], which are here not considered.

Further, when there is a significant heat generation in any of the phases, the system will rapidly depart from the local thermal equilibrium condition [10]. For such extreme conditions, the one-energy equation model (LTE) is inadequate to correctly describe both the transients associated with the quench front penetrating the hot dry porous layer, as well as regions where dry out occurs.

As mentioned, when the assumption of local thermal equilibrium fails, one possible solution is to develop separate transport equations for each phase [11–13] and this leads to macroscopic models, which are referred to in the literature as LTNE closures. For heat transport through a porous medium, a LTNE model involves the derivation of energy equation for both the solid and the fluid, which, in turn, requires additional information on the interfacial heat transfer coefficient between the fluid phase and the solid phase [14, 15]. For that, the use of LTNE models is, overall, more involving [16].

Important applications on the LTNE model are found in analyses of advanced materiais manufacturing and in renewable energy productions processes, such as in modern steel production and biomass gasification in fixed and moving bed configurations. With respect to pelletization of iron ore, Parisi and Laborde [17] and Negri et al. [18] presented a study about the direct reduction of iron oxide in a countercurrent reactor in a moving bed. Also within this context, Valipour et al. [19] developed a mathematical model to simulate grain kinetics and thermal behavior of a pellet of porous iron oxide. Their study considered chemical reactions with a mixture of hydrogen, carbon monoxide, carbon dioxide and water vapor. Further, Valipour et al. [20] presented a mathematical model to simulate the multiple heterogeneous reactions in a moving bed of porous pellets on a reactor. Valipour et al. [21] described a model to predict flow in a cylindrical reactor in which pellets of iron ore went through a gas mixture.

In advanced manufacturing, Henda and Falcioni [22] described the thermal performance of a pre-heater that consists of a moving bed of pellets of nickel in concurrent flow with a gas, using both one and two equations energy models.

Further, biomass pelletization and preparation for energy production may be considered as a system having a moving porous bed. Examples are given by Ryu et al. [23], Boman et al. [24] and Shimizu et al. [25], who presented mathematical models of the gasification a system using a moving bed in the burning of biomass. Already Kayal and Chakravarty [26], Rogel et al. [27] and Nussbaumer et al. [28] investigated technologies to cope with the problem of pollutant emission during of combustion and co-combustion of biomass. Other basic studies on reactive flow in fluidized beds can be found in the literature [29–31].

For thermal analysis of non-reacting systems, Nakayama et al. [32] presented the exact solution of different energy equations, for solid and fluid phases, for cases of engineering interest. They included in their study heat transfer analyses for one-dimensional porous plate with internal heat generation and thermally developing unidirectional flow through a semi-infinite porous medium. Such two-energy equation model has been investigated by a number of authors and is based on the

idea that under certain conditions the two phases, namely the solid and the fluid, cannot have their temperatures considered to be equal and, as such, they need be evaluated using distinct transport equations [33–35].

1.2 Outline of This Book

In this book, a macroscopic model for heat transfer in porous media is proposed in Chap. 2. For closing the model, we present a correlation for interstitial heat transfer obtained after integrating distributed numerical values in a unit cell, which here represents an infinite porous medium. Then, we consider the plug flow of an incompressible fluid in a two-dimensional channel fitted with porous material. Several cases are investigated in Chap. 2, including heat transfer through a fixed porous bed (Fig. 1.3a). In this configuration, the solid phase remains still while the working fluid is pumped through the permeable medium.

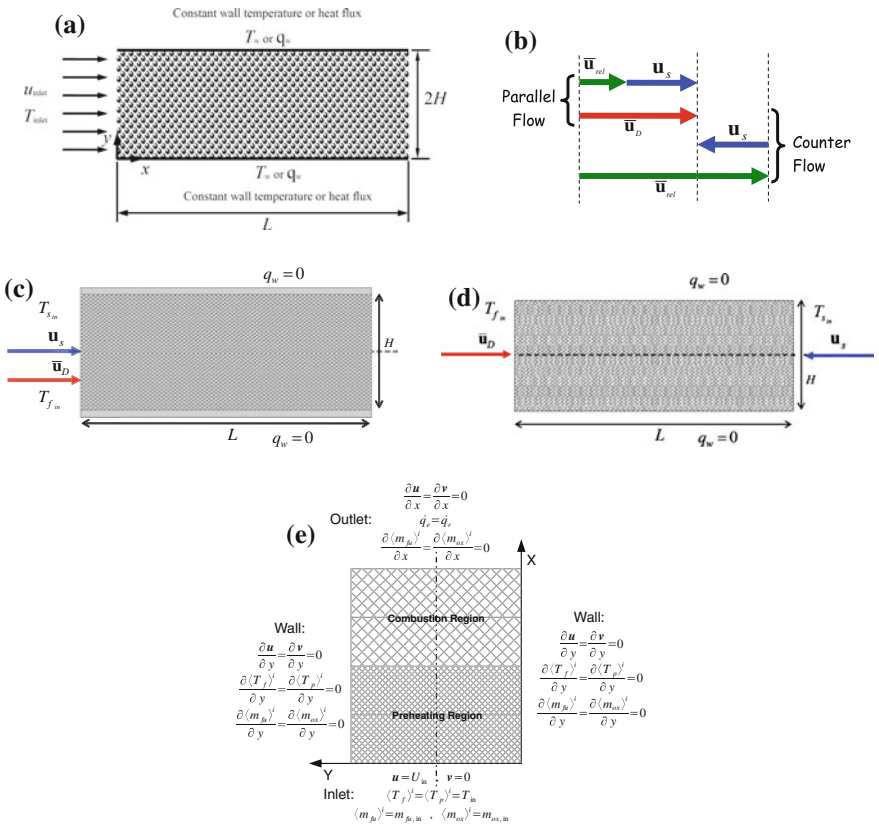

Fig. 1.3 Flow configurations. Two-dimensional channel flow: **a** Fixed bed. **b** Relative velocity. **c** Parallel flow. **d** Counter Flow. One-dimensional combustors: **e** Boundary conditions

Also include in this book are cases where the movement of the solid phase in relation to that of the fluid is considered, as will be seen in Chap. 3. The additional drag forces on the mean flow and extra term on the turbulent kinetic energy equation with depend on the relative velocity between the two phases (Fig. 1.3b). When both the fluid and solid move in the same direction, such configuration is here recalled "parallel flow" (Fig. 1.3c) whereas for the case when both phases move against each other such configuration is here named "counter flow" (Fig. 1.3d).

An important extension of the general model detailed in [1] is presented in Chap. 4, where exothermic chemical reactions are considered in the fluid phase. Such numerical results allow for the determination of temperature levels for the so-called "filtration combustion" systems. A schematic of systems envolving chemical reaction is presented in Fig. 1.3e.

Finally, double-diffusion effects are included and discussed in Chap. 5, which considers the change in the weight of a mixture by both the temperature drive (lighter hotter fluid) or mass drive (lighter of heavier mixture component).

References

1. Saito MB, de Lemos MJS (2010) A macroscopic two-energy equation model for turbulent flow and heat transfer in highly porous media. Int J Heat Mass Transf 53(11–12):2424–2433
2. Schumann TEW (1929) Heat transfer: liquid flowing through a porous prism. J Frankl Inst 208:405–416
3. Vafai K, Sozen M (1990) Analysis of energy and momentum transport for fluid flow through a porous bed. J Heat Transf 112:690–699
4. Amiri A, Vafai K (1994) Analysis of dispersion effects and nonthermal equilibrium, non-Darcian, variable porosity incompressible flow through porous media. Int J Heat Mass Transf 30:939–954
5. Whitaker S (1991) Improved constraints for the principle of local thermal equilibrium. Ind Eng Chem Res 30:983–997
6. Quintard M, Whitaker S (1993) One- and two-equation models for transient diffusion processes in two-phase systems. In: Advances in Heat Transfer,vol 23. Academic Press, New York, pp 369–464
7. Quintard M, Whitaker S (1995) Local thermal equilibrium for transient heat conduction: theory and comparison with numerical experiments. Int J Heat Mass Transf 38:2779–2796
8. Hsu CT (1999) A closure model for transient heat conduction in porous media. J Heat Transf 121:733–739
9. Sözen M, Vafai K (1990) Analysis of the non-thermal equilibrium condensing flow of a gas through a packed bed. Int J Heat Mass Transf 33(6):1247–1261
10. Kaviany M (1995) Principles of heat transfer in porous media, 2nd edn. Springer, New York
11. Quintard M (1998) Modeling local non-equilibrium heat transfer in porous media. In: Proceedings of the 11th international heat transfer conference, Kyongyu, Korea, vol 1, pp 279–285
12. Ingham DB, Pop I (1998) Transport phenomena in porous media. Elsevier, Amsterdam, pp 103–129
13. Quintard M, Kaviany M, Whitaker S (1997) Two-medium treatment of heat transfer in porous media: numerical results for effective properties. Adv Water Resour 20:77–94
14. Wakao N, Kaguei S, Funazkri T (1979) Effect of fluid dispersion coefficients on particle-to-fluid heat transfer coefficients in packed bed. Chem Eng Sci 34:325–336

15. Kuwahara F, Shirota M, Nakayama A (2001) A numerical study of interfacial convective heat transfer coefficient in two-energy equation model for convection in porous media. Int J Heat Mass Transf 44:1153–1159
16. Saito MB, de Lemos MJS (2005) Interfacial heat transfer coefficient for non-equilibrium convective transport in porous media. Int Commun Heat Mass Transf 32(5):667–677
17. Parisi DR, Laborde MA (2004) Modeling of counter current moving bed gas-solid reactor used in direct reduction of iron ore. Chem Eng J 104:35–43
18. Negri ED, Alfano OM, Chiovetta MG (1991) Direct redution of hematite in a moving-bed reactor: analysis of the water gas shift reaction effects on the reactor behavior. Am Chem Soc 30:474–482
19. Valipour MS, Hashemi MYM, Saboohi Y (2006) Mathematical modeling of the reaction in an iron ore pellet using a mixture of hydrogen, water vapor, carbon monoxide and carbon dioxide: an isothermal study. Adv Powder Technol 17(3):277–295
20. Valipour MS, Saboohi Y (2007) Modeling of multiple noncatalytic gas-solid reactions in a moving bed of porous pellets based on finite volume method. Heat Mass Transf 43(9):881–894
21. Valipour MS, Saboohi Y (2007) Numerical investigation of nonisothermal reduction Hematite using Syngas: the shaft scale study. Model Simul Mater Sci Eng 15:487–507
22. Henda R, Falcioni DJ (2006) Modeling of heat transfer in a moving packed bed: case of the preheater in nickel carbonyl process. J Appl Mech—ASME 73(1):47–53
23. Ryu C, Yang YB, Khor A, Yates NE, Sharifi VN, Swithenbank J (2006) Effect of fuel properties on biomass combustion: part i. experiments—fuel type, equivalence ratio and particle size. Fuel 85:1039–1046
24. Boman C, Nordin A, Thaning L (2003) Effects of increased biomass pellet combustion on ambient air quality in residential areas—a parametric dispersion modeling study. Biomass Bioenergy 25:465–474
25. Shimizu T, Han J, Choi S, Kim L, Kim H (2006) Fluidized-bed combustion characteristics of cedar pellets by using an alternative bed material. Energy Fuels 20:2737–2742
26. Kayal TK, Chakravarty M (1994) Mathematical modeling of continuous updraft gasification of bundled jute stick—a low ash content woody biomass. Bioresour Technol 49(1):61–73
27. Rogel A, Aguillón J (2006) The 2D Eulerian approach of entrained flow and temperature in a biomass stratified downdraft gasifier. Am J Appl Sci 3(10):2068–2075
28. Nussbaumer T (2003) Combustion and co-combustion of biomass: fundamentals, technologies, and primary measures for emission reduction. Energy Fuels 17:1510–1521
29. Li SY, Bie RS (2006) Modeling the reaction of gaseous HCl with CaO in fluidized bed. Chem Eng Sci 61(16):5468–5475
30. Zhao J, Huang J, Wu J, Fang Y, Wang Y (2008) Modeling and optimization of the moving granular packed bed for combined hot gas desulfurization and dust removal. Powder Technol 180:2–8
31. Baron J, Bulewicz EM (2006) The combustion of polymer pellets in a bubbling fluidized bed. Fuel 85:2494–2508
32. Nakayama A, Kuwahara F, Sugiyama M, Xu G (2001) A two energy equation model for conduction and convection in porous media. Int J Heat Mass Transf 44:4375–4379
33. Quintard M (1998) Modeling local non-equilibrium heat transfer in porous media. In: Proceedings of the eleventh international heat transfer conference, vol 1, pp 279–285
34. Kaviany M (1995) Principles of heat transfer in porous media, 2nd edn. Springer, New York, pp 391–424
35. Hsu CT (1999) A closure model for transient heat conduction in porous media. J Heat Transf 121:733–739

Chapter 2
Modeling of Thermal Non-equilibrium

2.1 Introduction

Convection heat transfer in porous media has been extensively investigated due to its many important engineering applications. The wide applications available have led to numerous investigations in this area. Such applications can be found in solar receiver devices, building thermal insulation, heat exchangers, energy storage units, etc. From the point of view of the energy equation there are two different models, local thermal equilibrium model and two energy approach. The first model assumes that the solid temperature is equal to the fluid temperature, thus local thermal equilibrium between the fluid and the solid-phases is achieved at any location in the porous media. This model simplifies theoretical and numerical research, but the assumption of local thermal equilibrium between the fluid and the solid is inadequate for a number of problems [1, 2]. In recent years more attention has been paid to the local thermal non-equilibrium model and its use has increased in theoretical and numerical research for convection heat transfer processes in porous media [3, 4]. Saito and de Lemos [5] considered local thermal non-equilibrium and obtained the interfacial heat transfer coefficient for laminar flow using a single unit cell with local instantaneous transport equations.

This chapter details the proposition of a new correlation for obtaining the interfacial heat transfer coefficient for turbulent flow in a packed bed. The bed is modeled as an infinite staggered array of square rods and the range of Reynolds number, based on the size of the rod, is extended up to 10^7. In-line rod arrangement is here not considered as the objective of this work is first to consolidate results for staggered arrays. Future investigations shall consider different array arrangements as well as distinct rod shapes, such as elliptical and circular rods.

The next sessions details the basic mathematical model, including the mean and turbulent fields for turbulent flows. Although the discussion of turbulent motion in porous media isn't present in this work the definition and concept to calculating the interfacial heat transfer coefficient for macroscopic flows are presented.

M.J.S. de Lemos, *Thermal Non-Equilibrium in Heterogeneous Media*,
SpringerBriefs in Computational Mechanics,
DOI 10.1007/978-3-319-14666-9_2

2.2 Governing Equations

2.2.1 Local Instantaneous Transport Equations

Microscopic transport equations or local time-averaged transport equations for incompressible fluid flow in a rigid homogeneous porous medium have been already presented in the literature and for that, they are here just presented [6]. The governing equations for the flow and energy for an incompressible fluid are given by:

$$\text{Continuity: } \nabla \cdot \mathbf{u} = 0. \tag{2.1}$$

$$\text{Momentum: } \rho\left[\frac{\partial \mathbf{u}}{\partial t} + \nabla \cdot (\mathbf{u}\mathbf{u})\right] = -\nabla p + \mu \nabla^2 \mathbf{u}. \tag{2.2}$$

$$\text{Energy-Fluid Phase: } \left(\rho c_p\right)_f \left\{\frac{\partial T_f}{\partial t} + \nabla \cdot \left(\mathbf{u} T_f\right)\right\} = \nabla \cdot \left(k_f \nabla T_f\right) + S_f. \tag{2.3}$$

$$\text{Energy-Solid Phase(Porous Matrix)} : \left(\rho c_p\right)_s \frac{\partial T_s}{\partial t} = \nabla \cdot \left(k_s \nabla T_s\right) + S_s. \tag{2.4}$$

where the subscripts f and s refer to fluid and solid phases, respectively. Here, T is the temperature k_f is the fluid thermal conductivity, k_s is the solid thermal conductivity, c_p is the specific heat and S is the heat generation term. If there is no heat generation either in the solid or in the fluid, one has further $S_f = S_s = 0$.

For turbulent flows, the standard time averaged transport equations can be written as:

$$\text{Continuity: } \nabla \cdot \bar{\mathbf{u}} = 0. \tag{2.5}$$

$$\text{Momentum: } \rho_f[\nabla \cdot (\bar{\mathbf{u}}\bar{\mathbf{u}})] = -\nabla \bar{p} + \nabla \cdot \left\{\mu\left[\nabla \bar{\mathbf{u}} + (\nabla \bar{\mathbf{u}})^T\right] - \rho \overline{\mathbf{u}'\mathbf{u}'}\right\}. \tag{2.6}$$

where the low and high Reynolds $k - \varepsilon$ model is used to obtain the eddy viscosity, μ_t, whose equations for the turbulent kinetic energy per unit mass and for its dissipation rate read:

Turbulent kinetic energy per unit mass:

$$\rho_f[\nabla \cdot (\bar{\mathbf{u}}k)] = \nabla \cdot \left[\left(\mu + \frac{\mu_t}{\sigma_k}\right)\nabla k\right] - \rho \overline{\mathbf{u}'\mathbf{u}'} : \nabla \bar{\mathbf{u}} - \rho\varepsilon \tag{2.7}$$

Turbulent kinetic energy per unit mass dissipation rate:

$$\rho_f[\nabla \cdot (\bar{\mathbf{u}}\varepsilon)] = \nabla \cdot \left[\left(\mu + \frac{\mu_t}{\sigma_\varepsilon}\right)\nabla \varepsilon\right] + \left[c_1\left(-\rho \overline{\mathbf{u}'\mathbf{u}'} : \nabla \bar{\mathbf{u}}\right) - c_2 f_2 \rho\varepsilon\right]\frac{\varepsilon}{k} \tag{2.8}$$

Reynolds stresses and the Eddy viscosity is given by, respectively:

$$-\rho\overline{\mathbf{u}'\mathbf{u}'} = \mu_t\left[\nabla\bar{\mathbf{u}} + (\nabla\bar{\mathbf{u}})^T\right] - \frac{2}{3}\rho k\mathbf{I} \tag{2.9}$$

$$\mu_t = \rho c_\mu f_\mu \frac{k^2}{\varepsilon} \tag{2.10}$$

where, ρ is the fluid density, p is the pressure, μ represents the fluid viscosity.

In the above equation set σ_k, σ_ε, c_1, c_2, and c_μ are dimensionless constants whereas f_2 and f_μ are damping functions of the low Re $k-\varepsilon$ turbulence models is justified by the fact that the turbulent flow in porous media occurs for Reynolds number relatively low. To account for the low Reynolds effects, the following damping functions were adopted.

$$f_\mu = \left\{1 - \exp\left[-\frac{(v\varepsilon)^{0.25}y}{14\,v}\right]\right\}^2 \left\{1 + \frac{5}{(k^2/v\varepsilon)^{0.75}}\exp\left[-\left(\frac{(k^2/v\varepsilon)}{200}\right)^2\right]\right\} \tag{2.11}$$

$$f_2 = \left\{1 - \exp\left[-\frac{(v\varepsilon)^{0.25}y}{3.1\,v}\right]\right\}^2 \left\{1 - 0.3\exp\left[-\left(\frac{(k^2/v\varepsilon)}{6.5}\right)^2\right]\right\} \tag{2.12}$$

where y is the coordinate normal to the wall. The turbulent model constants are given as follows,

$c_\mu = 0.09$, $c_1 = 1.5$, $c_2 = 1.9$, $\sigma_k = 1.4$, $\sigma_\varepsilon = 1.3$.

For the high Re model the standard constants of Launder and Spalding [7] were emplyed.

Also, the time averaged energy equations become:

$$\text{Energy-Fluid Phase: } (\rho c_p)_f\left[\nabla\cdot\left(\bar{\mathbf{u}}\bar{T}_f\right)\right] = \nabla\cdot\left(k_f\nabla\bar{T}_f\right) - (\rho c_p)_f\nabla\cdot\left(\overline{\mathbf{u}'T_f'}\right). \tag{2.13}$$

$$\text{Energy-Solid Phase (Porous Matrix): } \nabla\cdot\left(k_s\nabla\bar{T}_s\right) + S_s = 0. \tag{2.14}$$

2.2.2 *Double-Decomposition of Variables*

Macroscopic transport equations for turbulent flow in a porous medium are obtained through the simultaneous application of time and volume average operators over a generic fluid property φ. Such concepts are defined as [8–10].

$$\bar{\varphi} = \frac{1}{\Delta t}\int_{t}^{t+\Delta t} \varphi dt, \quad \text{with} \quad \varphi = \bar{\varphi} + \varphi' \tag{2.15}$$

for time splitting, as used in Eqs. (2.14)–(2.22), and

$$\langle\varphi\rangle^{i} = \frac{1}{\Delta V_f}\int\limits_{\Delta V_f} \varphi dV; \quad \langle\varphi\rangle^{v} = \phi\langle\varphi\rangle^{i}; \quad \phi = \frac{\Delta V_f}{\Delta V}, \quad \text{with} \quad \varphi = \langle\varphi\rangle^{i} + {}^{i}\varphi \tag{2.16}$$

for volume splitting, where ΔV_f is the volume of the fluid contained in a Representative Elementary Volume ΔV (REV, see Fig. 1.2a). Intrinsic average (fluid-based) and volume average (fluid-plus-soid-based) are represented, respectively, by $\langle\ \rangle^{i}$ and $\langle\ \rangle^{v}$. The double decomposition idea, introduced and fully described in [8–10], combines Eqs. (2.15) and (2.16) and can be summarized as:

$$\overline{\langle\varphi\rangle^{i}} = \langle\bar{\varphi}\rangle^{i}; \quad {}^{i}\bar{\varphi} = \overline{{}^{i}\varphi}; \quad \langle\varphi'\rangle^{i} = \langle\varphi\rangle^{i'} \tag{2.17}$$

and,

$$\left.\begin{array}{l}\varphi' = \langle\varphi'\rangle^{i} + {}^{i}\varphi' \\ {}^{i}\varphi = \overline{{}^{i}\varphi} + {}^{i}\varphi'\end{array}\right\} \quad \text{where} \quad {}^{i}\varphi' = \varphi' - \langle\varphi'\rangle^{i} = {}^{i}\varphi - \overline{{}^{i}\varphi} \tag{2.18}$$

therefore, the general vector quantity φ can be expressed by either,

$$\varphi = \overline{\langle\varphi\rangle^{i}} + \langle\varphi\rangle^{i'} + \overline{{}^{i}\varphi} + {}^{i}\varphi' \tag{2.19}$$

or

$$\varphi = \langle\bar{\varphi}\rangle^{i} + {}^{i}\bar{\varphi} + \langle\varphi'\rangle^{i} + {}^{i}\varphi'. \tag{2.20}$$

The term ${}^{i}\varphi'$ can be viewed as either the temporal fluctuation of the spatial deviation or the spatial deviation of the temporal fluctuation of the quantity φ.

2.2.3 Macroscopic Flow Equations

When the average operators (2.15) and (2.16) are simultaneously applied over Eqs. (2.1) and (2.2), macroscopic equations for turbulent flow are obtained. Volume integration is performed over a Representative Elementary Volume (REV) [11, 12], resulting in,

$$\text{Continuity: } \nabla \cdot \bar{\mathbf{u}}_D = 0. \tag{2.21}$$

where, $\bar{\mathbf{u}}_D = \phi \langle \bar{\mathbf{u}} \rangle^i$ and $\langle \bar{\mathbf{u}} \rangle^i$ identifies the intrinsic average of the time-averaged velocity vector $\bar{\mathbf{u}}$.

Momentum:

$$\begin{aligned} \rho \left[\frac{\partial \bar{\mathbf{u}}_D}{\partial t} + \nabla \cdot \left(\frac{\bar{\mathbf{u}}_D \bar{\mathbf{u}}_D}{\phi} \right) \right] = & -\nabla(\phi \langle \bar{p} \rangle^i) + \mu \nabla^2 \bar{\mathbf{u}}_D - \nabla \cdot (\rho \phi \langle \overline{\mathbf{u}'\mathbf{u}'} \rangle^i) \\ & - \left[\frac{\mu \phi}{K} \bar{\mathbf{u}}_D + \frac{c_F \phi \rho \, |\bar{\mathbf{u}}_D| \bar{\mathbf{u}}_D}{\sqrt{K}} \right] \end{aligned} \tag{2.22}$$

where the last two terms in Eq. (2.2) represent the Darcy and Forchheimer or form drags. The symbol K is the porous medium permeability, c_F is the form drag or Forchheimer coefficient, $\langle \bar{p} \rangle^i$ is the intrinsic average pressure of the fluid and ϕ is the porosity of the porous medium.

The macroscopic Reynolds stress, $-\rho \phi \langle \overline{\mathbf{u}'\mathbf{u}'} \rangle^i$, appearing in Eq. (2.22) is given as,

$$-\rho \phi \langle \overline{\mathbf{u}'\mathbf{u}'} \rangle^i = \mu_{t_\phi} 2 \langle \bar{\mathbf{D}} \rangle^{\mathbf{v}} - \frac{2}{3} \phi \rho \langle k \rangle^i \mathbf{I} \tag{2.23}$$

where,

$$\langle \bar{\mathbf{D}} \rangle^v = \frac{1}{2} \left[\nabla(\phi \langle \bar{\mathbf{u}} \rangle^i) + [\nabla(\phi \langle \bar{\mathbf{u}} \rangle^i)]^T \right] \tag{2.24}$$

is the macroscopic deformation tensor, $\langle k \rangle^i = \langle \overline{\mathbf{u}' \cdot \mathbf{u}'} \rangle^i / 2$ is the macroscopic turbulent kinetic energy, and μ_{t_ϕ}, is the turbulent viscosity, which is modeled in [9] similarly to the case of clear flow, in the form,

$$\mu_{t_\phi} = \rho c_\mu \frac{\langle k \rangle^{i^2}}{\langle \varepsilon \rangle^i} \tag{2.25}$$

The intrinsic turbulent kinetic energy per unit mass and its dissipation rate are governed by the following equations,

$$\begin{aligned} \rho \left[\frac{\partial}{\partial t} \left(\phi \langle k \rangle^i \right) + \nabla \cdot \left(\bar{\mathbf{u}}_D \langle k \rangle^i \right) \right] = & \nabla \cdot \left[\left(\mu + \frac{\mu_{t_\phi}}{\sigma_k} \right) \nabla \left(\phi \langle k \rangle^i \right) \right] - \rho \langle \overline{\mathbf{u}'\mathbf{u}'} \rangle^i : \nabla \bar{\mathbf{u}}_D \\ & + c_k \rho \frac{\phi \langle k \rangle^i |\bar{\mathbf{u}}_D|}{\sqrt{K}} - \rho \phi \langle \varepsilon \rangle^i \end{aligned} \tag{2.26}$$

$$\rho\left[\frac{\partial}{\partial t}\left(\phi\langle\varepsilon\rangle^{i}\right)+\nabla\cdot\left(\bar{\mathbf{u}}_{D}\langle\varepsilon\rangle^{i}\right)\right]=\nabla\cdot\left[\left(\mu+\frac{\mu_{t_{\phi}}}{\sigma_{\varepsilon}}\right)\nabla\left(\phi\langle\varepsilon\rangle^{i}\right)\right]+c_{1}\left(-\rho\langle\overline{\mathbf{u}'\mathbf{u}'}\rangle^{i}:\nabla\bar{\mathbf{u}}_{D}\right)\frac{\langle\varepsilon\rangle^{i}}{\langle k\rangle^{i}}$$
$$+\ c_{2}c_{k}\rho\frac{\phi\langle\varepsilon\rangle^{i}\left|\bar{\mathbf{u}}_{D}\right|}{\sqrt{K}}-c_{2}\rho\phi\frac{\langle\varepsilon\rangle^{i^{2}}}{\langle k\rangle^{i}} \tag{2.27}$$

where, $\sigma_k = 1$, $\sigma_\varepsilon = 1.3$, $c_1 = 1.44$, $c_2 = 1.92$, $c_\mu = 0.09$ and $c_k = 0.28$ are non-dimensional constants [8–10].

2.2.4 Macroscopic Energy Equations

Similarly, macroscopic energy equations are obtained for both fluid and solid phases by applying time and volume average operators to Eqs. (2.3) and (2.4). As in the flow case, volume integration is performed over a Representative Elementary Volume (REV), resulting in,

$$\left(\rho c_{p}\right)_{f}\left[\frac{\partial\,\phi\langle\overline{T_{f}}\rangle^{i}}{\partial t}+\nabla\cdot\left\{\phi\left(\langle\bar{\mathbf{u}}\rangle^{i}\langle\overline{T_{f}}\rangle^{i}+\underbrace{\langle{}^{i}\bar{\mathbf{u}}^{i}\overline{T_{f}}\rangle^{i}}_{\text{thermal disperson}}+\underbrace{\overline{\langle\mathbf{u}'\rangle^{i}\langle T_{f}'\rangle^{i}}}_{\text{turbulent heat flux}}+\underbrace{\langle\overline{{}^{i}\mathbf{u}'\,{}^{i}T_{f}'}\rangle^{i}}_{\text{turbulent thermal dispersion}}\right)\right\}\right]$$
$$=\underbrace{\nabla\cdot\left[k_{f}\nabla\left(\phi\,\langle\overline{T_{f}}\rangle^{i}\right)+\frac{1}{\Delta V}\int_{A_{i}}\mathbf{n}_{i}\,k_{f}\overline{T_{f}}\,dA\right]}_{\text{conduction}}+\underbrace{\frac{1}{-}\int_{A_{i}}\mathbf{n}_{i}\cdot k_{f}\nabla\overline{T_{f}}\,dA}_{\text{interfacial heat transfer}} \tag{2.28}$$

where the expansion,

$$\langle\overline{\mathbf{u}'T_{f}'}\rangle^{i}=\langle\overline{\left(\langle\mathbf{u}'\rangle^{i}+{}^{i}\mathbf{u}'\right)\left(\langle T_{f}'\rangle^{i}+{}^{i}T'\right)}\rangle^{i}=\overline{\langle\mathbf{u}'\rangle^{i}\langle T_{f}'\rangle^{i}}+\langle\overline{{}^{i}\mathbf{u}'{}^{i}T_{f}'}\rangle^{i} \tag{2.29}$$

has been used in light of the double decomposition concept given by Eqs. (2.17)–(2.20) [8]. For the solid phase, one has,

$$(\rho c_p)_s \left\{ \frac{\partial (1-\phi)\langle \overline{T_s} \rangle^i}{\partial t} \right\} = \underbrace{\nabla \cdot \left\{ k_s \nabla \left[(1-\phi)\langle \overline{T_s} \rangle^i \right] - \frac{1}{\Delta V} \int\limits_{A_i} \mathbf{n}_i k_s \overline{T_s} dA \right\}}_{\text{conduction}} \underbrace{- \frac{1}{\Delta V} \int\limits_{A_i} \mathbf{n}_i \cdot k_s \nabla \overline{T_s} dA}_{\text{interfacial heat transfer}} \tag{2.30}$$

In (2.28) and (2.30), $\langle \overline{T_s} \rangle^i$ and $\langle \overline{T_f} \rangle^i$ denote the intrinsic average temperature of solid and fluid phases, respectively, A_i is the interfacial area within the REV and $\mathbf{n}_i$ is the unit vector normal to the fluid-solid interface, pointing from the fluid towards the solid phase. Equations (2.28) and (2.30) are the macroscopic energy equations for the fluid and the porous matrix (solid), respectively.

In order to use Eqs. (2.28) and (2.30), the underscored terms have to be modeled in some way as a function of the intrinsically averaged temperature of solid phase and fluid, $\langle \overline{T_s} \rangle^i$ and $\langle \overline{T_f} \rangle^i$. To accomplish this, a gradient type diffusion model is used for all the terms, in the form,

$$\text{Turbulent heat flux: } - (\rho c_p)_f \left(\phi \, \overline{\langle \mathbf{u}' \rangle^i \langle T_f' \rangle^i} \right) = \mathbf{K}_t \cdot \nabla \langle \bar{T}_f \rangle^i. \tag{2.31}$$

$$\text{Thermal dispersion: } - (\rho c_p)_f \left(\phi \, \langle {}^i\bar{\mathbf{u}}^i \overline{T_f} \rangle^i \right) = \mathbf{K}_{disp} \cdot \nabla \langle \bar{T}_f \rangle^i. \tag{2.32}$$

$$\text{Turbulent thermal dispersion: } - (\rho c_p)_f \left(\phi \, \langle {}^i\overline{\mathbf{u}'^i T_f'} \rangle^i \right) = \mathbf{K}_{disp,t} \cdot \nabla \langle \bar{T}_f \rangle^i. \tag{2.33}$$

$$\text{Local conduction: } \begin{cases} \nabla \cdot \left[\dfrac{1}{\Delta V} \displaystyle\int\limits_{A_i} \mathbf{n}_i k_f \overline{T_f} \, dA \right] = \mathbf{K}_{f,s} \cdot \nabla \langle \bar{T}_s \rangle^i \\ -\nabla \cdot \left[\dfrac{1}{\Delta V} \displaystyle\int\limits_{A_i} \mathbf{n}_i k_s \overline{T_s} \, dA \right] = \mathbf{K}_{s,f} \cdot \nabla \langle \bar{T}_f \rangle^i \end{cases}. \tag{2.34}$$

where $\mathbf{n}_i$ in (2.34), as mentioned, is the unit vector pointing outwards of the fluid phase. In this work, for simplicity, one assumes that for turbulent flow the overall thermal resistance between the two phases is controlled by the interfacial film coefficient rather than by the thermal resistance within each phase. As such, the coefficients $\mathbf{K}_{f,s}, \mathbf{K}_{s,f}$ are here neglected for the sake of simplicity. More information on such quantities is given below.

The heat transferred between the two phases can be modeled by means of a film coefficient h_i such that,

$$h_i a_i\left(\langle\overline{T_s}\rangle^i - \langle\overline{T_f}\rangle^i\right) = \frac{1}{\Delta V}\int\limits_{A_i} \mathbf{n}_i \cdot k_f \nabla\overline{T_f}\, dA = \frac{1}{\Delta V}\int\limits_{A_i} \mathbf{n}_i \cdot k_s \nabla\overline{T_s}\, dA. \tag{2.35}$$

where $a_i = A_i/\Delta V$ is the surface area per unit volume. Using the above shown expressions, Eqs. (2.28) and (2.30) can be written as:

$$\left\{\left(\rho c_p\right)_f \phi\right\}\frac{\partial\langle\overline{T}\rangle^i}{\partial t} + \left(\rho c_p\right)_f \nabla\cdot\left(\mathbf{u}_D\langle\overline{T_f}\rangle^i\right) = \nabla\cdot\left\{\mathbf{K}_{eff,f}\cdot\nabla\langle\overline{T_f}\rangle^i\right\} + h_i a_i\left(\langle\overline{T_s}\rangle^i - \langle\overline{T_f}\rangle^i\right), \tag{2.36}$$

$$\left\{(1-\phi)\left(\rho c_p\right)_s\right\}\frac{\partial\langle\overline{T_s}\rangle^i}{\partial t} = \nabla\cdot\ \left\{\mathbf{K}_{eff,s}\cdot\nabla\langle\overline{T_s}\rangle^i\right\} - h_i a_i\left(\langle\overline{T_s}\rangle^i - \langle\overline{T_f}\rangle^i\right), \tag{2.37}$$

where, $\mathbf{K}_{eff,f}$ and $\mathbf{K}_{eff,s}$ are the effective conductivity tensor for fluid and solid, respectively, given by:

$$\mathbf{K}_{eff,f} = [\phi k_f]\mathbf{I} + \mathbf{K}_{f,s} + \mathbf{K}_t + \mathbf{K}_{disp} + \mathbf{K}_{disp,t}, \tag{2.38}$$

$$\mathbf{K}_{eff,s} = [(1-\phi)k_s]\mathbf{I} + \mathbf{K}_{s,f}, \tag{2.39}$$

and $\mathbf{I}$ is the unit tensor.

In order to be able to apply Eq. (2.36), it is necessary to determine the dispersion and conductivity tensors in Eq. (2.38), i.e., $\mathbf{K}_{f,s}$, $\mathbf{K}_t$, $\mathbf{K}_{disp}$ and $\mathbf{K}_{disp,t}$. Following Kuwahara et al. [13] and Quintard et al. [3], $\mathbf{K}_{f,s}$ and $\mathbf{K}_{disp}$, are obtained by making use of a unit cell subjected to periodic boundary conditions, where (2.32) are (2.34) are numerically resolved. Further, dispersion tensor components are then obtained directly from the microscopic results, for a unit cell, and reads for $Pe_D \geq 10$ [13]:

$$\frac{\left(K_{disp}\right)_{yy}}{k_f} = 0.052(1-\phi)^{0.5} Pe_D, \text{for transverse dispersion,} \tag{2.40}$$

$$\frac{\left(K_{disp}\right)_{xx}}{k_f} = 2.1\frac{Pe_D}{(1-\phi)^{0.1}}, \text{for longitudinal dispersion,} \tag{2.41}$$

Also, starting out from the time averaged energy equation, coupled with the microscopic modeling for the turbulent heat flux through the microscopic Eddy diffusivity, one can write:

$$-\left(\rho c_p\right)_f\overline{\mathbf{u}'T_f'} = \left(\rho c_p\right)_f\frac{\nu_t}{\sigma_T}\nabla\bar{T}_f \tag{2.42}$$

where σ_T is the turbulent Prandtl number which is taken here as a constant. Applying the volume average to the resulting Eq. (2.42) one obtains the macroscopic turbulent heat flux modeled as,

$$-(\rho c_p)_f \langle \overline{\mathbf{u}' T_f'} \rangle^i = (\rho c_p)_f \frac{\nu_{t_\phi}}{\sigma_T} \nabla \langle \bar{T}_f \rangle^i \tag{2.43}$$

where we have adopted the symbol ν_{t_φ} to express the macroscopic version of the Eddy viscosity, $\mu_{t_\phi} = \rho_f \nu_{t_\phi}$.

Equation (2.43) represents the sum of the turbulent heat flux and the turbulent thermal dispersion terms. As such, the turbulent heat flux and turbulent thermal dispersion components of the conductivity tensor in Eq. (2.38), $\mathbf{K}_t$ and $\mathbf{K}_{disp,t}$, which can not be determined from such a microscopic calculation, are here modeled through the Eddy diffusivity concept, as:

$$\mathbf{K}_t + \mathbf{K}_{disp,t} = \phi (\rho c_p)_f \frac{\nu_{t_\phi}}{\sigma_T} \mathbf{I} \tag{2.44}$$

where $\sigma_T = 0.9$ is the macroscopic turbulent Prandtl number for the fluid energy equation.

2.2.5 *Correlations for Interfacial Heat Transfer,* $\mathbf{h_i}$

Wakao et al. [14] proposed a correlation for h_i for closely packed bed and compared results with their experimental data. This correlation reads,

$$\frac{h_i D}{k_f} = 2 + 1.1 Re_D^{0.6} Pr^{1/3}. \tag{2.45}$$

Kuwahara et al. [15] also obtained the interfacial convective heat transfer coefficient for laminar flow, as follows,

$$\frac{h_i D}{k_f} = \left(1 + \frac{4(1-\phi)}{\phi}\right) + \frac{1}{2}(1-\phi)^{1/2}\, \mathrm{Re}_D\, \mathrm{Pr}^{1/3}, \text{valid for } 0.2 < \phi < 0.9, \tag{2.46}$$

Equation (2.46) is based on porosity dependency and is valid for packed beds of particle diameter D.

As will be seen below, in this work an additional correlation will be presented, which will be valid for both laminar and turbulent flows.

2.3 Periodic Cell

Nakayama et al. [16] and Kuwahara et al. [15] modeled a porous medium in terms of obstacles arranged in a regular pattern and solved the set of the local governing equations exploiting periodic boundary conditions. As such, consider a macroscopically uniform flow through an infinite number of square rods of lateral size D, placed in a staggered arrangement and maintained at constant temperature T_w. The periodic cell or representative elementary volume, ΔV, is schematically showed in Fig. 2.1a and has dimensions $2H \times H$. Computations within this cell were carried out using a non-uniform grid, as shown in Fig. 2.1b, to ensure that the results were grid independent. The Reynolds number $Re_D = \rho \bar{\mathbf{u}}_D D/\mu$ was varied from 10^4 to 10^7 and the porosity was determined as $\phi = 1 - (D/H)^2$.

2.3.1 Numerical Method and Boundary Conditions

The numerical method utilized to discretize the flow and energy equations in the unit cell is the Finite Control Volume approach. The SIMPLE method of Patankar [17] was used for solving Eqs. (2.1)–(2.4) and for handling the velocity- pressure coupling. Convergence was monitored in terms of the normalized residue for each variable. The maximum residue allowed for convergence check was set to 10^{-9}, being the variables normalized by appropriate reference values.

For periodic fully developed flow in the cell of Fig. 2.1b, the velocity at exit ($x/H = 2$) must be identical to that at the inlet ($x/H = 0$). Temperature profiles, however, are only identical at both cell exit and inlet if presented in terms of an appropriate non-dimensional variable. The situation is analogous to the case of forced convection in a channel with isothermal walls. Due to the periodicity of the model a single structural unit, as depicted in Fig. 2.1b, may be taken as a calculation domain. The equations used for turbulent flow in the unit cell are Eqs. (2.5)–(2.14).

Thus, boundary conditions and periodic constraints are given by:

On the solid walls (Low Re):

$$\bar{u} = 0, k = 0, \quad \varepsilon = \nu \frac{\partial^2 k}{\partial y^2}, \quad \bar{T} = \bar{T}_w, \tag{2.47}$$

On the solid walls (high Re):

$$\frac{\bar{u}}{u_\tau} = \frac{1}{\kappa} \ln(y^+ \mathrm{E}), \quad k = \frac{u_\tau^2}{c_\mu^{1/2}}, \quad \varepsilon = \frac{c_\mu^{3/4} k_w^{3/2}}{\kappa\, y_w}, \quad q_w = \frac{\left(\rho c_p\right)_f c_\mu^{1/4} k_w^{1/2} (\bar{T} - T_w)}{\left(\frac{Pr_t}{\kappa} \ln\left(y_w^+\right) + c_Q(Pr)\right)} \tag{2.48}$$

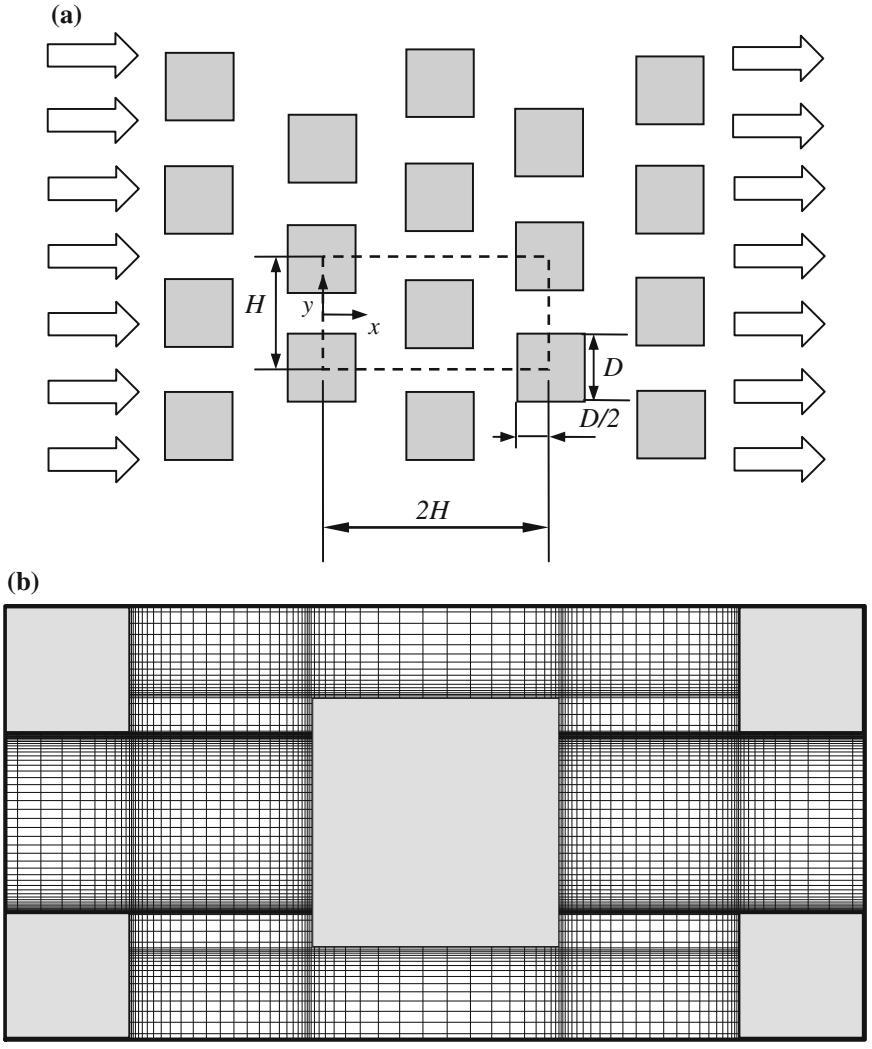

Fig. 2.1 Infinite medium: **a** Physical model and coordinate system, **b** Non uniform computational grid

where, $u_\tau = \left(\frac{\tau_w}{\rho}\right)^{1/2}$, $y_w^+ = \frac{y_w u_\tau}{\nu}$, $c_Q = 12.5Pr^{2/3} + 2.12\ln(Pr) - 5.3$ for $Pr > 0.5$ where, Pr and Pr_t are Prandtl and turbulent Prandtl number, respectively, q_w is wall heat flux, u_τ is wall-friction velocity, y_w is the coordinate normal to wall, κ is constant for turbulent flow past smooth impermeable walls or von Kármán's constant and E is an integration constant that depends on the roughness of the wall. For smooth walls with constant shear stress E = 9.

On the symmetry planes:

$$\frac{\partial \bar{u}}{\partial y} = \frac{\partial \bar{v}}{\partial y} = \frac{\partial k}{\partial y} = \frac{\partial \varepsilon}{\partial y} = 0, \tag{2.49}$$

where $\bar{u}$ and $\bar{v}$ are components of $\bar{\mathbf{u}}$.

On the periodic boundaries:

$$\bar{u}|_{inlet} = \bar{u}|_{outlet}, \quad \bar{v}|_{inlet} = \bar{v}|_{outlet}, \quad k|_{inlet} = k|_{outlet}, \quad \varepsilon|_{inlet} = \varepsilon|_{outlet}, \tag{2.50}$$

$$\theta|_{inlet} = \theta|_{outlet} \Leftrightarrow \left.\frac{\bar{T} - \bar{T}_w}{\bar{T}_B(x) - \bar{T}_w}\right|_{inlet} = \left.\frac{\bar{T} - \bar{T}_w}{\bar{T}_B(x) - \bar{T}_w}\right|_{outlet}, \tag{2.51}$$

The bulk mean temperature of the fluid is given by:

$$\bar{T}_B(x) = \frac{\int \bar{u}\bar{T}dy}{\int \bar{u}dy} \tag{2.52}$$

Computations are based on the Darcy velocity, the length of structural unit H and the temperature difference $(\bar{T}_B(x) - \bar{T}_w)$, as references scales.

2.3.2 *Film Coefficient* $\mathbf{H_i}$

Determination of h_i is here obtained by calculating, for the unit cell of Fig. 2.1b, an expression given as,

$$h_i = \frac{Q_{total}}{A_i \Delta T_{ml}} \tag{2.53}$$

where $A_i = 8D\,x\,1$. The overall heat transferred in the cell, Q_{total}, is giving by,

$$Q_{total} = (H - D)\rho \bar{u}_B c_p \left(\bar{T}_B|_{outlet} - \bar{T}_B|_{inlet}\right), \tag{2.54}$$

The bulk mean velocity of the fluid is given by:

$$\bar{u}_B(x) = \frac{\int \bar{u}dy}{\int dy} \tag{2.55}$$

and the logarithm mean temperature difference, ΔT_{ml} is,

$$\Delta T_{ml} = \frac{\left(\bar{T}_w - \bar{T}_B|_{outlet}\right) - \left(\bar{T}_w - \bar{T}_B|_{inlet}\right)}{\ln[(\bar{T}_w - \bar{T}_B|_{outlet})(\bar{T}_w - \bar{T}_B|_{inlet})]} \tag{2.56}$$

Equation (2.54) represents an overall heat balance on the entire cell and associates the heat transferred to the fluid to a suitable temperature difference ΔT_{ml}. As mentioned earlier, Eqs. (2.1)–(2.4) were numerically solved in the unit cell until conditions Eqs. (2.50) and (2.51) were satisfied.

2.3.3 A Correlation for Interstitial Heat Transfer

Figure 2.2a show distributions of pressure, isotherms and turbulence kinetic energy in a microscopic porous structure, obtained at $Re_D = 10^5$ for cases of $\phi = 0.65$. Pressure increases at the front face of the square rod and drastically decreases around the corner, as can be seen from the pressure contours shown in Fig. 2.2a.

Temperature distribution is shown in Fig. 2.2b. Colder fluid impinges on the rod left side yielding strong temperature gradients on that face. Downstream the obstacles, fluid recirculation smooths temperature gradients and deforms isotherms within the mixing region. When the Reynolds number is sufficiently high (not shown here), thermal boundary layers cover the rod surfaces indicating that convective heat transfer overwhelms thermal diffusion. Figure 2.2c presents levels of turbulence kinetic energy, which are higher around the rod corners where a strong shear layer is formed. Further downstream the rods in the weak region, steep velocity gradients appear due to flow deceleration, increasing there also the local level of k.

Once fully developed flow and temperature fields are achieved, for the fully developed condition ($x > 6H$), bulk temperatures were calculated according to Eq. (2.52), at both inlet and outlet positions. They were then used to calculate h_i using Eqs. (2.53)–(2.56). Results for h_i are plotted in Fig. 2.3a for Re_D up to 10^7. Also plotted in this figure are results computed with correlation (2.46) by Kuwahara et al. [15] using $\phi = 0.65$. The figure seems to indicate that both computations show a reasonable agreement for laminar results. In addition, numerical results for turbulent flow using Low and High Re models are also presented in this figure.

Figure 2.3b shows numerical results for the interfacial convective heat transfer coefficient for various porosities ($\phi = 0.44$, $\phi = 0.65$ and $\phi = 0.90$). Results for h_i are plotted for Re_D up to 10^7. In order to obtain a correlation for h_i in the turbulent regime, all curves were first collapsed after plotting them in terms of Re_D/ϕ, as showed in Fig. 2.4a. Furthermore, the least square technique was applied in order to determine the best correlation, which lead to a minimum overall error. Thus, the following expression is here proposed:

$$\frac{h_i D}{k_f} = 0.08\left(\frac{Re_D}{\phi}\right)^{0.8} Pr^{1/3}; \quad \text{for} \quad 1.0\times 10^4 < \frac{Re_D}{\phi} < 2.0\times 10^7, \quad \text{valid for} \quad 0.2 < \phi < 0.9, \tag{2.57}$$

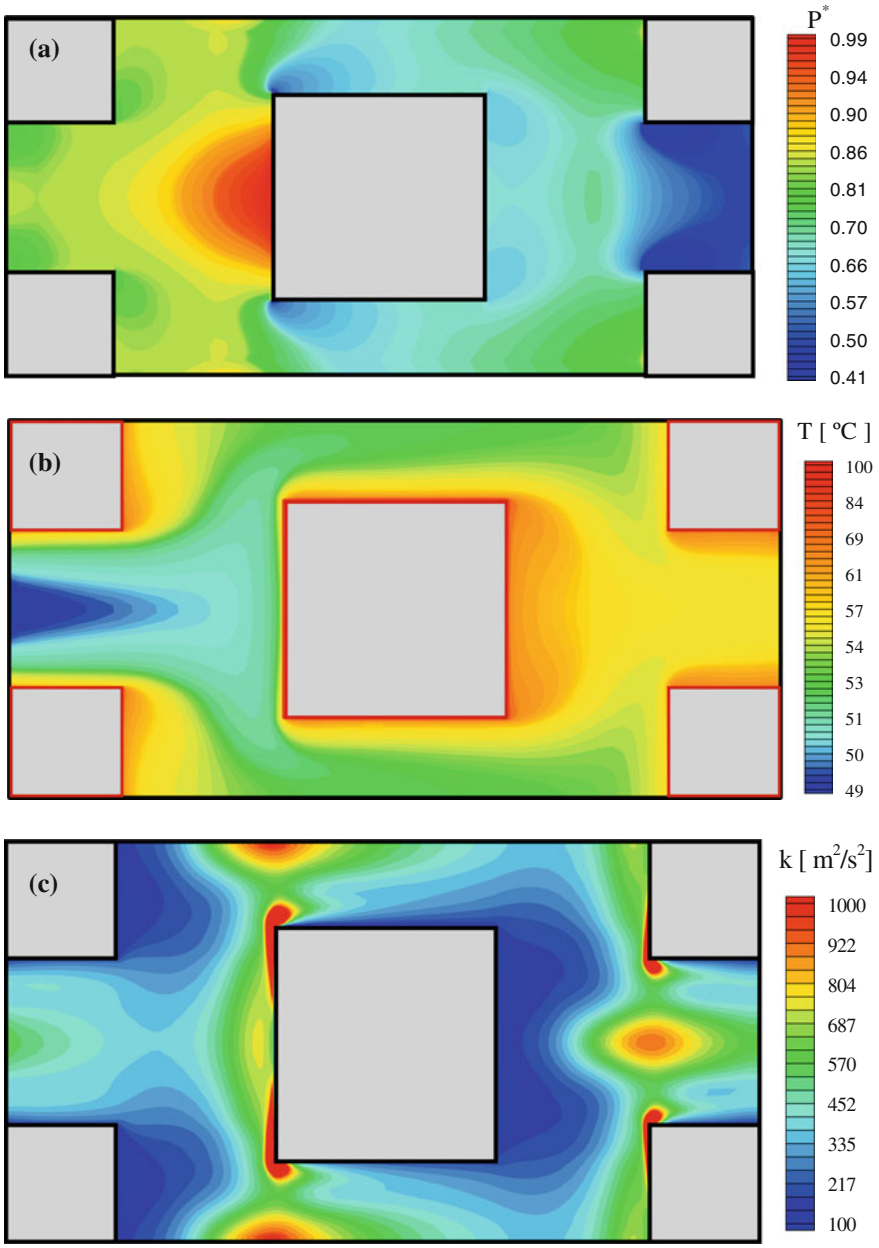

Fig. 2.2 Results for periodic cell: **a** Nondimensional pressure field for $Re_D = 10^5$ and $\phi = 0.65$, **b** Isotherms for $Pr = 1$, $Re_D = 10^5$ and $\phi = 0.65$, **c** Turbulence kinetic energy for $Re_D = 10^5$ and $\phi = 0.65$

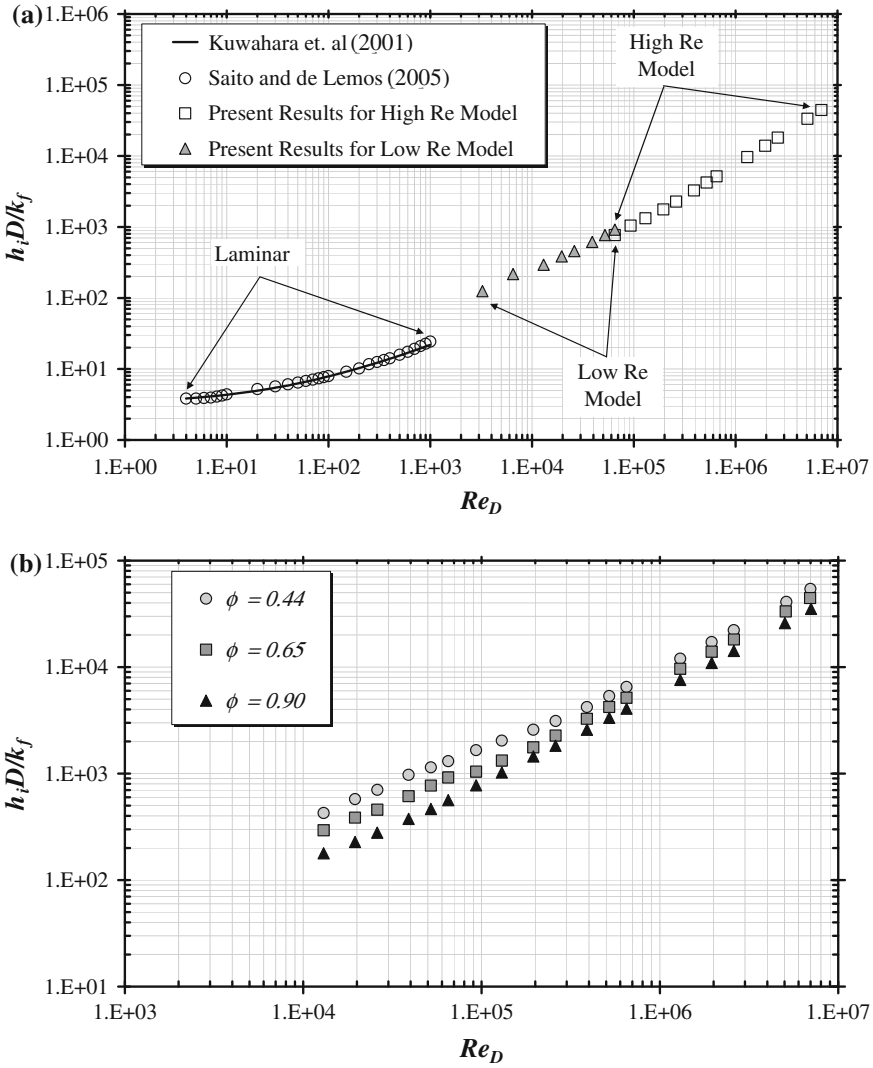

Fig. 2.3 Results for unit cell: **a** Effect of Re_D on h_i for $Pr = 1$ and $\phi = 0.65$, **b** Effect of porosity on h_i for $Pr = 1$

Equation (2.57), which gives the heat transfer coefficient for turbulent flow, is compared with numerical results obtained with Low and High Re models. Such comparison is presented in Fig. 2.4b, which also shows computations using correlations given by Eqs. (2.45) and (2.46) by Wakao et al. [14] and Zhukauskas [18], respectively. The agreement between the present correlation, other correlations in the literature and the numerical simulations stimulates further investigation on this

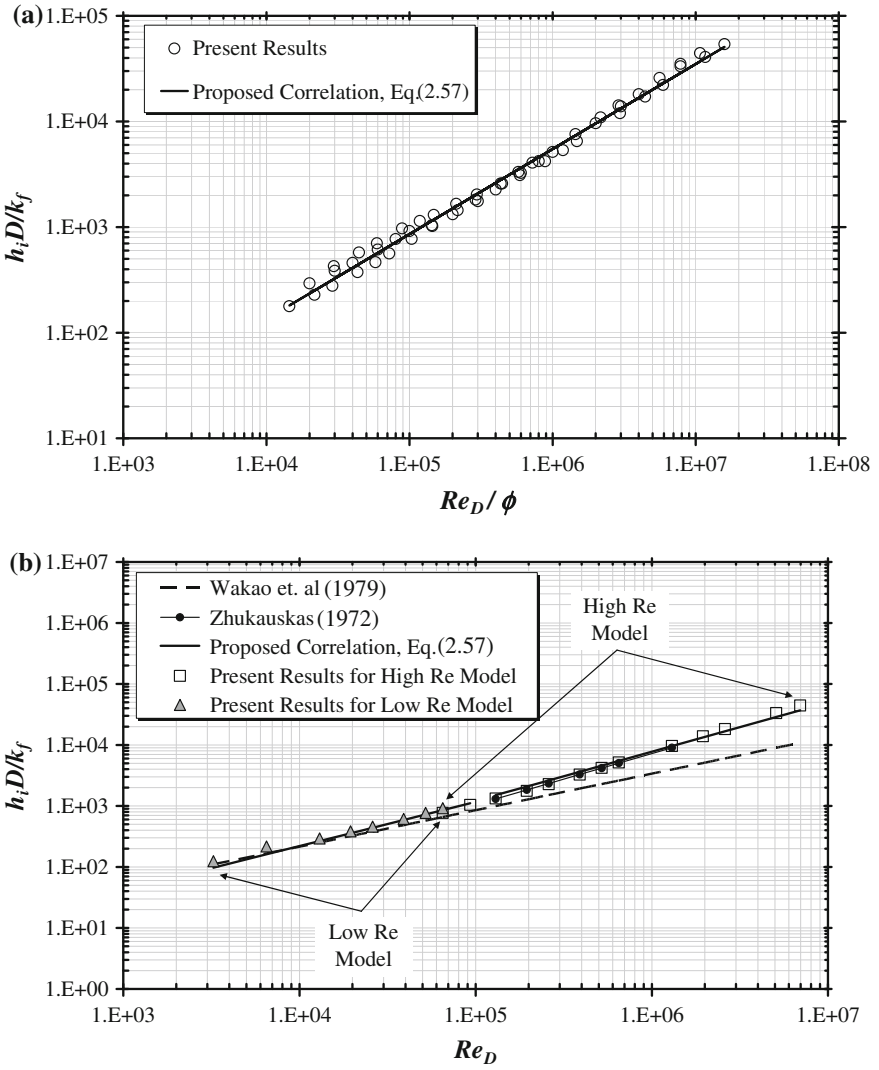

Fig. 2.4 Comparison of the numerical results for unit cell: **a** With proposed correlation Eq. (2.57), **b** With various correlations for $\phi = 0.65$

subject, contributing towards the building of a more general expression for the interfacial heat transfer coefficient for porous media. Table 2.1 compares Eq. (2.57) with other correlations in the literature.

Table 2.1 Correlations for heat transfer coefficient and fluid-to-solid specific area a_i

References	Correlation	Equations	a_i	Flow regime
Wakao et al. [14]	$\frac{h_i D}{k_f} = 2 + 1.1 Re_D^{0.6} Pr^{1/3}$	(2.45)	$\frac{6(1-\phi)}{D}$	Laminar
Kuwahara et al. [15]	$\frac{h_i D}{k_f} = \left(1 + \frac{4(1-\phi)}{\phi}\right) + \frac{1}{2}(1-\phi)^{1/2} Re_D Pr^{1/3}$	(2.46)	$\frac{4(1-\phi)}{D}$	Laminar
Proposed correlation	$\frac{h_i D}{k_f} = 0.08\left(\frac{Re_D}{\phi}\right)^{0.8} Pr^{1/3}$	(2.57)	$\frac{4(1-\phi)}{D}$	Turbulent

2.4 Laminar Flow in a Channel

This section presents numerical results with the macroscopic model above. The problem considered here is flow through a two-dimensional channel completely filled with a fixed porous substrate, as shown in Fig. 1.3a. Boundary conditions and periodic constraints for turbulent flows in porous media are similar to those applied to clear channel flow.

2.4.1 Non-dimensional Parameters

The longitudinal Nusselt number is calculated for both the fluid and solid phases and is defined as [19],

$$\text{Fluid phase Nusselt number: } Nu_f = -\frac{2H}{T_w - T_{mf}}\left(\frac{\partial \langle T_f \rangle^i}{\partial y}\right), \tag{2.58}$$

$$\text{Solid phase Nusselt number: } Nu_s = -\frac{2H}{T_w - T_{ms}}\left(\frac{\partial \langle T_s \rangle^i}{\partial y}\right), \tag{2.59}$$

where T_{mf} and T_{ms} are the average temperature of the fluid and the solid phase, respectively, and are defined as follows;

$$T_{mf} = \frac{\int u T_f dy}{u_B H}, u_B = \frac{\int u dy}{H}, T_{ms} = \frac{\int T_s dy}{H}, \tag{2.60}$$

The solid phase Nusselt number, Nu_s, was proposed by [19] and refers to a non-dimensional temperature gradient for the solid phase at the wall. This concept has also been applied in reference [20] for laminar flows.

Non-dimensional local and cross-section averaged temperatures, for both phases, are defined as,

$$\theta_{(s,f)} = \frac{T_w - T_{(s,f)}}{T_w - T_{inlet_{(s,f)}}} \tag{2.61}$$

$$\Theta_{(s,f)} = \frac{T_{m_{(s,f)}} - T_{inlet_f}}{T_{inlet_s} - T_{inlet_f}}, \tag{2.62}$$

2.4.2 Numerical Method and Boundary Conditions

As before, the numerical method used to discretize the flow and energy equations was the Control Volume approach and the SIMPLE method of Patankar [17] was applied to relax the systems of algebraic equations. For convergence, the normalized residue was set to be lower than 10^{-9}. Boundary conditions are given by:

$$\text{On the solid walls: } \langle \mathbf{u} \rangle^i = 0, \langle T_s \rangle^i = \langle T_f \rangle^i = T_w, \tag{2.63}$$

$$\text{On the entrance: } \mathbf{u}_D = \mathbf{u}_{inlet}, \langle T_s \rangle^i = \langle T_f \rangle^i = T_{inlet}, \tag{2.64}$$

2.4.3 Local Nusselt Numbers

The effect of the Reynolds number is shown in Fig. 2.5 compared with similar computations by Alazmi and Vafai [19]. The Reynolds number is found to have a substantial effect on the development length for *Nu* along the channel. Figure 2.5c seems to indicate that for lower Reynolds number, the thermal equilibrium condition is achieved faster than for higher Reynolds number cases. Both solid and fluid temperatures reach an equilibrium value along *X*, decreasing the *Nu* difference along the channel.

Figure 2.6 shows the effect of porosity on Nusselt for both phases. It is observed from Fig. 2.6a, b that the lower the porosity, the smaller the differences between the present results and those by Alazmi and Vafai [19]. For thermally developed flow and low porosity, both sets of results are closer to each other. Also, the higher the porosity, the higher the *Nu* number. High porosity condition means a lower interfacial area a_i, reducing the exchange of energy between phases, leading ultimately to higher values of *Nu*. Figure 2.6c presents similar results in each phase for the entrance region of parallel plates.

The particle diameter, *D*, is directly related to the interfacial area a_i and appears in the expressions for h_i. Low values for *D* are associated with high interfacial areas and high interfacial film coefficients. As such, for the same porosity smaller particle

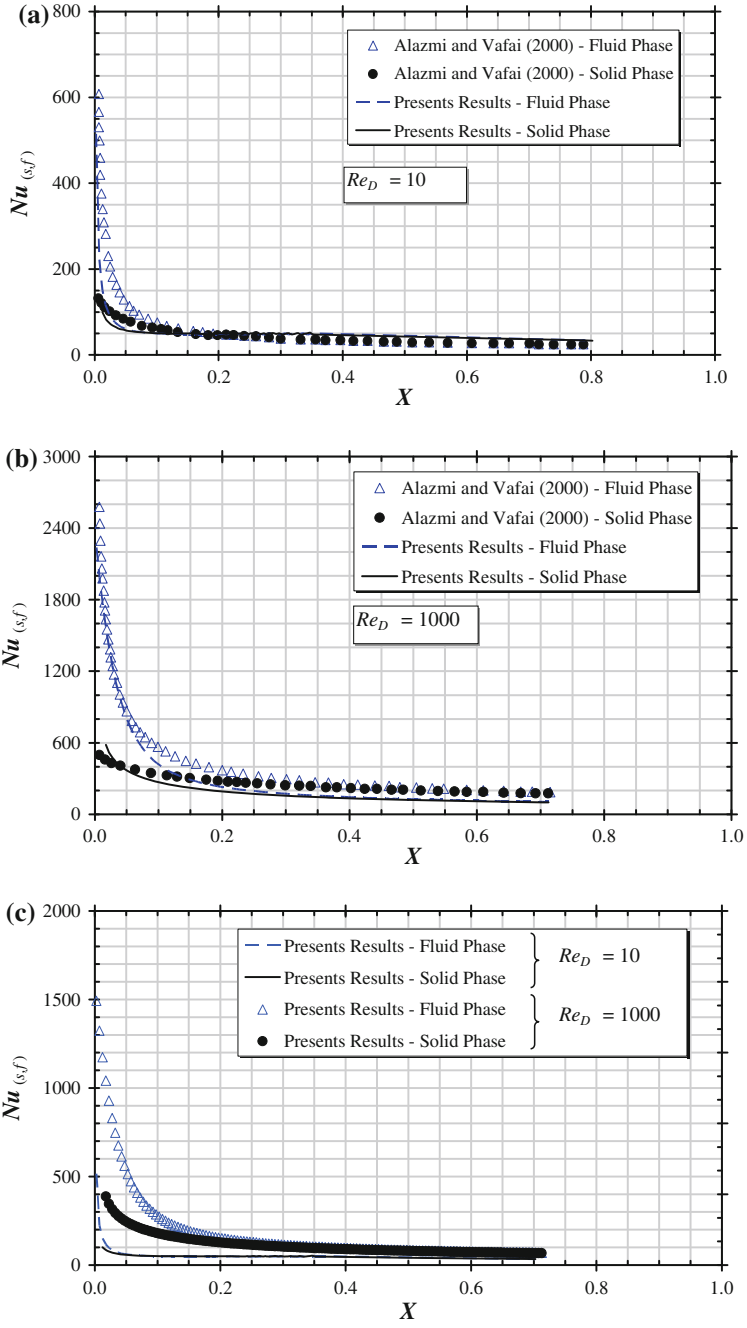

Fig. 2.5 Effect of Re on longitudinal Nusselt number. $Da = 10^{-4}; \phi = 0.6; D/H = 5.2 \times 10^{-2}$; $k_s/k_f = 25$; **a** $Re_D = 10$, **b** $Re_D = 1000$, **c** Both Re, present results

diameters promote thermal equilibrium between phases by increasing the area of contact between the solid and the fluid. On the other hand, larger particle diameters tend to impair thermal equilibrium between phases, as seen in Fig. 2.7a, b. Figure 2.7c shows the difference between each phase for distinct values of D and shows that thermal equilibrium is reached faster for smaller particle diameters. Also shown is that the larger particle diameters impair thermal equilibrium, affecting temperature distributions and leading to lower Nu numbers for both phases.

Figure 2.8 shows the effect of thermal conductivity ratio on Nu. As seen in Fig. 2.8a, b, a lower conductivity ratio enhances thermal equilibrium by reducing temperature differences between phases. Figure 2.8c presents a comparison of Nusselt numbers indicating that for a high conductivity ratio, impairment on the exchange of energy between phases affects local temperature values, ultimately reducing corresponding Nusselt numbers.

Finally, Fig. 2.9 shows a comparison of present results and those by Wakao et al. [14] and Kuwahara et al. [15] correlations in addition to results by Alazmi and Vafai [19]. It is clearly seen from Fig. 2.9 that a reasonable agreement is found between the predictions, except for the Kuwahara correlation [15] for the fluid phase Nusselt number, which is slightly higher. This discrepancy could be explained due to the fact that predictions by Alazmi and Vafai [19] were obtained with Wakao correlation [14], which is calculated considering a_i based on circular rods instead of square rods.

2.5 Turbulent Flow in a Channel

Results below were obtained after extensive testing on grid size independence and search for optimal relaxation parameters. Due to lack of space here, the interest reader is referred to previous work where such studies are presented in detail [20–22].

Also, for turbulent flow ($Re_D = 5 \times 10^4$), a sensitive analysis on the value of h_i is performed in order to evaluate the correctness of code programming. Figure 2.10 shows results for the cross-section averaged temperatures for both the solid and fluid phases. As in the case of laminar flow, a nominal value for h_i in employed in Fig. 2.10b and compared with artificially increased (Fig. 2.10a) and reduced (Fig. 2.10c) values of the interfacial film coefficient. Also for turbulent flow, shorter (Fig. 2.10a) and larger (Fig. 2.10c) developing lengths correspond to higher and lower values for h_i, respectively, indicating that physically realistic results for temperatures are obtained.

Next, the effect of introducing $\mathbf{K}_{disp}$ in the calculations for turbulent flow is presented is Figure Fig. 2.11, for the conditions $Da = 10^{-4}$, $Re_D = 5 \times 10^4$, $D/H = 1.03 \times 10^{-1}$, $k_s/k_f = 25$ and $\phi = 0.6$. The differences between the solid and fluid phase temperature profiles are greater when thermal dispersion is

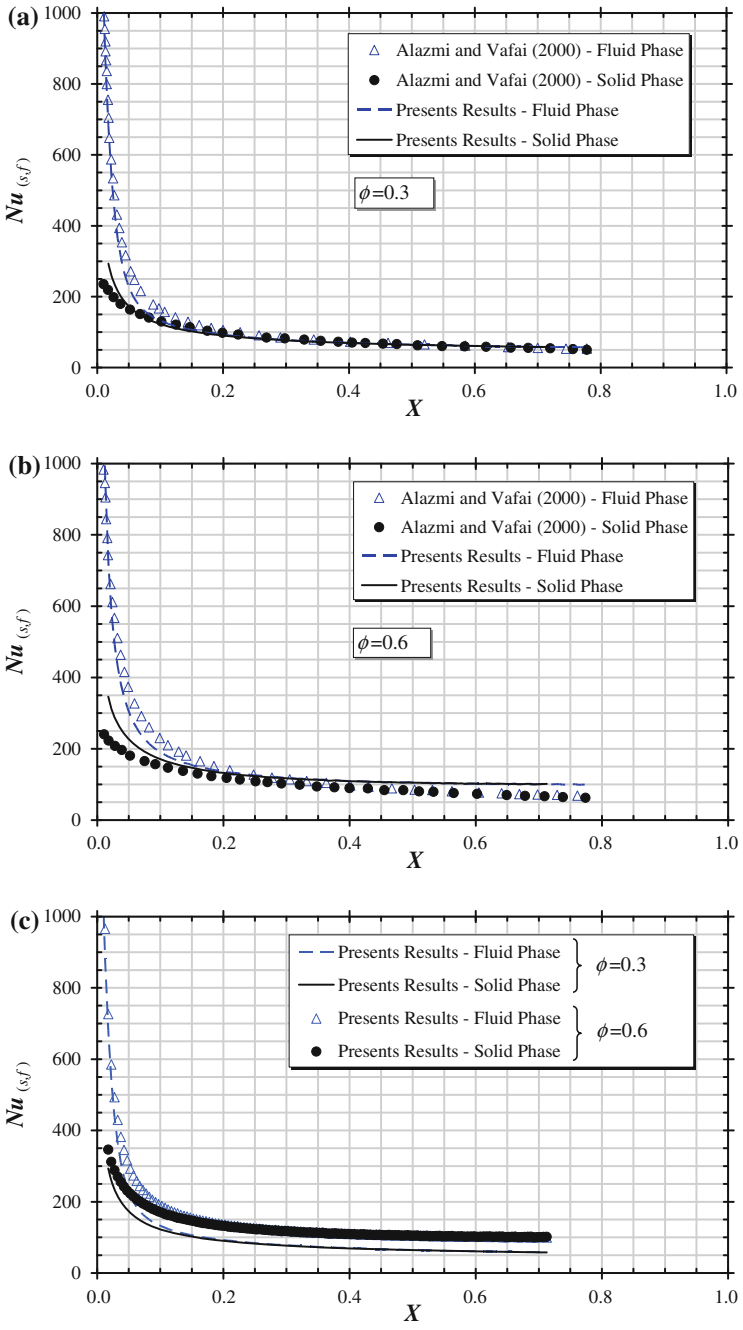

Fig. 2.6 Effect of porosity on longitudinal Nusselt number, $Re_D = 100$, $D/H = 5.2 \times 10^{-2}$, $k_s/k_f = 25$: **a** $\phi = 0.3$, **b** $\phi = 0.6$, **c** Both porosities, present results

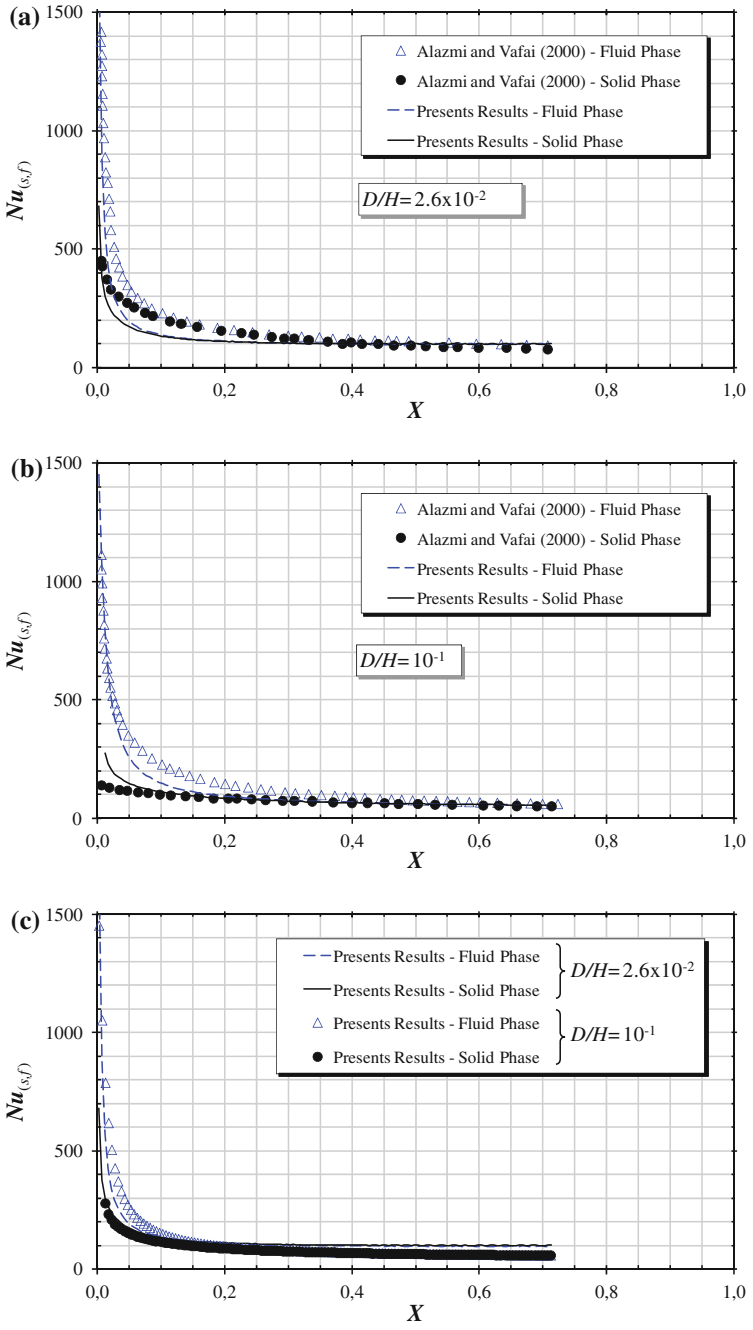

Fig. 2.7 Effect of D on longitudinal Nusselt number. $Da = 10^{-4}$; $Re_D = 100$; $\phi = 0.6$; $k_s/k_f = 25$; **a** $D/H = 2.6 \times 10^{-2}$, **b** $D/H = 10^{-1}$, **c** Both *D/H* ratios, present results

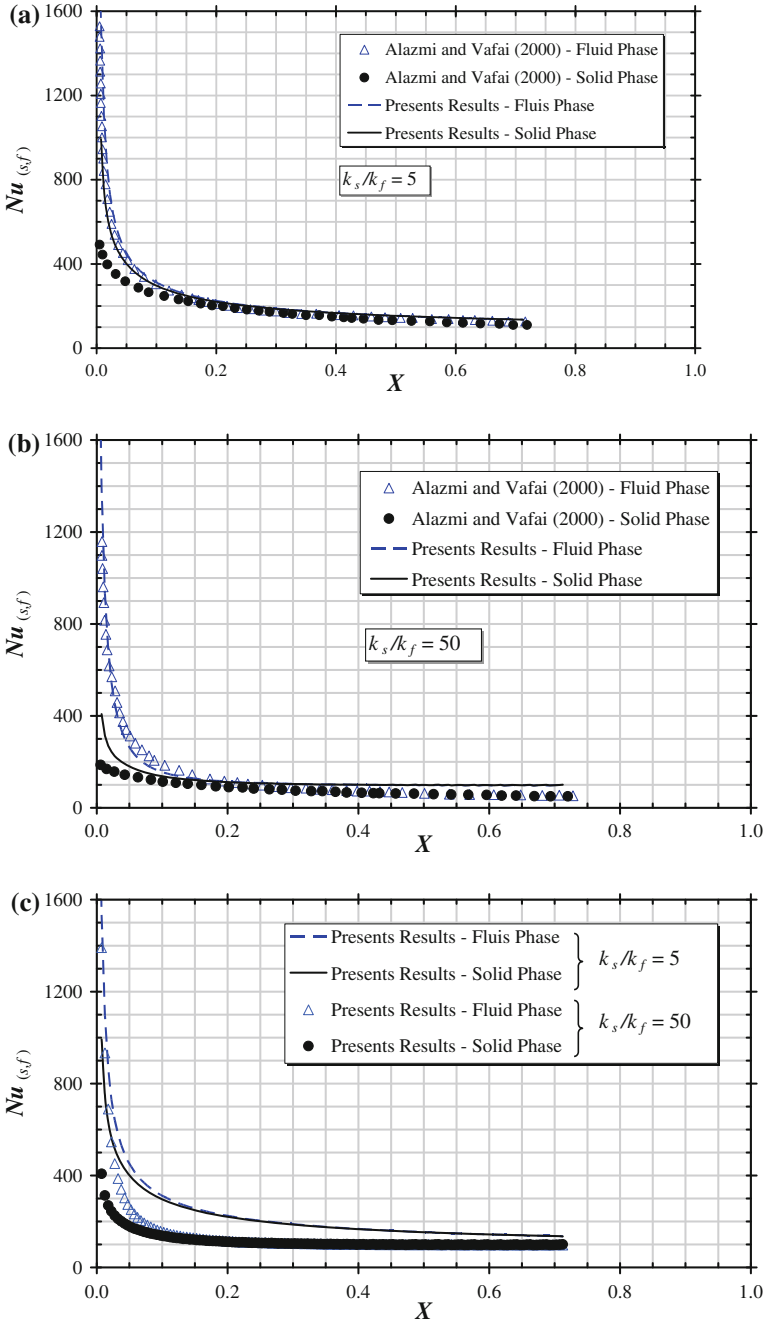

Fig. 2.8 Effect of solid-to-fluid thermal conductivity ratio on longitudinal Nusselt number. $Da = 10^{-4}; Re_D = 100; \phi = 0.6; D/H = 5.2 \times 10^{-2}$; **a** $k_s/k_f = 5$, **b** $k_s/k_f = 50$, **c** Both k_s/k_f ratios, present results

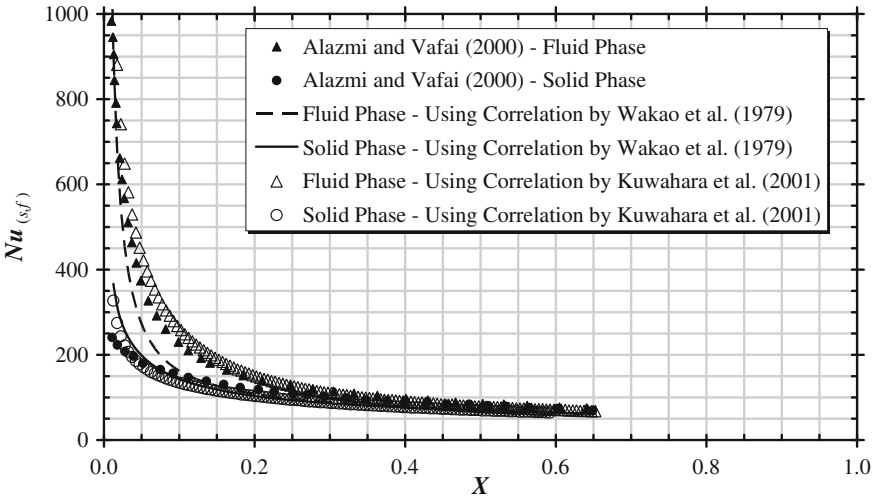

Fig. 2.9 Comparison between present results with various correlations and Alazmi and Vafai (2000) results. $Da = 10^{-4}; Re_D = 100; \phi = 0.6; D/H = 5.2 \times 10^{-2}; k_s/k_f = 25$

incorporated in the macroscopic model, particularly in the near wall region ($Y < 0.1$), which embraces the boundary layer that is much thinner than for laminar flows cases. Therefore, here also the role of the additional mechanism of dispersion is to promote diffusion across the cross section of the channel, leading to flatter $\langle \bar{T}_f \rangle^i$ profiles and larger temperature differences from corresponding local values of $\langle \bar{T}_s \rangle^i$. Effects of Reynolds number, Re_D, porosity, ϕ, non-dimensional particle diameter, D/L, and solid-to-fluid thermal conductivity, k_s/k_f, on temperature behavior are shown next.

Figure 2.12 shows the effect of the Reynolds number and boundary condition on Nu. One can note in the figure that an increase in Re_D results in an increase in Nusselt, for all cases, as expected. For high values of Re_D, Nu_f and Nu_s are closer to each other when compared with similar computations for $Re_D = 10^5$ (Fig. 2.12b). Figure 2.12c shows a comparison of all cases and indicates that Nu_f attains higher values than Nu_s, along the flow direction.

In Fig. 2.13a, b the effect of porosity ϕ on Nu is presented. An increase in porosity causes the solid phase Nusselt number to decrease whereas Nu_f in augmented, for both boundary condition types. Increase in this difference for low porosity medium could be explained by noting that a higher ϕ gives a lower h_i, according to Eq. (2.57), as well as a lower a_i, as seen in Table 2.1. Their product, $h_i a_i$, is proportional to the heat transfer between phases, as shown by the two energy Eqs. (2.36) and (2.37). Consequently, a high porosity medium will have the intensity of energy transfer between phases reduced, reflecting in the temperature fields and, ultimately, on the calculated Nu values.

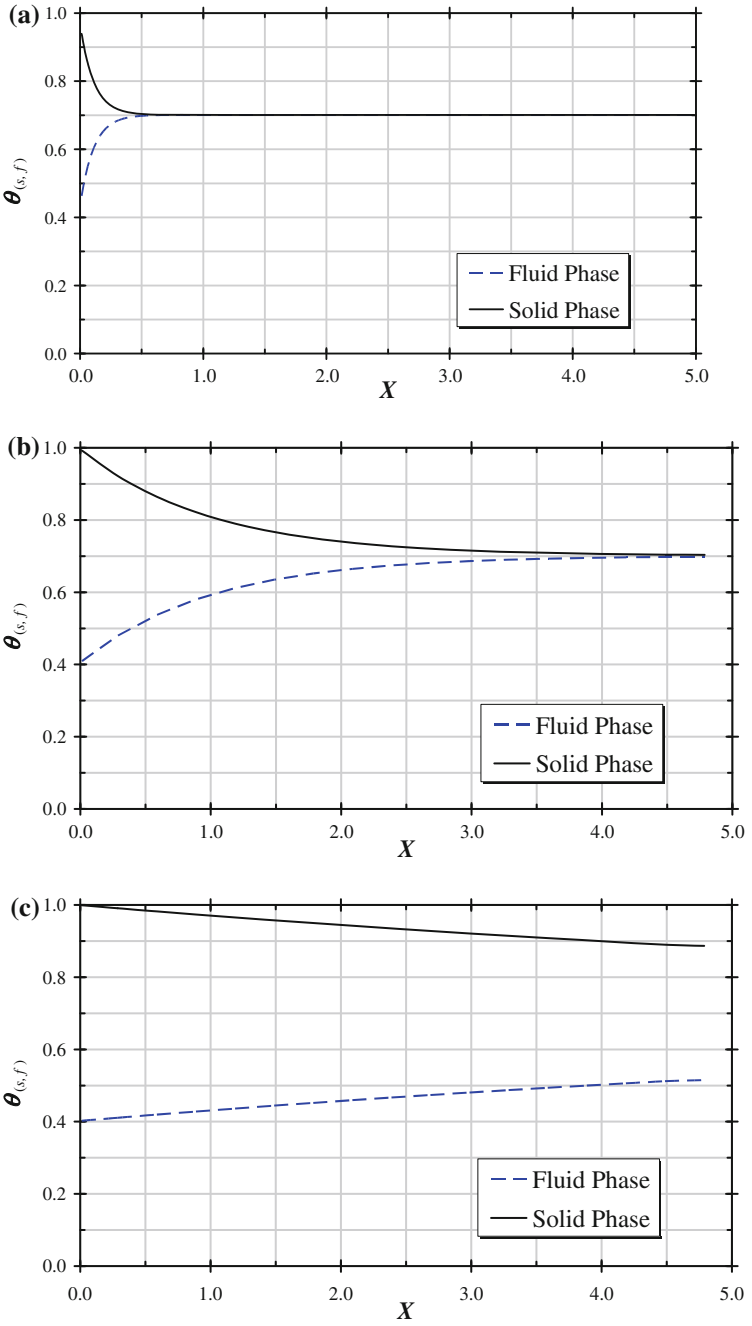

Fig. 2.10 Fluid and solid cross-sectional averaged temperatures along the flow, $Da = 10^{-4}; Re_D = 5 \times 10^4, \phi = 0.6; D/H = 1.03 \times 10^{-1}; k_s/k_f = 25$: **a** $h_{eff} = 10h_i$, **b** $h_{eff} = h_i$, **c** $h_{eff} = 0.1h_i$

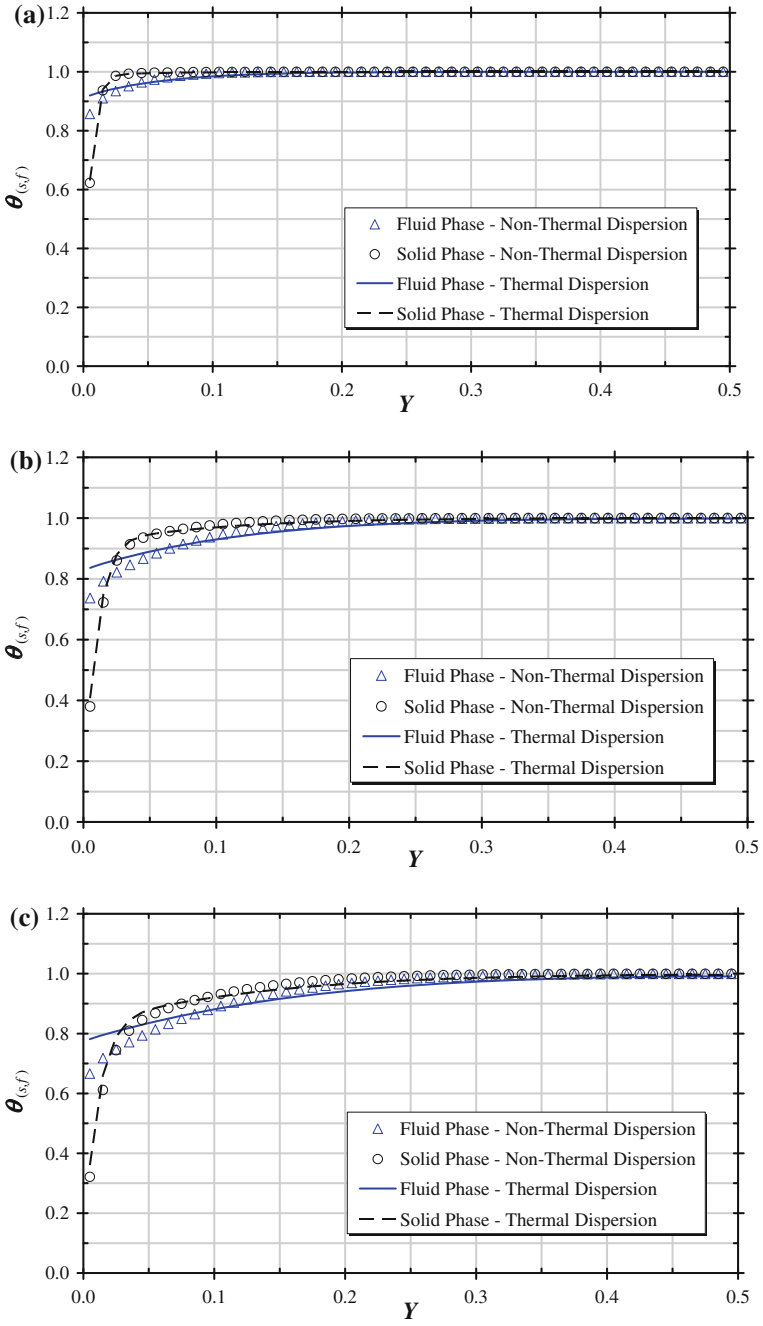

Fig. 2.11 Effect of thermal dispersion on local non-dimensional temperatures, $Da = 10^{-4}, Re_D = 5 \times 10^4, \phi = 0.6; D/H = 1.03 \times 10^{-1}, k_s/k_f = 25$: **a** $X = 0.1$, **b** $X = 0.5$, **c** $X = 1$

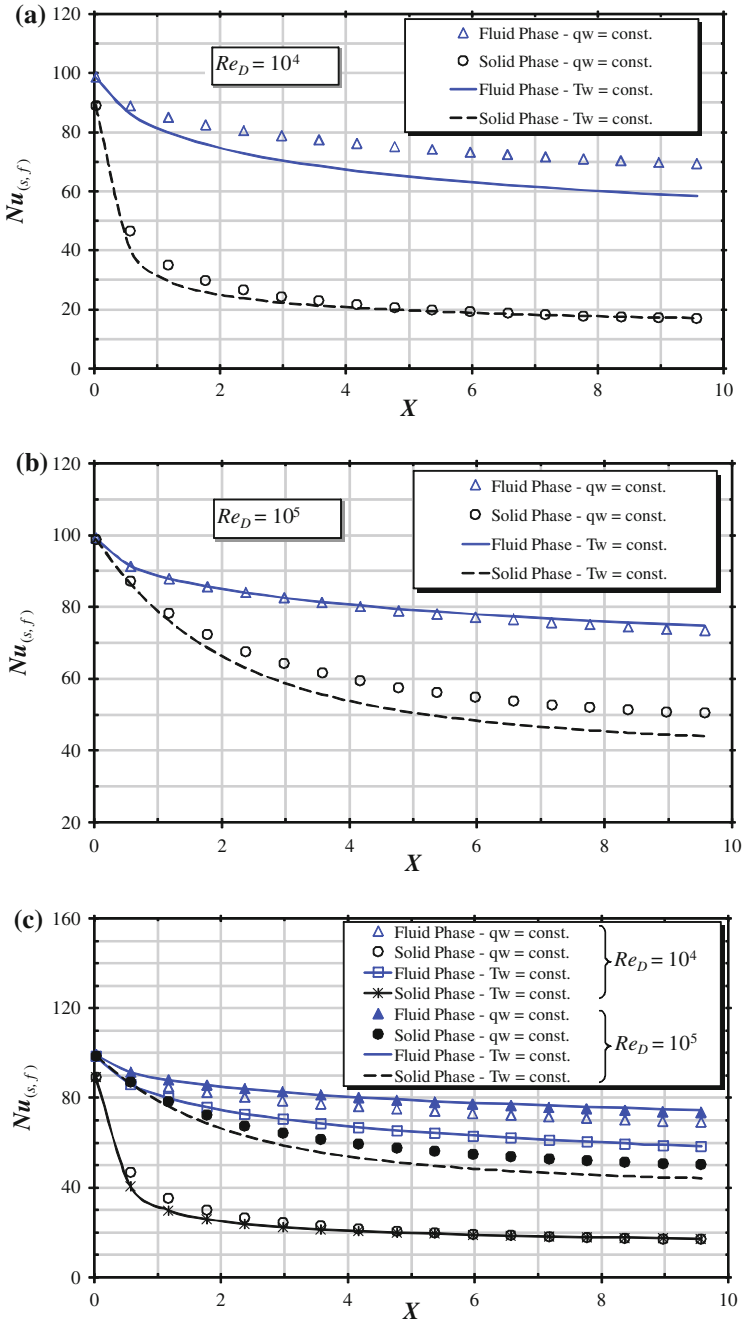

Fig. 2.12 Effect of Re_D on Nu for turbulent flow, $Da = 10^{-4}, \phi = 0.6, D/H = 1.03 \times 10^{-1}$, $k_s/k_f = 25$: **a** $Re_D = 10^4$, **b** $Re_D = 10^5$, **c** Both Re_D

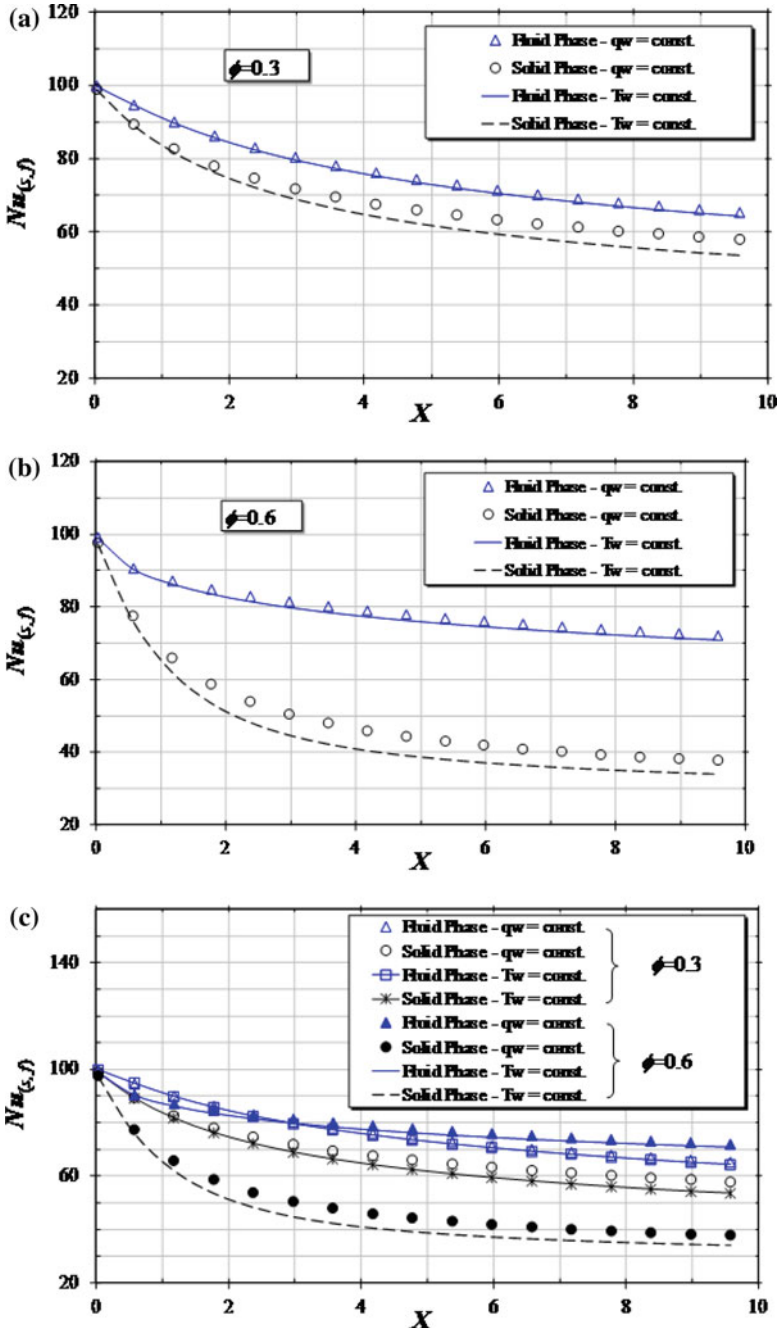

Fig. 2.13 Effect of ϕ on Nu for turbulent flow, $Da = 10^{-4}; Re_D = 5 \times 10^4; D/L = 1.03 \times 10^{-2}$; $k_s/k_f = 25$; **a** $\phi = 0.3$, **b** $\phi = 0.6$, **c** Both ϕ

Figure 2.14 shows the effect of the non-dimensional particle diameter D/L on Nusselt, for a fixed porosity. In general, an increase in the particle diameter D/L results in an increase in Nusselt, for both phases and both boundary condition types (Fig. 2.14a, b). When porosity is constant and the thermal dispersion effects are omitted, the particle diameter only affects h_i and a_i [see Eq. (2.57) and Table 2.1]. A reduced value for D/L with a constant ϕ increases the interstitial area, promoting the exchange of energy between phases, leading to a reduction of the temperature gradients in the wall region, which ultimately reflects on the Nu values. Figure 2.14c compiles such findings and shows for turbulent flow, small differences on Nu prevail in spite of the boundary condition type used.

Effects of the ratio k_s/k_f is presented in Fig. 2.15. All computations made so far were obtained with $k_s/k_f = 25$ and when one compares Fig. 2.15a, b, one can note that the lower such ratio, the closer are the values for the Nusselt numbers, regardless of the boundary condition used. When the fluid and the solid conduct heat at rates of the same order, their temperatures levels do not differ much, with reflection on the proximity of corresponding Nusselt numbers. Further, differences between the Nusselt numbers for $q_w = const.$ and $T_w = const.$ are reduced for the solid, when k_s/k_f is large, and increased for the fluid, for small values of k_s/k_f (Fig. 2.15c).

2.6 Chapter Summary

A computational procedure for determining the convective coefficient of heat exchange between the porous substrate and the working fluid for a porous medium was detailed. As a preliminary result, macroscopically uniform laminar and turbulent flow through a periodic cell of isothermal square rods was computed, considering periodical velocity and temperature fields. Quantitative agreement was obtained when comparing laminar results herein with simulations by Kuwahara et al. [15]. For turbulent flows, Low and High Reynolds turbulence models were employed in order to obtain the interfacial heat transfer coefficient. A correlation was then proposed for such coefficient. Further work will be carried out in order to simulate fully turbulent flow and heat transfer in a porous medium formed by arrays of elliptic, cylindrical and transverse elliptic rods, displaced in in-line as well as staggered arrangements. Ultimately, it is expected that a more general correlation for h_i be obtained to be used in conjunction with macroscopic two-energy equation models.

Also, fully developed forced convection in a porous channel bounded by parallel plates based on a two-energy equation model is analyzed. Details are presented for determining the temperature profile and Nusselt number for laminar flows in a porous medium. Results simulate the effects of Re, ϕ, D and k_s/k_f on Nu. High Re, low porosities, low particle diameters and low thermal conductivity ratios promote thermal equilibrium between phases, eventually leading to higher values of Nu for

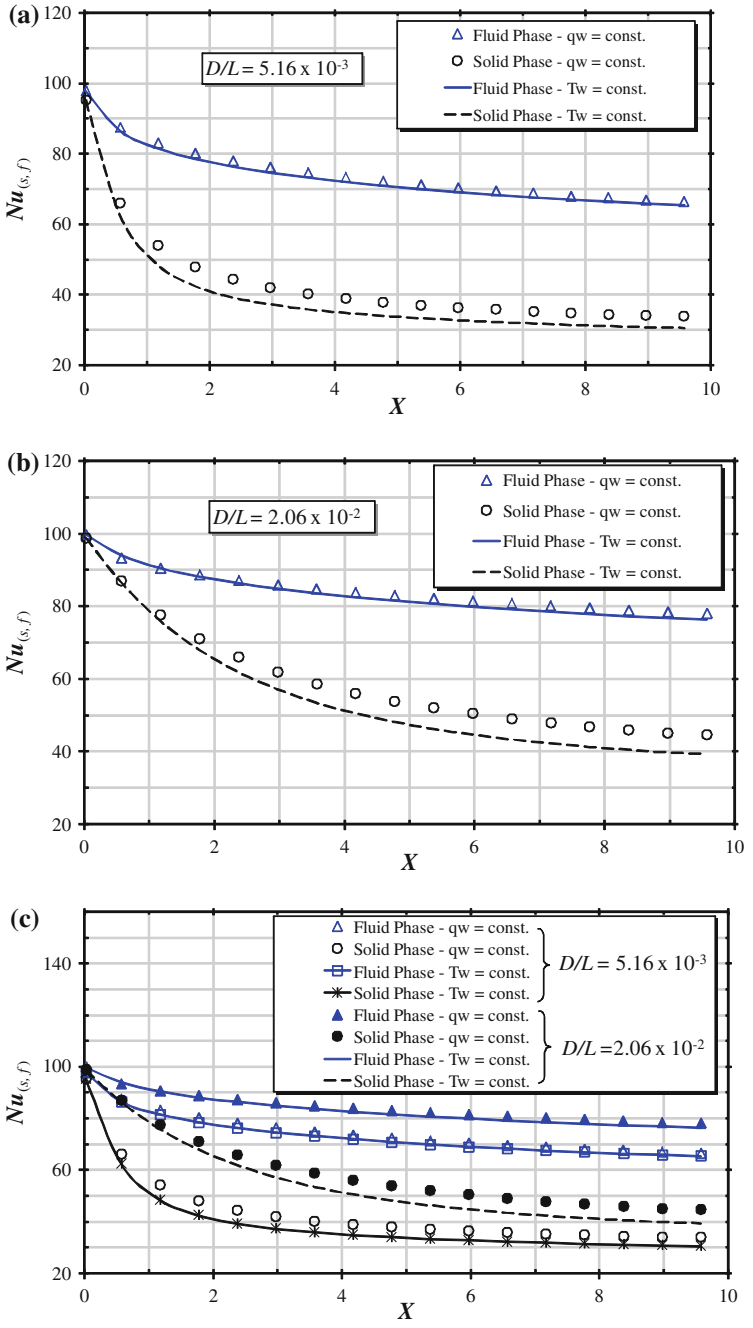

Fig. 2.14 Effect of D/L on Nu for turbulent flow, $Re_D = 5 \times 10^4; \phi = 0.6; k_s/k_f = 25$: **a** $D/L = 5.16 \times 10^{-3}$, **b** $D/L = 2.06 \times 10^{-2}$, **c** Both D/L

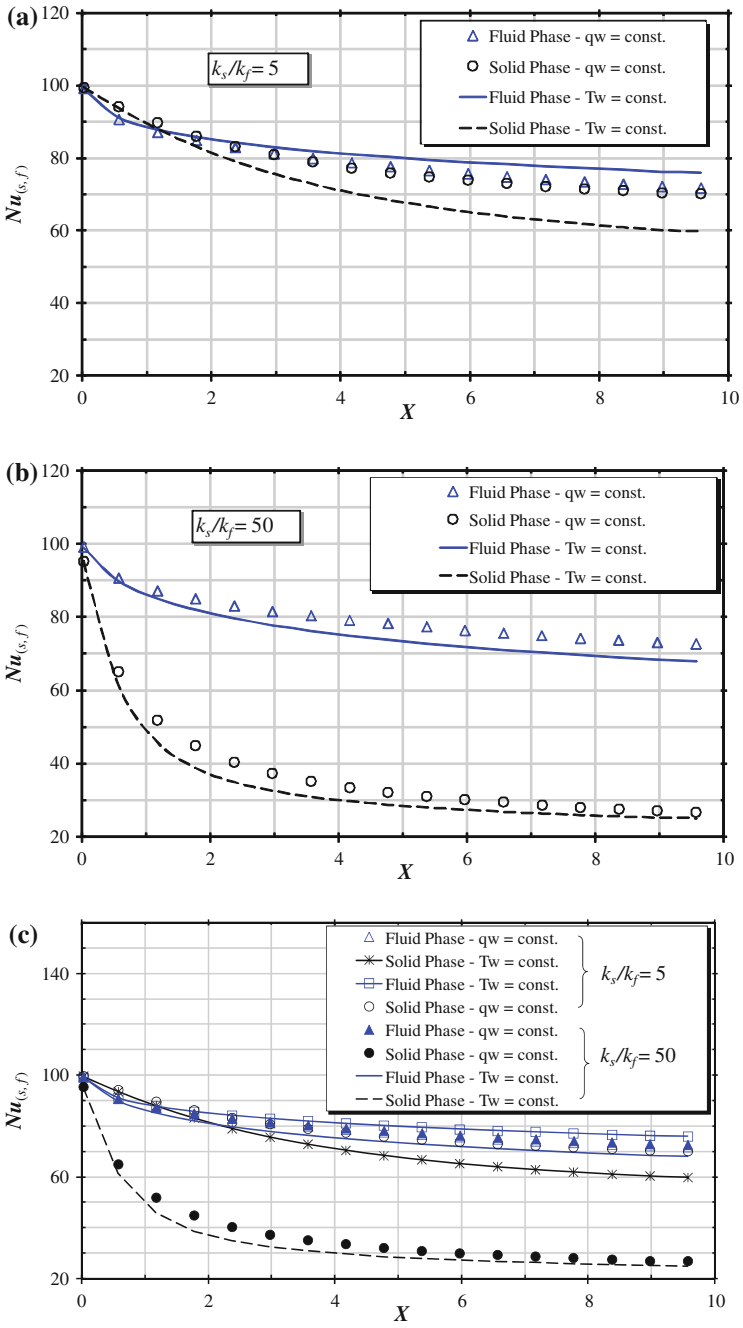

Fig. 2.15 Effect of k_s/k_f on Nu for turbulent flow, $Da = 10^{-4}, Re_D = 5 \times 10^4, \phi = 0.6, D/H = 1.03 \times 10^{-1}$: **a** $k_s/k_f = 5$, **b** $k_s/k_f = 50$

both the fluid and the solid. Further work will be carried out in order to simulate fully turbulent flow and heat transfer in a porous medium with the macroscopic two-energy equation model.

Further, this chapter also investigated the behavior of a two-energy equation model to simulate flow and heat transfer in a porous bed. Effects of thermal dispersion, Reynolds number, particle diameter, porosity and solid-to-fluid thermal conductivity ratio were investigated. The following conclusions were observed:

(1) For laminar flow, the thermal dispersion mechanism promotes energy exchange in the fluid phase, leading to larger local temperature differences when the solid and the fluid temperature are compared along the channel cross-section, particularly at the entry region,
(2) For turbulent flow, the effect of including the thermal dispersion mechanism is concentrated in the region close to the wall, within the boundary layer, where such temperature differences are pronounced,
(3) Increase in *Re* number causes values for *Nu* of both phases to increase and to approach each other,
(4) An increase in porosity causes the solid phase Nusselt number to decrease whereas Nu_f in augmented, for both boundary condition types. A high porosity medium will have the intensity of energy transfer between phases reduced, reflecting in the temperature fields and, ultimately, on the calculated *Nu* values.
(5) A reduced value for D/L with a constant porosity increases the interstitial area, promoting the exchange of energy between phases, leading to a reduction of the temperature gradients in the wall region. In general, an increase in the particle diameter results in an increase in Nusselt, for both phases and both boundary conditions.
(6) The thermal conductivity ratio k_s/k_f causes the most effect on Nusselt numbers, and the grater the ratio, the most wider apart are Nu_s and Nu_f, with a reduction of Nusselt for the solid phase.

References

1. Schumann TEW (1929) Heat transfer: liquid flowing through a porous prism. J Franklin Inst 208:405–416
2. Kaviany M (1995) Principles of heat transfer in porous media, 2nd edn. Springer, New York
3. Quintard M, Kaviany M, Whitaker S (1997) Two-medium treatment of heat transfer in porous media: numerical results for effective properties. Adv Water Resour 20:77–94
4. Ochoa-Tapia JA, Whitaker S (1997) Heat transfer at the boundary between a porous medium and a homogeneous fluid. Int J Heat Mass Transf 40:2691–2707
5. Saito MB, de Lemos MJS (2005) Interfacial heat transfer coefficient for non-equilibrium convective transport in porous media. Int Comm Heat Mass Transf 32(5):667–677

6. de Lemos MJS, Rocamora FD (2002) Turbulent transport modeling for heated flow in rigid porous media. In: Proceedings of the twelfth international heat transfer conference, Grenoble, France, 18–23 Aug 2002, pp 791–795
7. Launder BE, Spalding DB (1974) The numerical computation of turbulent flows. Comp Meth Appl Mech Eng 3:269–289
8. Pedras MHJ, de Lemos MJS (2000) On the definition of turbulent kinetic energy for flow in porous media. Int Comm Heat Mass Transf 27(2):211–220
9. Pedras MHJ, de Lemos MJS (2001) Simulation of turbulent flow in porous media using a spatially periodic array and a low-Re two-equation closure. Numer Heat Transf, Part A Appl 39(1):35–59
10. Pedras MHJ, de Lemos MJS (2003) Computation of turbulent flow in porous media using a Low Reynolds $k - \varepsilon$ model and an infinite array of transversally-displaced elliptic rods, Numer Heat Transf Part A, Appl 43(6):585–602
11. Gray WG, Lee PCY (1977) On the theorems for local volume averaging of multiphase system. Int J Multiph Flow 3:333–340
12. Slattery JC (1967) Flow of viscoelastic fluids through porous media, A I Ch E J 13:1066–1071
13. Kuwahara F, Nakayama A, Koyama H (1996) A numerical study of thermal dispersion in porous media. J Heat Transfer 118:756–761
14. Wakao N, Kaguei S, Funazkri T (1979) Effect of fluid dispersion coefficients on particle-to-fluid heat transfer coefficients in packed bed. Chem Eng Sci 34:325–336
15. Kuwahara F, Shirota M, Nakayama A (2001) A numerical study of interfacial convective heat transfer coefficient in two-energy equation model for convection in porous media. Int J Heat Mass Transf 44:1153–1159
16. Nakayama A, Kuwahara F, Sugiyama M, Xu G (2001) A two-energy equation model for conduction and convection in porous media. Int J Heat Mass Transf 44:4375–4379
17. Patankar SV (1980) Numerical heat transfer and fluid flow. Hemisphere, Washington, DC
18. Zhukauskas A (1972) Heat transfer from tubes in cross flow, advances in heat transfer, 8. Academic Press, New York
19. Alazmi B, Vafai K (2000) Analysis of variants within the porous media transport models. J Heat Transf 122:303–326
20. Saito MB, de Lemos MJS (2009) Laminar heat transfer in a porous channel simulated with a two-energy equation model. Int Commun Heat Mass Transf 36:1002–1007
21. Rocamora FD Jr, de Lemos MJS (2000) Analysis of convective heat transfer of turbulent flow in saturated porous media. Int Comm Heat Mass Transf 27(6):825–834
22. de Lemos MJS, Silva RA (2006) Turbulent flow over a layer of a highly permeable medium simulated with a diffusion-jump model for the interface. Int J Heat Mass Transf 49(3–4):546–556

Chapter 3
Moving Systems

3.1 Introduction

There is an increasing interest in the use of moving bed technology for chemical compound separation, recuperation of petrochemical processes, drying of grains and seeds and removal of organic matter in affluents, to mention a few applications. The advantages of using a moving bed configuration are low investment, low energy consumption, low maintenance and improvement process performance. Accordingly, granular moving bed configurations are present in a number of engineering systems, including those involving iron ore preparation for steel production, for manufacturing of advanced materials and, more recently, for biomass use in environment-friendly energy production equipment. Before proceeding, one should mention that although most applications in industry are concerned with turbulent flow through permeable beds, here only the laminar flow regime is investigated. By that, one can established a consistent line of study in order to analyze turbulent flows with appropriate models in the future.

3.2 Macroscopic Laminar Model for Fixed and Moving Beds

The equations to follow are available in the open literature and for that their derivation are not repeated here [1]. The geometry considered in this work is schematically shown in Fig. 1.3c. Results for counter-flow depicted in Fig. 1.3b are not shown here. In Fig. 1.3d, a moving permeable bed with constant velocity travels along the reactor depicted in the figures. Incoming fluid and solid phase have different temperatures at inlet.

M.J.S. de Lemos, *Thermal Non-Equilibrium in Heterogeneous Media*,
SpringerBriefs in Computational Mechanics,
DOI 10.1007/978-3-319-14666-9_3

3.2.1 Fixed Bed

A macroscopic form of the governing equations is obtained by taking the volumetric average of the entire equation set. In this development, the porous medium is considered to be rigid, fixed and saturated by the incompressible fluid. As mentioned, derivation of this equation set is already available in the literature [1] so that details need not to be repeated here. Nevertheless, for the sake of completeness, the final laminar incompressible form of the equations is here presented:

Continuity:

$$\nabla \cdot \mathbf{u}_D = 0 \tag{3.1}$$

Momentum:

$$\rho\left[\frac{\partial \mathbf{u}_D}{\partial t} + \nabla \cdot \left(\frac{\mathbf{u}_D \mathbf{u}_D}{\phi}\right)\right] = -\nabla(\phi\langle\bar{p}\rangle^i) + \mu\nabla^2\mathbf{u}_D - \left[\frac{\mu\phi}{K}\mathbf{u}_D + \frac{c_F\phi\rho|\mathbf{u}_D|\mathbf{u}_D}{\sqrt{K}}\right] \tag{3.2}$$

where the last two terms in Eq. (3.2) represent the Darcy and Forchheimer contributions.

3.2.2 Moving Bed

For a moving bed, only cases where the solid phase velocity is kept constant will be considered here, or say, we consider here a moving bed that crosses a fixed control volume in addition to a flowing fluid, which is not necessarily moving with a velocity aligned with the solid phase velocity. The steps below show first some basic definitions prior to presenting a proposal for a set of transport equations for analyzing such systems.

A general form for a volume-average of any property φ, distributed within a phase γ that occupy volume ΔV_γ, can be written as [2–4],

$$\langle\varphi\rangle^\gamma = \frac{1}{\Delta V_\gamma}\int_{\Delta V_\gamma} \varphi \, dV_\gamma \tag{3.3}$$

In the general case, the volume ratio occupied by phase γ will be $\phi^\gamma = \Delta V_\gamma/\Delta V$.

If there are two phases, a solid $\gamma = s$ and a fluid phase $\gamma = f$, volume average can be established on both regions. Also,

$$\phi^s = \Delta V_s/\Delta V = 1 - \Delta V_f/\Delta V = 1 - \phi^f \tag{3.4}$$

and for simplicity of notation one can drop the superscript "f" to get

$$\phi^s = 1 - \phi \tag{3.5}$$

As such, calling the instantaneous local velocities for the solid and fluid phases, $\mathbf{u}_s$ and $\mathbf{u}$, respectively, one can obtain the average for the solid velocity, within the solid phase, as follows,

$$\langle \mathbf{u} \rangle^s = \frac{1}{\Delta V_s} \int_{\Delta V_s} \mathbf{u}_s \, dV_s \tag{3.6}$$

with, in turn, can be related to an average velocity referent to the entire REV as,

$$\mathbf{u}_S = \overbrace{\frac{\Delta V_s}{\Delta V}}^{(1-\phi)} \underbrace{\frac{1}{\Delta V_s} \int_{\Delta V_s} \mathbf{u}_s \, dV_s}_{\langle \mathbf{u} \rangle^s} \tag{3.7}$$

A further approximation herein is that the porous bed is kept rigid and moves with a steady average velocity $\mathbf{u}_s$.

Both velocities can then be written as,

$$\mathbf{u}_D = \phi \langle \mathbf{u} \rangle^i \text{ and } \mathbf{u}_s = (1 - \phi) \langle \mathbf{u} \rangle^s = const \tag{3.8}$$

A relative velocity is then defined as,

$$\mathbf{u}_{rel} = \mathbf{u}_D - \mathbf{u}_S \tag{3.9}$$

Assuming that the relative movement between the two phases is macroscopically described by Eq. (3.9), the momentum equation reads,

$$\rho \left[\frac{\partial \mathbf{u}_D}{\partial t} + \nabla \cdot \left(\frac{\mathbf{u}_D \mathbf{u}_D}{\phi} \right) \right] = -\nabla (\phi \langle \bar{p} \rangle^i) + \mu \nabla^2 \mathbf{u}_D - \underbrace{\left[\frac{\mu \phi}{K} \mathbf{u}_{rel} + \frac{c_F \phi \rho \, |\mathbf{u}_{rel}| \mathbf{u}_{rel}}{\sqrt{K}} \right]}_{relative\ drag}, \tag{3.10}$$

3.3 Turbulence Model for Flow Equations

As mentioned, the equations to follow are available in the open literature [1]. For turbulent flow, the geometry considered is also schematically shown in Fig. 1.3a. A moving porous bed co-flows with a permeating fluid and both, the solid matrix as well as the working fluid, move in the same west-to-east direction. The channel

shown in the figure has length and height given by L and H, respectively. For the sake of completeness, equations for turbulent flow for both fixed and moving medium are presented below.

3.3.1 Fixed Bed

A macroscopic form of the governing equations is obtained by taking the volumetric average of the entire equation set. In this development, the porous medium is considered to be rigid, fixed and saturated by the incompressible fluid. The final forms of the equations considered here for turbulent flow are [1]:

Continuity:

$$\nabla \cdot \bar{\mathbf{u}}_D = 0 \tag{3.11}$$

Momentum:

$$\rho\left[\nabla \cdot \left(\frac{\bar{\mathbf{u}}_D \bar{\mathbf{u}}_D}{\phi}\right)\right] = -\nabla(\phi\langle\bar{p}\rangle^i) + \mu\nabla^2\bar{\mathbf{u}}_D + \nabla \cdot (-\rho\phi\langle\overline{\mathbf{u}'\mathbf{u}'}\rangle^i) - \left[\frac{\mu\phi}{K}\bar{\mathbf{u}}_D + \frac{c_F\phi\rho\,|\bar{\mathbf{u}}_D|\bar{\mathbf{u}}_D}{\sqrt{K}}\right], \tag{3.12}$$

Turbulent kinetic energy:

$$\rho\nabla \cdot \left(\bar{\mathbf{u}}_D\langle k\rangle^i\right) = \nabla \cdot \left[\left(\mu + \frac{\mu_{t_\phi}}{\sigma_k}\right)\nabla\left(\phi\langle k\rangle^i\right)\right] + P^i + G^i - \rho\phi\langle\varepsilon\rangle^i \tag{3.13}$$

Dissipation rate of turbulence kinetic energy:

$$\rho\nabla.\left(\bar{\mathbf{u}}_D\langle\varepsilon\rangle^i\right) = \nabla \cdot \left[\left(\mu + \frac{\mu_{t_\phi}}{\sigma_\varepsilon}\right)\nabla\left(\phi\langle\varepsilon\rangle^i\right)\right] + c_1P^i\frac{\langle\varepsilon\rangle^i}{\langle k\rangle^i} + c_2\frac{\langle\varepsilon\rangle^i}{\langle k\rangle^i}\left(G^i - \rho\phi\langle\varepsilon\rangle^i\right) \tag{3.14}$$

where $\bar{\mathbf{u}}_D$ is the time-averaged Darcy velocity vector, $\bar{\mathbf{u}}_D = \phi\langle\bar{\mathbf{u}}\rangle^i$, ϕ is the porosity, ρ is the density of the fluid, p is the pressure, μ is the fluid dynamic viscosity, K is the medium permeability, c_F is the Forchheimer coefficient, μ_{t_ϕ} is the macroscopic turbulent viscosity, σ_k and σ_ε are constants, $\langle k\rangle^i$ is the intrinsic (fluid) average of k and $\langle\varepsilon\rangle^i$ is the intrinsic dissipation rate of $\langle k\rangle^i$, $\varepsilon = \mu\overline{\nabla\mathbf{u}' : (\nabla\mathbf{u}')^T}\Big/\rho$. In Eq. (3.14), c_1 and c_2 are constants, $P^i = -\rho\langle\overline{\mathbf{u}'\mathbf{u}'}\rangle^i : \nabla\bar{\mathbf{u}}_D$ is the production rate of $\langle k\rangle^i$ due to gradients of $\bar{\mathbf{u}}_D$ and $G^i = c_k\rho\phi\,\langle k\rangle^i\,|\bar{\mathbf{u}}_D|\Big/\sqrt{K}$ is the generation rate of the intrinsic average of k due to the action of the porous matrix (see [1] for details):

3.3.2 Moving Bed

As before, only cases where the solid phase velocity is given a constant will be considered. Further, for turbulent flows the phase velocities read,

$$\bar{\mathbf{u}}_D = \phi\langle\bar{\mathbf{u}}\rangle^i, \mathbf{u}_S = (1-\phi)\langle\mathbf{u}\rangle^s = const. \tag{3.15}$$

with a relative velocity,

$$\bar{\mathbf{u}}_{rel} = \bar{\mathbf{u}}_D - \mathbf{u}_S \tag{3.16}$$

In addition, a relative Reynolds number based on $\bar{\mathbf{u}}_{rel}$ and D can be defined as:

$$\mathrm{Re}_D = \frac{\rho\,|\bar{\mathbf{u}}_{rel}|\,D}{\mu} \tag{3.17}$$

Further, if one uses the Darcy velocity and the overall reactor size H, one has a different definition for Reynolds given by,

$$\mathrm{Re} = \frac{\rho\,|\bar{\mathbf{u}}_D|\,H}{\mu} \tag{3.18}$$

Incorporating now in Eq. (3.12) a model for the Macroscopic Reynolds Stresses $-\rho\phi\langle\overline{\mathbf{u}'\mathbf{u}'}\rangle^i$, and assuming that a relative movement between the two phases is described by Eq. (3.16), the momentum equation reads (see [1, 5] for details),

$$\begin{aligned}\rho\left[\nabla\cdot\left(\frac{\bar{\mathbf{u}}_D\bar{\mathbf{u}}_D}{\phi}\right)\right] - \nabla\cdot\left\{\left(\mu+\mu_{t_\phi}\right)\left[\nabla\bar{\mathbf{u}}_D + (\nabla\bar{\mathbf{u}}_D)^T\right]\right\} \\ = -\nabla(\phi\langle\bar{p}\rangle^i) - \frac{\mu\phi}{K}\bar{\mathbf{u}}_{rel} + \frac{c_F\phi\rho|\bar{\mathbf{u}}_{rel}|\bar{\mathbf{u}}_{rel}}{\sqrt{K}}\end{aligned} \tag{3.19}$$

where μ_{t_ϕ} is the macroscopic eddy viscosity given by

$$\mu_{t_\phi} = \rho\, c_\mu f_\mu \frac{\langle k\rangle^{i^2}}{\langle\varepsilon\rangle^i}, \tag{3.20}$$

c_μ is dimensionless constant and f_μ is a damping function, which differs from unit if a Low-Reynolds turbulence model is applied. More on damping functions and model constants will be shown below. Thus, to obtain the eddy viscosity, μ_{t_ϕ}, we used here the Low and High Reynolds number $k-\varepsilon$ models, whose equations for the turbulent kinetic energy and its dissipation rate, incorporating now a relative movement between the two phases $|\bar{\mathbf{u}}_{rel}|$, are given next [5].

A transport equation for $\langle k\rangle^i$ can be written as,

$$\rho\left[\nabla\cdot(\bar{\mathbf{u}}_D\langle k\rangle^i)\right] = \nabla\cdot\left[(\mu+\frac{\mu_{t_\phi}}{\sigma_k})\nabla(\phi\langle k\rangle^i)\right] - \rho\langle\overline{\mathbf{u}'\mathbf{u}'}\rangle^i : \nabla\bar{\mathbf{u}}_D + \underbrace{c_k\,\rho\frac{\phi\langle k\rangle^i|\bar{\mathbf{u}}_{rel}|}{\sqrt{K}}}_{G^i} - \rho\phi\langle\varepsilon\rangle^i \tag{3.21}$$

where σ_k and c_k are dimensionless constants and the generation rate due to the porous substrate, G^i, which was included in Eq. (3.13), now depends on $|\bar{\mathbf{u}}_{rel}|$ and reads,

$$G^i = c_k\rho\phi\,\langle k\rangle^i|\bar{\mathbf{u}}_{rel}|\Big/\sqrt{K} \tag{3.22}$$

A corresponding transport equation for $\langle\varepsilon\rangle^i$, incorporating also the relative velocity $|\bar{\mathbf{u}}_{rel}|$, can be written as,

$$\rho\left[\frac{\partial}{\partial t}(\phi\langle\varepsilon\rangle^i)+\nabla\cdot(\bar{\mathbf{u}}_D\langle\varepsilon\rangle^i)\right] = \nabla\cdot\left[(\mu+\frac{\mu_{t_\phi}}{\sigma_\varepsilon})\nabla(\phi\langle\varepsilon\rangle^i)\right] + c_1(-\rho\langle\overline{\mathbf{u}'\mathbf{u}'}\rangle^i:\nabla\bar{\mathbf{u}}_D)\frac{\langle\varepsilon\rangle^i}{\langle k\rangle^i} + c_2c_k\rho\frac{\phi\,\langle\varepsilon\rangle^i|\bar{\mathbf{u}}_{rel}|}{\sqrt{K}} - c_2f_2\rho\phi\frac{\langle\varepsilon\rangle^{i^2}}{\langle k\rangle^i} \tag{3.23}$$

where σ_ε, c_1 and c_2 are constants and f_2 is a damping function.

3.4 Thermal Transport

3.4.1 Two-Energy Equation Model

As for the flow, the macroscopic equations to heat transport in porous media are obtained by applying the average volume to microscopic equations. The mathematical model used to describe the heat transfer between the solid and fluid in a unit of moving bed is based on the two-energy equations model, which can be written as:

$$\left\{(\rho c_p)_f\phi\right\}\frac{\partial\langle T_f\rangle^i}{\partial t} + (\rho c_p)_f\nabla\cdot(\mathbf{u}_D\langle T_f\rangle^i) = \nabla\cdot\left\{\mathbf{K}_{eff,f}\cdot\nabla\langle T_f\rangle^i\right\} + h_ia_i(\langle T_s\rangle^i-\langle T_f\rangle^i) \tag{3.24}$$

$$\left\{(1-\phi)(\rho c_p)_s\right\}\frac{\partial\langle T_s\rangle^i}{\partial t} + (\rho c_p)_s\nabla\cdot(\mathbf{u}_S\langle T_s\rangle^i) = \nabla\cdot\left\{\mathbf{K}_{eff,s}\cdot\nabla\langle T_s\rangle^i\right\} - h_ia_i(\langle T_s\rangle^i-\langle T_f\rangle^i) \tag{3.25}$$

where, $\mathbf{K}_{eff,f}$ and $\mathbf{K}_{eff,s}$ are the effective conductivity tensors for fluid and solid, respectively, given by:

$$\mathbf{K}_{eff,f} = [\phi\, k_f]\, \mathbf{I} + \mathbf{K}_{f,s} + \mathbf{K}_{disp} \tag{3.26}$$

$$\mathbf{K}_{eff,s} = [(1-\phi)\, k_s]\, \mathbf{I} + \mathbf{K}_{s,f} \tag{3.27}$$

where $\mathbf{I}$ is the unit tensor and $\mathbf{K}_{disp}$, $\mathbf{K}_{f,s}$ and $\mathbf{K}_{s,f}$ are coefficients defined as,

$$\text{Thermal dispersion}: -(\rho\, c_p)_f\, (\phi\ \langle {}^i\mathbf{u}^i T_f \rangle^i\ ) = \mathbf{K}_{disp} \cdot \nabla \langle T_f \rangle^i \tag{3.28}$$

$$\text{Local conduction}: \begin{cases} \nabla \cdot \left[\dfrac{1}{\Delta V} \displaystyle\int_{A_i} \mathbf{n}_i\, k_f T_f\, dA \right] = \mathbf{K}_{f,s} \cdot \nabla \langle T_s \rangle^i \\ -\nabla \cdot \left[\dfrac{1}{\Delta V} \displaystyle\int_{A_i} \mathbf{n}_i\, k_s T_s\, dA \right] = \mathbf{K}_{s,f} \cdot \nabla \langle T_f \rangle^i \end{cases} \tag{3.29}$$

where $\mathbf{n}_i$ in (3.29) as already noted, is the unit vector pointing outwards of the fluid phase. In this work, for simplicity, one assumes that the overall thermal resistance between the two phases is controlled by the interfacial film coefficient, which considers the boundary layer at the solid-fluid interface, rather than by the thermal resistance within the solid and the fluid phases. Such an assumption might be more valid for turbulent flows, but here it is also employed for laminar cases in the absence of better information. As such, the local conduction coefficients $\mathbf{K}_{f,s}, \mathbf{K}_{s,f}$ are here neglected for the sake of simplicity. Additional information on the models in Eqs. (3.26) and (3.27) can be found in [6].

Non-dimensional temperatures for the solid and fluid are defined as:

$$\theta_{s,f} = \frac{\langle T_{s,f} \rangle^i - T_{\min}}{T_{\max} - T_{\min}} \tag{3.30}$$

where the subscripts s,f stands for the solid and fluid phases, respectively, and "max" and "min" refers to both temperature maximum and minimum of either phase.

3.4.2 Interfacial Heat Transfer Coefficient

The heat transferred between the two phases was modeled by means of a film coefficient h_i, or interstitial heat transfer coefficient, present in Eqs. (3.24) and (3.25), such that,

$$h_i a_i \left(\langle T_s \rangle^i - \langle T_f \rangle^i \right) = \frac{1}{\nabla V} \int_{A_i} \mathbf{n}_i \cdot k_f \nabla T_f dA = \frac{1}{\Delta V} \int_{A_i} \mathbf{n}_i \cdot k_s \nabla T_s \, dA \tag{3.31}$$

where A_i is the interfacial area between the two phases and a_i is the interfacial area per unit volume or $a_i = A_i / \nabla V$. The high values of a_i make them attractive for transferring thermal energy via conduction through the solid followed by convection to a fluid stream.

Wakao et al. [7] obtained a heuristic correlation for a closely packed bed of particle diameter D and compared their results with experimental data. This correlation for the interfacial heat transfer coefficient is given by,

$$\frac{h_i D}{k_f} = 2 + 1.1 Re_D^{0.6} Pr^{1/3}, \text{ for } \phi > 0.9 \tag{3.32}$$

Further, a numerical correlation for the interfacial convective heat transfer coefficient was proposed by Kuwahara et al. [8] for a laminar flow as,

$$\frac{h_i D}{k_f} = \left(1 + \frac{4(1-\phi)}{\phi} \right) + \frac{1}{2} (1-\phi)^{1/2} Re_D Pr^{1/3}, \text{ valid for } 0.2 < \phi < 0.9. \tag{3.33}$$

Results in Eq. (3.33) depend on the porosity and are valid for packed beds of particle diameter D. In addition, Saito and de Lemos (2005) [9] also obtained the interfacial heat transfer coefficient for laminar flows through an infinite square rod array using the same methodology as Kuwahara et al. (2001) [8].

The interstitial heat transfer coefficient h_i is calculated by correlations Eq. (3.33) for laminar flow and Eq. (2.57) for turbulent flow (see also Chap. 2 and Table 2.1). However, since the relative movement between phases is seen as the promoter of convective heat transport from the fluid to the solid, or vice versa, a relative Reynolds number defined as,

$$Re_D = \frac{\rho |\mathbf{u}_{rel}| D}{\mu} \tag{3.34}$$

is used in the correlations Eqs. (2.57) and (3.33) instead of a Reynolds number based on the absolute velocity of the fluid phase. Accordingly, when the solid phase

velocity approaches the fluid velocity, the only mechanism for transferring heat between phases is conduction.

3.4.3 Wall Treatment and Boundary Conditions

In this work, two forms of the $k - \varepsilon$ model are employed, namely the High Reynolds and Low Reynolds number turbulence models. For the High Reynolds turbulence model, a macroscopic form of the standard $k - \varepsilon$ closure was used (Launder and Spalding (1974) [10]) whereas for the Low Reynolds number model constants and damping functions of Abe et al. (1992) [11] were applied. All model constants and damping functions for both turbulence models are compiled in Table 3.1.

Boundary conditions are given by:

On the solid walls:

$$\langle \mathbf{u} \rangle^i = 0, q_w = 0 \tag{3.35}$$

On the entrance:

$$\mathbf{u}_D = \mathbf{u}_{inlet}, \langle T_f \rangle^i = T^f_{inlet}, \langle T_s \rangle^i = T^s_{inlet}. \tag{3.36}$$

On the solid walls (Low Reynolds turbulence model):

$$\bar{u} = 0,\ k = 0,\ \varepsilon = v\frac{\partial^2 k}{\partial y^2} \tag{3.37}$$

Table 3.1 Damping functions and constants for high and low Reynolds turbulence models

High Reynolds model proposed by Launder and Spalding (1974) [10]		Low Reynolds model proposed by Abe et al. (1992) [11]
f_μ	1.0	$\left\{1 - \exp\left[-\frac{(v\varepsilon)^{0.25} y}{14v}\right]\right\}^2 \left\{1 + \frac{5}{(k^2/v\varepsilon)^{0.75}} \exp\left[-\left(\frac{(k^2/v\varepsilon)}{200}\right)^2\right]\right\}$
f_2	1.0	$\left\{1 - \exp\left[-\frac{(v\varepsilon)^{0.25} y}{3.1v}\right]\right\}^2 \left\{1 - 0.3 \exp\left[-\left(\frac{(k^2/v\varepsilon)}{6.5}\right)^2\right]\right\}$
σ_k	1.0	1.4
σ_ε	1.33	1.3
c_1	1.44	1.5
c_2	1.92	1.9

On the solid walls (High Reynolds turbulence model):

$$\frac{\bar{u}}{u_\tau} = \frac{1}{\kappa}\ln(y^+ E),\ k = \frac{u_\tau^2}{c_\mu^{1/2}},\ \varepsilon = \frac{c_\mu^{3/4} k_w^{3/2}}{\kappa y_w} \tag{3.38}$$

with, $u_\tau = \left(\frac{\tau_w}{\rho}\right)^{1/2}$, $y_w^+ = \frac{y_w u_\tau}{v}$, where u_τ is wall-friction velocity, y_w is the non-dimensional coordinate normal to wall, κ is the von Kármán constant, and E is a constant that depends on the roughness of the wall. For smooth walls, E = 9.

On the entrance:

$$\bar{\mathbf{u}}_D = \mathbf{u}_{inlet} \tag{3.39}$$

At exit, zero diffusion flux is considered for all variables.

3.5 Results for Laminar Parallel Flow

The problem under investigation is a laminar flow through a channel completely filled with a moving layer of a porous material, as depicted in Fig. 1.3a. The channel shown in Fig. 1.3a has length and height given by L and H, respectively. As mentioned previously, the geometry of Fig. 1.3a was numerically investigated using the control-volume method of Fig. 1.3b. The porous matrix moves with constant velocity $\mathbf{u}_s$. Here, validation of the presented simulations considered a fixed solid matrix, i.e., $\mathbf{u}_S/\mathbf{u}_D = 0$, for which an analytical solution is available in the literature [11]. Additional results follow taking into consideration $\mathbf{u}_S/\mathbf{u}_D > 0$. All runs for moving bed cases are detailed in Table 3.2. Also, the fluid and solid phases are given different temperatures at the inlet.

3.5.1 *Effect of Reynolds Number, Re_D*

Figure 3.1a shows values for the longitudinal non-dimensional temperature profiles as a function of Re_D. The Reynolds number was calculated based on relative velocity $\mathbf{u}_{rel}$ and for a slip ratio $u_S/u_D = 0.5$. As such, for increasing Re_D while keeping u_S/u_D constant, both the fluid and the solid phases had to increase according to the relationship for concurrent flow,

Table 3.2 Cases and parameters used for laminar flow (Sect. 3.2)

Cases investigated	Dimensional				Non-dimensional					
	u_D (m/s)	u_S (m/s)	u_{rel} (m/s)	K (m^2)	Re_D	u_s/u_D	Da	ϕ	$(\rho c_p)_s/(\rho c_p)_f$	k_s/k_f
Effect of Re_D	5.666E-02	2.833E-02	2.833E-02	2.025E-05	1.00E01	5.0E-01	3.371E-03	0.9	1.5E00	2.5E01
	2.833E-01	1.416E-01	1.417E-01		5.00E01					
	5.666E-01	2.833E-01	2.833E-01		1.00E02					
Effect of u_S/u_D	2.833E-01	0.000E00	2.833E-01	2.025E-05	1.00E02	0.0E00	3.371E-03	0.9	1.5E00	2.5E01
		7.083E-02	2.125E-01		7.50E01	2.5E-01				
		1.416E-01	1.417E-01		5.00E01	5.0E-01				
		2.125E-01	7.083E-02		2.50E01	7.5E-01				
		2.692E-01	1.417E-02		5.00E00	9.5E-01				
Effect of Da	2.125E-01	1.062E-01	1.062E-01	5.625E-07	6.25E00	5.0E-01	9.365E-05	0.9	1.5E00	2.5E01
				5.062E-06	1.87E01		8.429E-04			
				5.625E-05	6.25E01		9.365E-03			
Effect of ϕ	2.125E-01	1.062E-01	1.062E-01	3.086E-07	6.25E01	5.0E-01	5.139E-05	0.4	1.5E00	2.5E01
				1.562E-06			2.601E-04	0.6		
				1.111E-05			1.850E-03	0.8		
Effect of $(\rho c_p)_s/(\rho c_p)_f$	2.125E-01	1.062E-01	1.062E-01	9.000E-06	2.50E01	5.0E-01	1.498E-03	0.9	2.5E-01	2.5E01
									5.0E-01	
									1.0E00	
									1.0E01	
Effect of k_s/k_f, $u_S/u_D = 0$	2.125E-01	0.000E00	2.125E-01	1.562E-06	1.25E02	0.0E00	2.601E-04	0.6	1.5E00	1.0E00
										1.0E01
										1.0E02
										1.0E03

(continued)

Table 3.2 (continued)

Cases investigated	Dimensional				Non-dimensional					
	u_D (m/s)	u_S (m/s)	u_{rel} (m/s)	K (m^2)	Re_D	u_s/u_D	Da	ϕ	$(\rho c_p)_s/(\rho c_p)_f$	k_s/k_f
Effect of k_s/k_f, $u_S/u_D = 0.1$	2.125E-01	2.125E-2	1.912E-01	1.562E-06	1.12E02	1.0E-01	2.601E-04	0.6	1.5E00	1.0E00
										1.0E01
										1.0E02
										1.0E03
Effect of k_s/k_f, $u_S/u_D = 0.4$	2.125E-01	8.500E-2	1.275E-01	1.562E-06	7.50E01	4.0E-01	2.601E-04	0.6	1.5E00	1.0E00
										1.0E01
										1.0E02
										1.0E03

$$Re_D = \frac{\rho\, u_{rel}\, D}{\mu} = \frac{\rho\, u_D D}{\mu}\left(1 - \frac{u_S}{u_D}\right) = Re\left(1 - \frac{u_S}{u_D}\right) \tag{3.40}$$

Back to Fig. 3.1, one can see that the cold fluid is heated up as it permeates the hot porous structure. Also, because the magnitude of both velocities increase for a higher Re_D, one can see that the axial length needed for reaching the equilibrium value is increased as Re_D increases.

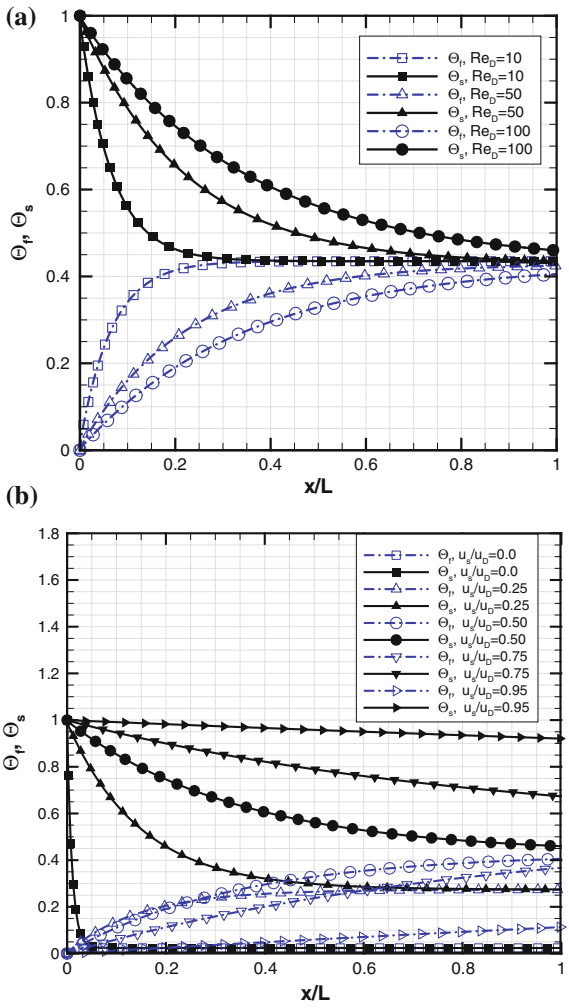

Fig. 3.1 Non-dimensional temperatures for $k_s/k_f = 25$, $\phi = 0.9$, $Da = 3.371 \times 10^{-3}$, $(\rho c_p)_s/(\rho c_p)_f = 1.5$; **a** as a function of Re_D, $u_s/u_D = 0.5$, **b** as a function of u_s/u_D

3.5.2 Effect of Slip Ratio, u_s/u_D

Figure 3.1b shows temperature profiles for a moving bed, as a function of $\mathbf{u}_s/\mathbf{u}_D$. It is observed that the higher the value of $\mathbf{u}_s/\mathbf{u}_D$, the greater is the temperature difference between fluid and solid phases. The stronger axial convection due to a higher u_s brings more solid phase energy into the reactor, leading to high values of the solid temperature along the axial direction. In addition, increasing $\mathbf{u}_s/\mathbf{u}_D$ for the same fluid velocity leads to a raise in the equilibrium temperature as more thermal energy is brought into the system. When the solid velocity approaches that of the fluid, the velocity of the solid phase becomes large, leading to a longer equilibrium length. Further, decreasing the relative velocity between phases as u_s increases reduces the interstitial heat transfer rate and, consequently, exchange of heat between phases becomes mostly governed by conduction, which further contributes towards a longer axial length for thermal equilibrium to be established.

3.5.3 Effect of Darcy Number, Da

Figure 3.2a presents the effect of particle diameter D on the axial temperature profiles. For a give particle diameter, permeability is given according to the Ergun equation by (see [9]):

$$K = \frac{D^2\phi^2}{144(1-\phi)^2} \tag{3.41}$$

leading to a Darcy number $Da = K/H^2$ where H is the height of channel. The Reynolds number and the porosity are kept constant for all curves. It is observed in Fig. 3.2 that for a small permeability, as a result of a decrease of particle diameter while keeping the porosity constant, a larger interfacial heat transfer area promotes heat transfer between phases and reduces the length necessary for thermal equilibrium to be reached.

3.5.4 Effect of Porosity, ϕ

Figure 3.2b shows the effect of porosity on the longitudinal temperature distribution. The Reynolds number Re_D, the velocity ratio between the solid and fluid phases $u_S/u_D = 0.5$ and the ratio of thermal capacity $(\rho c_p)_s/(\rho c_p)_f = 1.5$ are kept constant for all curves. For a small porosity, a larger interfacial heat transfer area promotes heat transfer between phases and reduces the length necessary for thermal equilibrium to be reach. Also, for a fixed Reynolds number based on $u_D = \phi\langle u\rangle^i$, an increase in porosity corresponds to a reduction in the fluid velocity $\langle u\rangle^i$, which

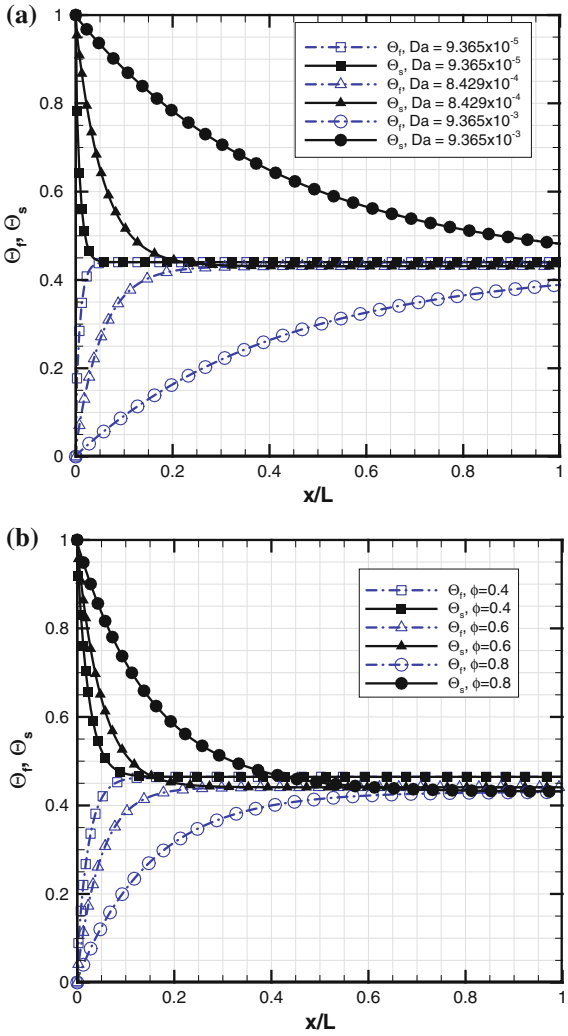

Fig. 3.2 Non-dimensional temperatures for $u_s/u_D = 0.5$, $(\rho c_p)_s/(\rho c_p)_f = 1.5$, $k_s/k_f = 25$; **a** as a function of Da, $\phi = 0.9$, **b** as a function of ϕ, $Re_D = 62.5$

further reduces the cooling effect by reducing the interfacial heat transfer coefficient h_i between phases. Consequently, the product $h_i a_i$ will be decreased as porosity ϕ increases, which indicates damping of convective transfer through the interfacial area.

3.5.5 *Effect of Thermal Capacity Ratio* $(\rho c_p)_s/(\rho c_p)_f$

Figure 3.3 shows the effect of the thermal capacity ratio on dimensionless temperature distribution along the axial direction. The density and specific heat of the

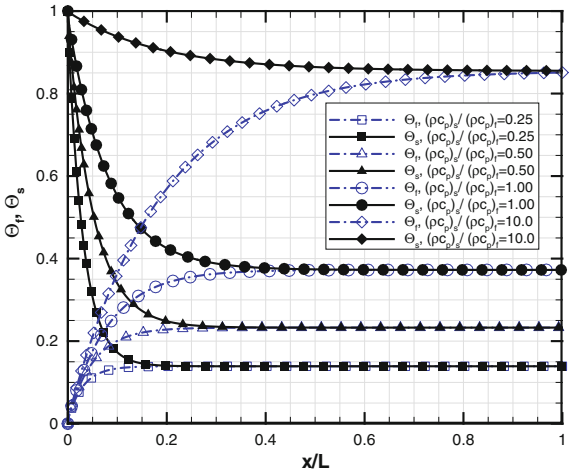

Fig. 3.3 Non-dimensional temperatures as a function of $(\rho c_p)_s/(\rho c_p)_f$, $u_s/u_D = 0.5$, $k_s/k_f = 25$, $\varphi = 0.9$, $Da = 1.498 \times 10^{-3}$, $Re_D = 25$

fluid are kept constant given by $\rho = 0.4345\,\text{kg/m}^3$ and $(c_p)_f = 1986.8\,\text{J/kg K}$ respectively. It is observed in Fig. 3.3 that increasing the thermal capacity of the solid $(\rho c_p)_s$, the equilibrium temperature tends to approach the inlet of the solid, or say, for higher values of $(\rho c_p)_s$ more energy exchange is needed to vary the temperature of the solid by a certain amount.

3.5.6 *Effect of Thermal Conductivity Ratio k_s/k_f*

Figure 3.4a shows the effect of k_s/k_f on longitudinal non-dimensional temperatures. It is noted that the higher the ratio k_s/k_f, the longer is the length needed for thermal development since heat is transported only by conduction within the solid, which causes its temperature distribution to be more connected to the inlet temperature. In addition, a longer developing length and a higher equilibrium temperature are obtained as k_s/k_f increases.

With increasing k_s/k_f for $u_s/u_D = 0.1$ (Fig. 3.4b), also here we can note higher solid temperatures along the reactor as well higher equilibrium temperatures of the system. Enhancing convection of the solid also raises the equilibrium temperature (see Fig. 3.4b), which can be better seen when comparing corresponding final equilibrium values for $k_s/k_f = 1$ in Figs. 3.4a and 3.6b. On the other hand, by decreasing the thermal conductivity ratio, also here a shorter axial length is needed for the equilibrium temperature to be reached.

Further increasing the slip ratio to $u_s/u_D = 0.4$ (Fig. 3.4c), one can see that the axial convection strength of the solid for $k_s/k_f = 1$, when compared to the similar

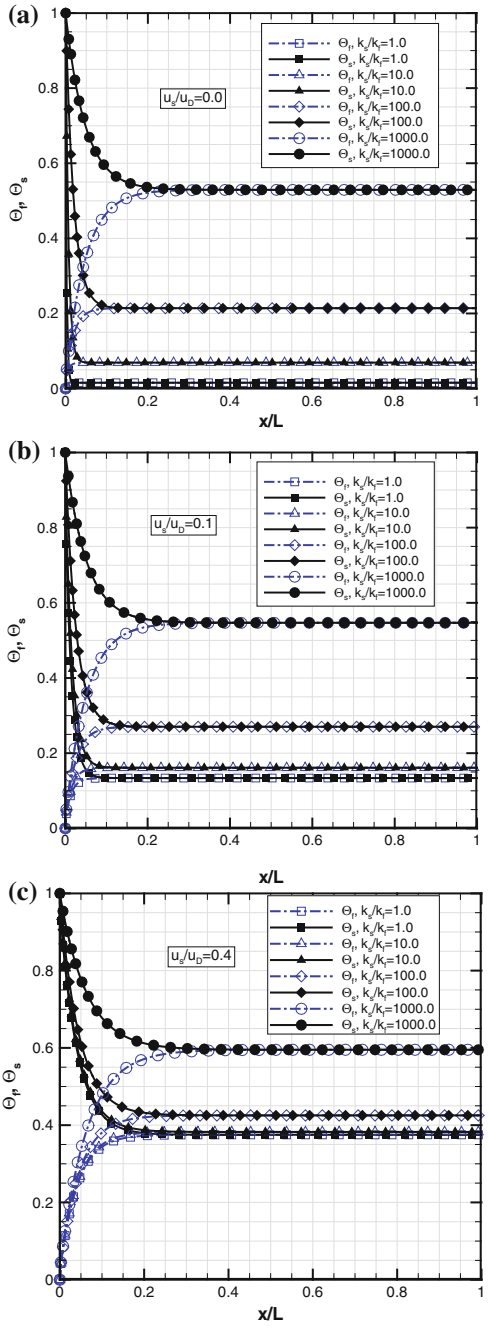

Fig. 3.4 Non-dimensional temperatures as a function of k_s/k_f, $\phi = 0.6$, $Da = 2.601 \times 10^{-4}$, $(\rho c_p)_s/(\rho c_p)_f = 1.5$; **a** $u_s/u_D = 0.0$, **b** $u_s/u_D = 0.1$, **c** $u_s/u_D = 0.4$

cases in Fig. 3.6a, b, yield the most significant changes in raising the equilibrium temperature. For example, nondimensional equilibrium temperatures rise from around 0.02 for $u_s/u_D = 0$ and $k_s/k_f = 1$ (Fig. 3.4a) to more than 0.35 for $u_s/u_D = 0.4$ and the same thermal conductivity ratio equal to unity (Fig. 3.4a).

Therefore, when comparing the two mechanisms, namely advection and conduction of the solid phase, higher ratios k_s/k_f have less impact on raising the equilibrium temperature than the increase in the velocity ratio u_s/u_D.

3.6 Results for Turbulent Parallel Flow

As mentioned, this chapter presents results for both laminar and turbulent flow in a channel containing a moving porous bed as shown in Fig. 1.3a. Data for all runs are detailed in Tables 3.3 and 3.4.

3.6.1 Effect of Reynolds Number, Re_D

The Reynolds number Re_D was calculated based on relative velocity $\bar{\mathbf{u}}_{rel}$ for high and low Reynolds models. It is noticed that when Darcy velocity $\bar{u}_D$ increases while keeping the same porosity and slip ratio, there is an increase in the relative velocity $\bar{\mathbf{u}}_{rel}$ (see Tables 3.3 and 3.4). Accordingly, Fig. 3.5a, b shows that when the relative velocity increases, a greater amount of mean mechanical energy is converted into turbulence, regardless of the turbulence model used. Or say, as the relative fluid velocity increases past the solid obstacles, the amount of fluid disturbance is increased leading to an increase in the final level of $\langle k \rangle^i$. That can be seen by inspecting the generation term $G^i = c_k \rho \phi \langle k \rangle^i |\bar{\mathbf{u}}_{rel}| / \sqrt{K}$ that is proportional to $\bar{\mathbf{u}}_{rel}$.

3.6.2 Effect of Slip Ratio, u_s/u_D

Figure 3.6a, b indicate the damping of turbulence as the solid velocity approaches that of the flowing fluid. As the relative velocity $\bar{\mathbf{u}}_{rel}$ decreases, the amount of disturbances in the flow is reduced, implying then in a reduction of the final level of $\langle k \rangle^i$, according to G^i for both High and Low Reynolds number models.

Table 3.3 Cases and parameters used for turbulent flow (Sect. 3.3, High Reynolds Turbulence Model, Launder and Spalding (1974) [10])

Cases investigated	Dimensional					Non-dimensional					
	u_D (m/s)	u_S (m/s)	u_{rel} (m/s)	D (m)	K (m^2)	Re_D	Re	u_S/u_D	Da	ϕ	y+
Effect of Re_D	4.250E01	2.125E01	2.125E01	8.00E-03	1.000E-06	1.00E04	1.938E05	5.0E-01	1.665E-04	0.6	1.119E01
	2.120E02	1.062E02	1.062E02			5.00E04	1.938E06				4.762E01
	4.250E02	2.125E02	2.125E02			1.00E05	3.875E06				9.104E01
	4.250E03	2.125E03	2.125E03			1.00E06	3.875E07				8.267E02
Effect of u_S/u_D	4.250E02	0.000E00	4.250E02	8.00E-03	1.000E-06	2.00E05	3.875E06	0.0E00	1.665E-04	0.6	1.840E02
		1.062E02	3.188E02			1.50E05		2.5E-01			1.351E02
		2.125E02	2.125E02			1.00E05		5.0E-01			9.105E01
		3.187E02	1.063E02			5.00E04		7.5E-01			6.234E01
		4.037E02	2.125E01			1.00E04		9.5E-01			6.137E01
Effect of Da	4.250E02	2.125E02	2.125E02	1.00E-03	1.562E-08	1.25E04	3.875E06	5.0E-01	2.601E-06	0.6	1.170E02
				3.00E-03	1.406E-07	3.75E04			2.341E-05		1.081E02
				1.00E-02	1.562E-06	1.25E05			2.601E-04		8.690E01
Effect of ϕ	2.120E02	1.062E02	1.062E02	8.00E-03	1.975E-07	5.00E04	1.938E06	5.0E-01	3.289E-05	0.4	5.867E01
				3.50E-03	1.000E-06				1.665E-04	0.6	4.762E01
				1.30E-03	7.111E-06				1.184E-03	0.8	3.600E01

Table 3.4 Cases and parameters used (Sect. 3.3, Low Reynolds Turbulence Model, Abe et al. (1992) [11])

Cases investigated	Dimensional					Non-dimensional					
	u_D (m/s)	u_S (m/s)	u_{rel} (m/s)	D (m)	K (m^2)	Re_D	Re	u_s/u_D	Da	ϕ	y+
Effect of Re_D	5.312E00	2.656E00	2.656E00	8.00E-03	1.000E-06	1.25E03	4.844E04	5.0E-01	1.665E-04	0.6	1.72E00
	1.062E01	5.312E00	5.312E00			2.50E03	9.688E04				2.88E00
	2.125E01	1.062E01	1.062E01			5.00E03	1.938E05				4.68E00
Effect of u_S/u_D	1.190E01	0.000E00	1.190E01	8.00E-03	1.000E-06	5.60E03	1.085E05	0.0E00	1.665E-04	0.6	1.86E00
		2.975E00	8.925E00			4.20E03		2.5E-01			1.80E00
		5.950E00	5.950E00			2.80E03		5.0E-01			1.72E00
		8.925E00	2.975E00			1.40E03		7.5E-01			1.58E00
Effect of Da	3.400E01	1.700E01	1.700E01	1.00E-03	1.562E-08	1.00E03	3.100E05	5.0E-01	2.601E-06	0.6	3.25E00
				3.00E-03	1.406E-07	3.00E03			2.341E-05		3.65E00
				1.00E-02	1.562E-06	1.00E04			2.601E-04		4.78E00
Effect of ϕ	1.062E01	5.312E00	5.312E00	8.00E-03	1.975E-07	2.50E03	9.688E04	5.0E-01	3.289E-05	0.4	3.19E00
				3.50E-03	1.000E-06				1.665E-04	0.6	3.18E00
				1.30E-03	7.111E-06				1.184E-03	0.8	3.20E00

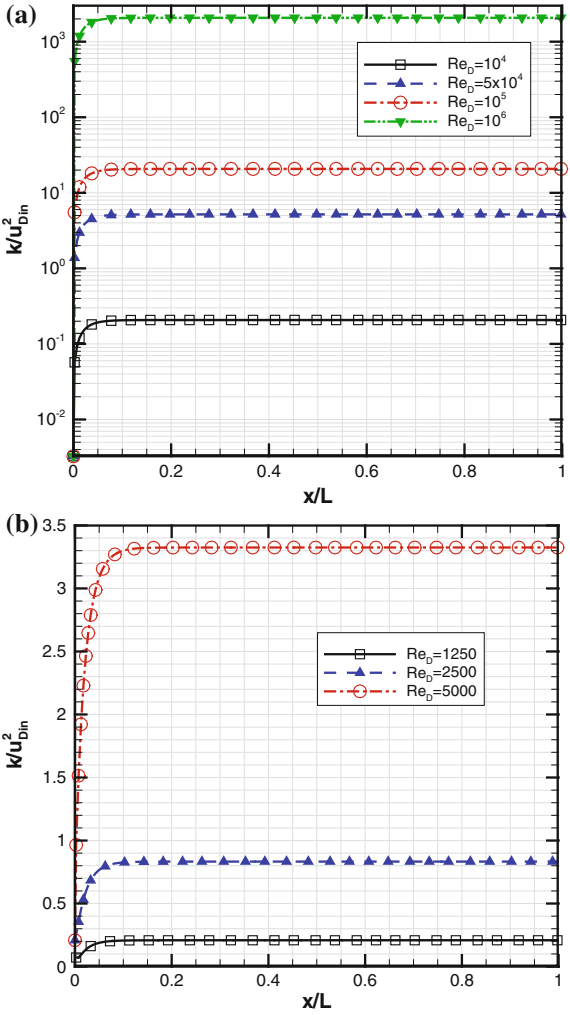

Fig. 3.5 Non-dimensional turbulent kinetic energy as a function of Re_D, with $u_s/u_D = 0.5$, $\phi = 0.6$: **a** High Reynolds model and **b** low Reynolds model

3.6.3 Effect of Darcy Number, Da

Figure 3.7 shows the distribution of turbulence kinetic energy with variation of Darcy number. It is notice that as Darcy number increases, the intensity of the turbulence kinetic energy inside of the porous layer decreases, mainly next to the entrance, staying constant along the channel after x/L = 0.15 for High (Fig. 3.7a) and Low Reynolds (Fig. 3.7b) models.

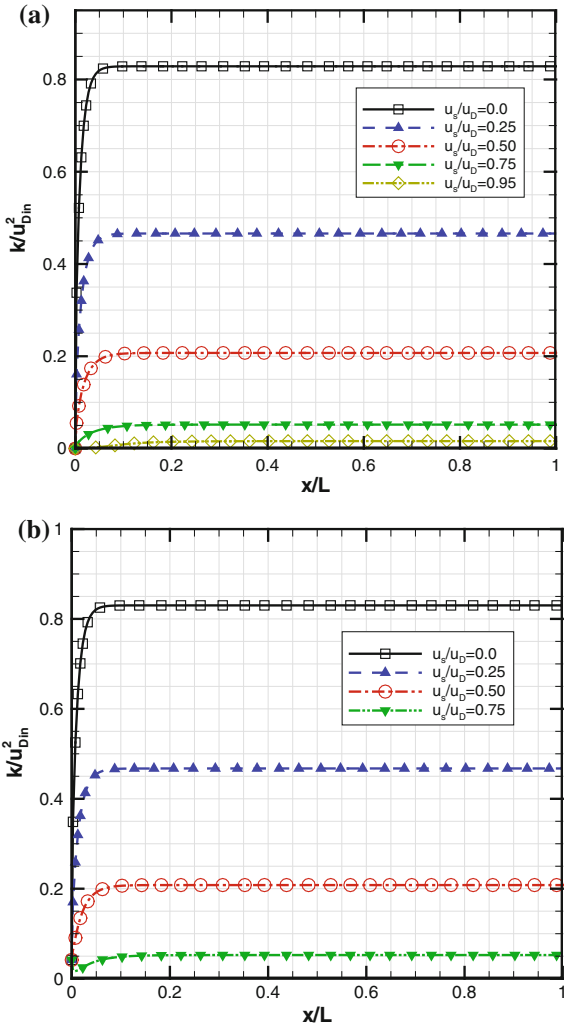

Fig. 3.6 Non-dimensional turbulent kinetic energy as a function of u_s/u_D, with $k_s/k_f = 25$, $\phi = 0.6$, $Da = 1.665 \times 10^{-4}$: **a** High Reynolds model $\mathrm{Re}_D \approx 10^5$, **b** low Reynolds model $\mathrm{Re}_D \approx 10^3$

3.6.4 *Effect of Porosity, ϕ*

Figure 3.8 shows values for non-dimensional turbulent kinetic energy along the channel as a function of porosity ϕ and for both turbulence models here employed. The Reynolds number, Re_D, and the velocity ratio between the solid and fluid phases, $u_s/u_D = 0.5$, are kept constant for all curves in the figure.

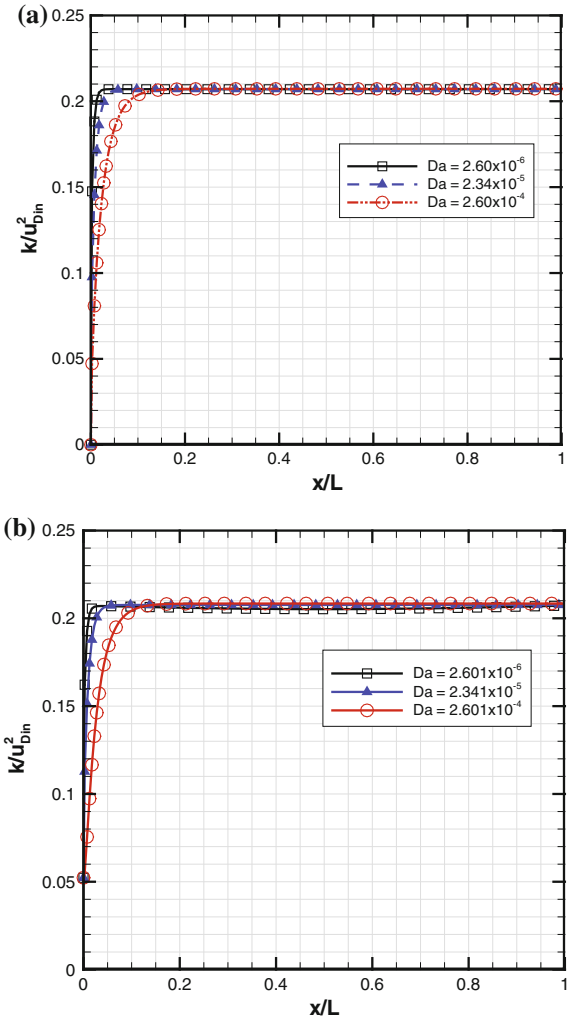

Fig. 3.7 Non-dimensional turbulent kinetic energy as a function of Da, with $u_s/u_D = 0.5$, $\phi = 0.6$: **a** High Reynolds model, Re $= 3.875 \times 10^6$; **b** low Reynolds model, Re $= 3.1 \times 10^5$

For a fixed Reynolds number based on $\bar{\mathbf{u}}_D = \phi\langle\bar{\mathbf{u}}\rangle^i$, a decrease in porosity corresponds to an increase in the intrinsic fluid velocity $\langle\bar{\mathbf{u}}\rangle^i$, reflecting a greater conversion of mean mechanical kinetic energy into turbulence. It is also observed that as the porosity gets lower, while keeping both velocities constant, the permeability K decreases leading to an increase in the final level of $\langle k\rangle^i$ according to G^i (see Eq. (3.22)), which is, as seen, the generation rate of $\langle k\rangle^i$ due the porous substrate.

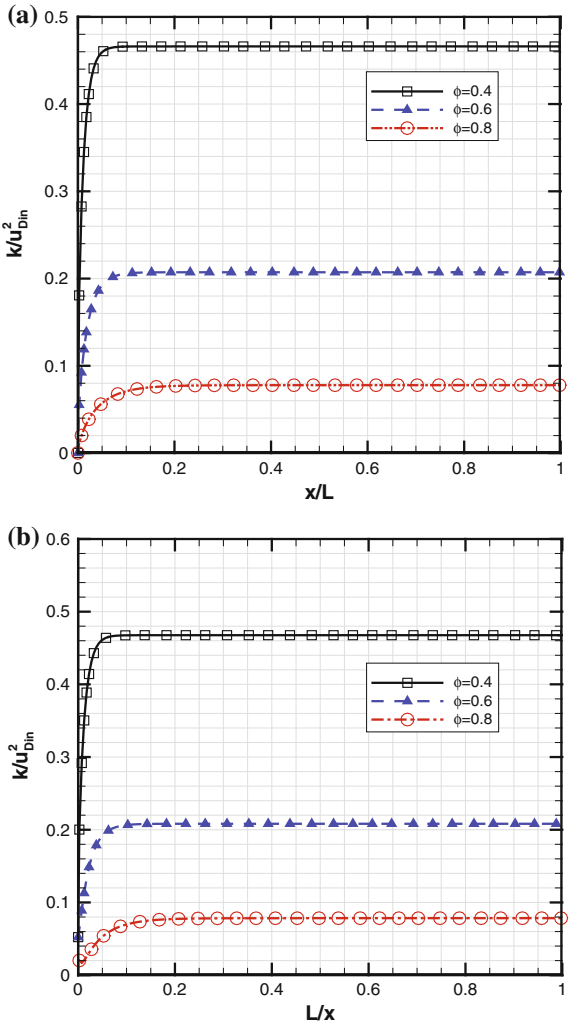

Fig. 3.8 Non-dimensional turbulent kinetic energy as a function of ϕ, with $u_s/u_D = 0.5$: **a** High Reynolds model, $\mathrm{Re_D} = 5 \times 10^4$; **b** low Reynolds model $\mathrm{Re_D} = 2.5 \times 10^3$

3.7 Chapter Summary

For laminar flows, this chapter investigated the behavior of a two-energy equation model to simulate flow and heat transfer in a moving porous bed. Numerical solutions for laminar flow in a moving porous bed were obtained for different Reynolds number Re_D, slip ratio $\mathbf{u}_s/\mathbf{u}_D$, Darcy number Da, porosity ϕ, ratio of thermal capacity $(\rho c_p)_s/(\rho c_p)_f$ and of ratio of thermal conductivity k_s/k_f, ranging

the slip ratio $\mathbf{u}_s/\mathbf{u}_D$. Governing equations were discretized and numerically solved. The following conclusions were observed:

(1) For low values of Re_D, $\mathbf{u}_s/\mathbf{u}_D$, Da, ϕ, $(\rho c_p)_s/(\rho c_p)_f$ and k_s/k_f, thermal equilibrium between phases require smaller axial lengths,
(2) Increasing the speed of the solid relative to a fixed fluid speed enhances the solid convection strength through the reactor as well as reduces the transport of energy between the phases, leading, ultimately, to an increase in the axial length necessary for thermal equilibrium to occur. The results presented here have a wide application to analysis and optimization of engineering processes in which a moving bed configuration could be identified.

Further, for turbulent flows, the behavior of turbulent kinetic energy in a concurrent moving porous bed was also presented. Numerical solutions for turbulent flow were obtained for different Reynolds number, Re_D, slip ratio, $\mathbf{u}_s/\mathbf{u}_D$, Darcy number, Da and porosity ϕ. Governing equations were discretized and numerically solved.

It is observed, according with the results obtained, that for high values of Re_D, higher final levels of $\langle k \rangle^i$ are simulated, as expected. The same effect occur for lower values of slip ratio $\mathbf{u}_s/\bar{\mathbf{u}}_D$, Darcy number Da and porosity ϕ, or say, for smaller values of these parameters, higher levels of $\langle k \rangle^i$ are computed. Results herein might be useful to the design and analysis of a number of engineering processes of practical interest.

References

1. Pivem AC, de Lemos MJS (2013) Turbulence modeling in a parallel flow moving porous bed. Int Commun Heat Mass Transf 48:1–7
2. Gray WG, Lee PCY (1977) On the theorems for local volume averaging of multiphase system. Int J Multiph Flow 3:333–340
3. Whitaker S (1969) Advances in theory of fluid motion in porous media. Ind Eng Chem 61:14–28
4. Whitaker S (1967) Diffusion and dispersion in porous media. J Amer Inst Chem Eng 13 (3):420–427
5. de Lemos MJS, Saito MB (2008) Computation of turbulent heat transfer in a moving porous bed using a macroscopic two-energy equation model. Int Commun Heat Mass Transf 35:1262–1266
6. Rocamora FD Jr, de Lemos MJS (2000) Analysis of Convective heat transfer of turbulent flow in satured porous media. Int Comm Heat Mass Transf 27(6):825–834
7. Wakao N, Kaguei S, Funazkri T (1979) Effect of fluid dispersion coefficients on particle-fluid heat transfer coefficient in packed bed. Chem Eng Sci 34:325–336
8. Kuwahara F, Shirota M, Nakayama A (2001) A numerical study of interfacial convective heat transfer coefficient in two-energy equation model for convection in porous media. Int J Heat Mass Transf 44:1153–1159

9. Saito MB, de Lemos MJS (2005) Interfacial heat transfer coefficient for non-equilibrium convective transport in porous media. Int Comm Heat Mass Transf 32(5):666–676
10. Launder BE, Sapalding DB (1974) The numerical computation of turbulent flows. Comp Meth Appl Mech Eng 3:269–289
11. Abe K, Nagano Y, Kondoh T (1992) An improve $k - \varepsilon$ model for prediction of turbulent flows with separation and reattachment. Trans JSME 58:3003–3010

Chapter 4
Combustion Systems

4.1 Introduction

Modeling of flows in inert porous media has attracted the attention of scientists and engineers worldwide and in the last decade a number of outstanding books, handbooks and edited books have been written on the subject [1–5].

In addition to thermo-mechanical models, including new research work aimed at biological applications [6] flows with chemical reactions in inert porous media have been also investigated extensively due to their many engineering applications and the demand for high efficiency power-producing devices. The growing use of efficient radiant burners can be encountered in the power and process industries and, as such, proper mathematical models of flow, heat, and mass transfer in porous media under combustion can benefit from the development of such engineering equipment.

In this chapter, an overview of recent development in modeling and simulating reactive flow in porous material will be presented.

4.2 Porous Burners

The advantages of having a combustion process inside an inert porous matrix are today well documented in the literature [7–14] including recent reviews about combustion of gases [15] and liquids [16] in such burners. Hsu et al. [17] points out some of its benefits, including higher burning speed and volumetric energy release rates, greater combustion stability and the ability to burn gases with low energy content. Driven by this motivation, the effects on porous ceramic inserts have been investigated in Peard et al. [18], among others.

Turbulence modeling of combustion within inert porous media has been conducted by Lim and Matthews [19] on the basis of an extension of the standard

M.J.S. de Lemos, *Thermal Non-Equilibrium in Heterogeneous Media*,
SpringerBriefs in Computational Mechanics,
DOI 10.1007/978-3-319-14666-9_4

k-ε model of Jones and Launder [20]. Work on direct simulation of turbulence in premixed flames, in cases when the porous dimension is of the order of the flame thickness, also has been reported in Sahraoui and Kaviany [21].

Further, nonreactive turbulent flow in porous media has been the subject of several studies [22–24], including many applications such as flow though porous baffles [25], channels with porous inserts [26] and buoyant flows [27]. In such work, intra-pore turbulence is accounted for in all transport equations, but only nonreactive flows have been investigated. Other important contributions in modeling inert flows in porous media can be found in the high-impact and outstanding competing model of turbulence developed by Kuznetsov et al. [28] and Kuznetsov [29].

Motivated by the foregoing, this chapter extends previous work on turbulence modeling in porous media to include now predictions of combusting flows. Computations are carried out for inert porous material considering one- and two-dimensional turbulent flows with one- and two-temperature approaches. In addition, four different thermo-mechanical models are compared here, namely Laminar Flow, Laminar Flow with Radiation Transport, Turbulent Flow and Turbulent Flow with Radiation Transport. As such, this contribution compares the effects of radiation and turbulence in smoothing temperature distributions within porous burners. The material in this chapter reviews the work in de Lemos [30, 31] and Coutinho and de Lemos [32] in a consolidated fashion, in addition to presenting additional information in regard to this topic.

4.3 Macroscopic Flow

The thermo-mechanical model employed here is based on the "double-decomposition" concept detailed in de Lemos [33] and Saito and de Lemos [34, 35]. Transport equations are volume-averaged according to the Volume Averaging Theorem [36–38] in addition of using time decomposition of flow variables followed by standard time-averaging procedure for treating turbulence. As the entire equation set is already fully available in the open literature, these equations will be reproduced here, and details about their derivations can be obtained in the aforementioned references. Essentially, in all the above mentioned studies, the flow variables are decomposed in a volume mean and a deviation (classical porous media analysis) in addition to being decomposed in a time mean and a fluctuation (classical turbulent flow treatment).

4.3.1 Macroscopic Continuity Equation

As previously stated, most of the equations to be shown in this chapter are fully detailed in existing open literature, so only their final modeled forms will be repeated.

The continuity of fluid mass reads.

$$\nabla \cdot \rho_f \bar{\mathbf{u}}_D = 0 \tag{4.1}$$

Equation (4.1) represents the macroscopic continuity equation for the flowing gas and its density, ρ_f, is allowed to vary as temperate rises.

4.3.2 Macroscopic Momentum Equation

The momentum equation for macroscopic turbulent flow reads as follows [33]:

$$\begin{aligned}\nabla \cdot \left(\rho_f \frac{\bar{\mathbf{u}}_D \bar{\mathbf{u}}_D}{\phi}\right) = &- \nabla\left(\phi \langle \bar{p} \rangle^i\right) + \mu \nabla^2 \bar{\mathbf{u}}_D + \nabla \cdot \left(-\rho_f \phi \langle \overline{\mathbf{u}' \mathbf{u}'} \rangle^i\right) \\ &- \left[\frac{\mu \phi}{K} \bar{\mathbf{u}}_D + \frac{c_F \phi \rho_f |\bar{\mathbf{u}}_D| \bar{\mathbf{u}}_D}{\sqrt{K}}\right]\end{aligned} \tag{4.2}$$

where the last two terms in Eq. (4.2) represent the Darcy and Forchheimer contributions, respectively. The symbol K is the porous medium permeability, $c_F = 0.55$ is the form drag coefficient, $\langle p \rangle^i$ is the intrinsic (fluid phase averaged) pressure, μ is the fluid viscosity and ϕ is the porosity of the porous medium.

4.3.3 Turbulence Modeling

Turbulence is handled via a macroscopic $k - \varepsilon$ model, given by:

$$\begin{aligned}\nabla \cdot \left(\rho_f \bar{\mathbf{u}}_D \langle k \rangle^i\right) = &\nabla \cdot \left[\left(\mu + \frac{\mu_{t_\phi}}{\sigma_k}\right) \nabla\left(\phi \langle k \rangle^i\right)\right] - \rho_f \langle \overline{\mathbf{u}' \mathbf{u}'} \rangle^i \\ &: \nabla \bar{\mathbf{u}}_D + c_k \rho_f \frac{\phi \langle k \rangle^i |\bar{\mathbf{u}}_D|}{\sqrt{K}} - \rho_f \phi \langle \varepsilon \rangle^i\end{aligned} \tag{4.3}$$

$$\begin{aligned}\nabla \cdot \left(\rho_f \bar{\mathbf{u}}_D \langle \varepsilon \rangle^i\right) = &\nabla \cdot \left[\left(\mu + \frac{\mu_{t_\varphi}}{\sigma_\varepsilon}\right) \nabla\left(\phi \langle \varepsilon \rangle^i\right)\right] + c_1 \left(-\rho \langle \overline{\mathbf{u}' \mathbf{u}'} \rangle^i : \nabla \bar{\mathbf{u}}_D\right) \frac{\langle \varepsilon \rangle^i}{\langle k \rangle^i} \\ &+ c_2 c_k \rho_f \frac{\phi \langle \varepsilon \rangle^i |\bar{\mathbf{u}}_D|}{\sqrt{K}} - c_2 \rho \phi \frac{\langle \varepsilon \rangle^{i^2}}{\langle k \rangle^i}\end{aligned} \tag{4.4}$$

Assuming that a model for the Macroscopic Reynolds Stresses $-\rho_f \phi \langle \overline{\mathbf{u}' \mathbf{u}'} \rangle^i$ can be given by

$$-\rho_f \phi \langle \overline{\mathbf{u}'\mathbf{u}'} \rangle^i = \mu_{t_\phi} 2 \langle \bar{\mathbf{D}} \rangle^{\mathbf{v}} - \frac{2}{3} \phi \rho_f \langle k \rangle^i \mathbf{I} \tag{4.5}$$

with

$$\langle \bar{\mathbf{D}} \rangle^v = \frac{1}{2} \left[\nabla \left(\phi \langle \bar{\mathbf{u}} \rangle^i \right) + \left[\nabla \left(\phi \langle \bar{\mathbf{u}} \rangle^i \right) \right]^T \right], \tag{4.6}$$

the momentum Eq. (4.2) finally reads [33],

$$\begin{aligned} \nabla \cdot \left(\rho_f \frac{\bar{\mathbf{u}}_D \bar{\mathbf{u}}_D}{\phi} \right) - \nabla \cdot \left\{ \left(\mu + \mu_{t_\phi} \right) \left[\nabla \bar{\mathbf{u}}_D + (\nabla \bar{\mathbf{u}}_D)^T \right] \right\} \\ = -\nabla \left(\phi \langle \bar{p} \rangle^i \right) - \left[\frac{\mu \phi}{K} \bar{\mathbf{u}}_D + \frac{c_F \phi \, \rho_f |\bar{\mathbf{u}}_D| \bar{\mathbf{u}}_D}{\sqrt{K}} \right] \end{aligned} \tag{4.7}$$

where,

$$\mu_{t_\phi} = \rho_f \, c_\mu \frac{\langle k \rangle^{i^2}}{\langle \varepsilon \rangle^i} \tag{4.8}$$

Note that in Eq. (4.7) a modified pressure is used, which includes the last term in Eq. (4.5). Dealing with combustion processes, it is important to emphasize that the fluid density ρ_f is allowed to vary within the computational domain, as mentioned above.

4.4 Heat Transfer

There are two possibilities to handle energy transport across the porous burner. In the simplified model, also named "One-Temperature Model", we assume the so-called local thermal equilibrium hypothesis (LTE), in which the solid temperature is numerically equal to that of the flowing gas. When the solid and the gas temperatures differ by a considerable amount, the "Two-Temperature Model" based on the local non-thermal equilibrium hypothesis (LTNE) applies. In the latter case, distinct energy balances are set for each phase. Transport equations for both models are discussed in the following sections.

4.4.1 Local Thermal Non-equilibrium Model (LTNE)

In cases where average temperatures in distinct phases are substantially different, macroscopic energy equations are obtained for both the fluid and solid phases by

also applying time- and volume-average operators to the instantaneous local equations [35]. As in the flow case, volume integration is performed over a Representative Elementary Volume or REV. After including the heat released due to the combustion reaction, one gets the following:

$$\text{Gas Phase}: \nabla \cdot (\rho_f \, c_{pf} \, \bar{\mathbf{u}}_D \langle \overline{T_f} \rangle^i) = \nabla \cdot \left\{ \mathbf{K}_{eff,f} \cdot \nabla \langle \overline{T_f} \rangle^i \right\} + h_i a_i \left(\langle \overline{T_p} \rangle^i - \langle \overline{T_f} \rangle^i \right) + \phi \, \Delta H \, S_{fu}, \tag{4.9}$$

$$\text{Solid Phase}: 0 = \nabla \cdot \left\{ \mathbf{K}_{eff,p} \cdot \nabla \langle \overline{T_p} \rangle^i \right\} - h_i a_i \left(\langle \overline{T_p} \rangle^i - \langle \overline{T_f} \rangle^i \right), \tag{4.10}$$

where $\langle \overline{T_f} \rangle^i$ and $\langle \overline{T_p} \rangle^i$ are the gas and solid temperatures, respectively, $a_i = A_i / \Delta V$ is the interfacial area per unit volume, h_i is the film coefficient for interfacial transport, ΔH is the heat of combustion [J/kg] and S_{fu} is the rate of fuel consumption [kg/m^{2}s; discussed later in this chapter]. Tensors $\mathbf{K}_{eff,f}$ and $\mathbf{K}_{eff,p}$ are the effective conductivity tensors for the fluid and solid phases, respectively, given by,

$$\mathbf{K}_{eff,f} = \left\{ \overbrace{\phi \, \lambda_f}^{conduction} \right\} \mathbf{I} + \underbrace{\mathbf{K}_{f,p}}_{local\ conduction} + \underbrace{\mathbf{K}_{disp}}_{dispersion} + \underbrace{\mathbf{K}_t + \mathbf{K}_{disp,t}}_{turbulence} \tag{4.11}$$

$$\mathbf{K}_{eff,s} = \left\{ \overbrace{(1-\phi) \, [\lambda_p}^{conduction} + \frac{\overbrace{16\sigma (\langle \overline{T_p} \rangle^i)^3}^{radiation}}{3\beta_r}] \right\} \mathbf{I} + \underbrace{\mathbf{K}_{p,f}}_{local\ conduction} \tag{4.12}$$

where λ is the thermal conductivity for either phase, β_r is the extinction coefficient [1/m], σ is the Stephan-Boltzmann constant and **I** is the unit tensor. All mechanisms contributing to heat transfer within the medium, together with turbulence and radiation, are included here to compare their effect on temperature distribution. Further, such distinct contributions of various mechanisms are the outcome of the application of gradient type diffusion models, in the following forms (see [35] for more details):

$$\text{Turbulent heat flux}: - \left(\rho \, c_p \right)_f \left(\phi \ \overline{\langle \mathbf{u}' \rangle^i \langle T_f' \rangle^i} \right) = \mathbf{K}_t \cdot \nabla \langle \bar{T}_f \rangle^i. \tag{4.13}$$

$$\text{Thermal dispersion}: - \left(\rho \, c_p \right)_f \left(\phi \ \langle {}^i\bar{\mathbf{u}}^i \overline{T_f} \rangle^i \right) = \mathbf{K}_{disp} \cdot \nabla \langle \bar{T}_f \rangle^i. \tag{4.14}$$

$$\text{Turbulent thermal dispersion}: - \left(\rho \, c_p \right)_f \left(\phi \ \langle \overline{{}^i\mathbf{u}' \, {}^i T_f'} \rangle^i \right) = \mathbf{K}_{disp,t} \cdot \nabla \langle \bar{T}_f \rangle^i. \tag{4.15}$$

$$\text{Local conduction:} \begin{cases} \dfrac{1}{\Delta V}\displaystyle\int_{A_i} \mathbf{n}_i\, k_f \overline{T_f}\, dA = \mathbf{K}_{f,p} \cdot \nabla \langle \bar{T}_f \rangle^i \\ -\dfrac{1}{\Delta V}\displaystyle\int_{A_i} \mathbf{n}_i\, k_p \overline{T_p}\, dA = \mathbf{K}_{p,f} \cdot \nabla \langle \bar{T}_p \rangle^i \end{cases} \tag{4.16}$$

In Eqs. (4.9) and (4.10) the heat transferred between the two phases was modeled by means of a interfacial convective heat transfer coefficient h_i, as presented above. A numerical correlation for it was proposed by Kuwahara et al. [39] for laminar flow as,

$$\frac{h_i D}{\lambda_f} = \left(1 + \frac{4(1-\phi)}{\phi}\right) + \frac{1}{2}(1-\phi)^{1/2} \mathrm{Re}_D\, \mathrm{Pr}^{1/3} \text{ valid for } 0.2 < \phi < 0.9 \tag{4.17}$$

For turbulent flow, the following expression was proposed in Saito and de Lemos [35],

$$\frac{h_i D}{\lambda_f} = 0.08 \left(\frac{Re_D}{\phi}\right)^{0.8} Pr^{1/3};\ \text{for } 1.0\,\text{x}\,10^4 < \frac{Re_D}{\phi} < 2.0\,\text{x}\,10^7,\ \text{valid for } 0.2 < \phi < 0.9, \tag{4.18}$$

4.5 Combustion Modeling

In this work, the gas phase is assumed to be composed by a premixture of air and gaseous fuel that undergoes combustion while flowing through the solid. For analyzing such a system, the equation set (4.1) to (2.57) is complemented with a transport equation for the fuel and a kinetics model for the burning process [30].

4.5.1 Mass Transport for Fuel

Transport equation for the fuel is,

$$\nabla \cdot (\rho_f \bar{\mathbf{u}}_D \langle \bar{m}_{fu} \rangle^i) = \nabla \cdot \rho_f \mathbf{D}_{eff} \cdot \nabla (\phi \langle \bar{m}_{fu} \rangle^i) - \phi\, S_{fu} \tag{4.19}$$

where $\langle \bar{m}_{fu} \rangle^i$ is the mass fraction for the fuel. The effective mass transport tensor, $\mathbf{D}_{eff}$, is defined as:

$$\mathbf{D}_{eff} = \underbrace{\mathbf{D}_{disp}}_{dispersion} + \overbrace{\mathbf{D}_{diff}}^{diffusion} + \underbrace{\mathbf{D}_t + \mathbf{D}_{disp,t}}_{turbulence} = \mathbf{D}_{disp} + \frac{1}{\rho_f}\left(\frac{\mu_\phi}{Sc_\ell} + \frac{\mu_{t_\phi}}{Sc_{\ell,t}}\right)\mathbf{I}$$
$$= \mathbf{D}_{disp} + \frac{1}{\rho_f}\left(\frac{\mu_{\phi,eff}}{Sc_{\ell,eff}}\right)\mathbf{I} \tag{4.20}$$

where Sc_ℓ and $Sc_{\ell,t}$ are the laminar and turbulent Schmidt numbers for species ℓ, respectively, and "*eff*" denotes an effective value. The dispersion tensor is defined such that,

$$-\rho_f \phi \left\langle {}^i\bar{\mathbf{u}}\, {}^i\bar{m}_{fu} \right\rangle^i = \rho_f\, \mathbf{D}_{disp} \cdot \nabla(\phi \left\langle \bar{m}_{fu} \right\rangle^i) \tag{4.21}$$

4.5.2 Chemical Reaction

The chemical exothermic reaction is assumed to be instantaneous and to occur in a single, kinetic-controlled step, which, for combustion of a mixture of air and methane, is given by the following chemical reaction [8, 40];

$$CH_4 + 2(1+\Psi)(O_2 + 3.76N_2) \rightarrow CO_2 + 2H_2O + 2\Psi O_2 + 7.52(1+\Psi)N_2 \tag{4.22}$$

For *N*-heptane, a similar equation reads as follows [41],

$$C_7H_{16} + 11(1+\Psi)(O_2 + 3.76N_2) \rightarrow 7CO_2 + 8H_2O + 11\Psi O_2 + 41.36(1+\Psi)N_2 \tag{4.23}$$

And for Octane, we get,

$$C_8H_{18} + 12.5(1+\Psi)(O_2 + 3.76N_2) \rightarrow 8CO_2 + 9H_2O + 12.5\Psi O_2 + 47(1+\Psi)N_2 \tag{4.24}$$

where Ψ is the excess air in the reactant stream at the inlet of the porous foam. For the stoichiometric ratio, $\Psi = 0$. In all of these equations, the reaction is then assumed to be kinetically controlled and occurring infinitely fast. A general expression for them can be derived as,

$$C_nH_{2m} + (n + \frac{m}{2})(1+\Psi)(O_2 + 3.76N_2) \rightarrow nCO_2 + mH_2O + (n + \frac{m}{2})\Psi O_2 + (n + \frac{m}{2})3.76(1+\Psi)N_2 \tag{4.25}$$

where the coefficients n and m can be found in Table 4.1. Here, Eq. (4.25) is assumed to hold for the particular examples given in Table 4.1.

The local instantaneous rate of fuel consumption over the total volume (fluid plus solid) was determined by one-step Arrhenius reaction [42, 43] given by,

$$S_{fu} = \rho_f^a A \left\langle m_{fu}^b \right\rangle^i \left\langle m_{ox}^c \right\rangle^i \; e^{-E/R\left\langle \bar{T}_f \right\rangle^i} \tag{4.26}$$

where m_{fu} and m_{ox} are the local instantaneous mass fractions for the fuel and oxidant, respectively, the coefficients *a, b, c* depend on the particular reaction [42], A is the pre-exponential factor and E is the activation energy, where numerical values for these parameters depend on the fuel considered [43]. For simplicity in presenting the ideas in this chapter, we assume here that $a = 2$, $b = c = 1$, which corresponds to the burning of a mixture of methane and air [8, 30, 40].

Density ρ_f in these equations is determined from the perfect gas equation for a mixture of perfect gases:

$$\rho_f = \frac{P_o}{RT_f \sum_1^{\ell} \frac{m_\ell}{M_\ell}} \tag{4.27}$$

where P_o is the absolute pressure, R is the universal gas constant [8.134 J/(mol.K)] and M_ℓ is the molecular weight of species ℓ.

4.6 Heat Release

4.6.1 Double-Decomposition of Variables

Macroscopic transport equations for turbulent flow in a porous medium are obtained through the simultaneous application of time and volume average operators over a generic fluid property φ. Such concepts are defined as follows [36–38].

$$\langle \varphi \rangle^i = \frac{1}{\Delta V_f} \int_{\Delta V_f} \varphi dV; \; \langle \varphi \rangle^v = \phi \langle \varphi \rangle^i; \; \phi = \frac{\Delta V_f}{\Delta V}, \text{ with } \varphi = \langle \varphi \rangle^i + {}^i\varphi \tag{4.28}$$

$$\bar{\varphi} = \frac{1}{\Delta t} \int_t^{t+\Delta t} \varphi \, dt, \text{ with } \varphi = \bar{\varphi} + \varphi' \tag{4.29}$$

where ΔV_f is the volume of the fluid contained in a REV ΔV, and intrinsic average and volume average are represented, respectively, by $\langle \; \rangle^i$ and $\langle \; \rangle^v$. Also, due to the definition of average we get,

Table 4.1 Coefficients in the general combustion Eq. (4.25)

Gas	n	m	(n + m/2)	(n + m/2) × 3.76
Methane	1	2	2	7.52
N-heptane	7	8	11	41.36
Octane	8	9	12.5	47

$$\overline{\varphi'} = 0 \tag{4.30}$$

and

$$\langle {}^{i}\varphi \rangle^{i} = 0 \tag{4.31}$$

The double decomposition idea, fully described in de Lemos [33], combines Eqs. (4.28) and (4.29) and can be summarized as:

$$\overline{\langle \varphi \rangle^{i}} = \langle \bar{\varphi} \rangle^{i};\ {}^{i}\bar{\varphi} = \overline{{}^{i}\varphi};\ \langle \varphi' \rangle^{i} = \langle \varphi \rangle^{i'} \tag{4.32}$$

and,

$$\left.\begin{aligned} \varphi' &= \langle \varphi' \rangle^{i} + {}^{i}\varphi' \\ {}^{i}\varphi &= \overline{{}^{i}\varphi} + {}^{i}\varphi' \end{aligned}\right\} \quad \text{where} \quad {}^{i}\varphi' = \varphi' - \langle \varphi' \rangle^{i} = {}^{i}\varphi - \overline{{}^{i}\varphi} \tag{4.33}$$

Therefore, the quantity φ can be expressed by either,

$$\varphi = \overline{\langle \varphi \rangle^{i}} + \langle \varphi \rangle^{i'} + \overline{{}^{i}\varphi} + {}^{i}\varphi' \tag{4.34}$$

or

$$\varphi = \langle \bar{\varphi} \rangle^{i} + {}^{i}\bar{\varphi} + \langle \varphi' \rangle^{i} + {}^{i}\varphi'. \tag{4.35}$$

The term ${}^{i}\varphi'$ can be viewed as either *the temporal fluctuation of the spatial deviation* or the *spatial deviation of the temporal fluctuation* of the quantity φ.

4.6.2 Macroscopic Fuel Consumption

To derive macroscopic equations for the simple combustion model presented earlier, we can take Eq. (4.26) with $a = 2$, $b = c = 1$ and note that the rate of fuel consumption is dictated by the product of two local instantaneous values, m_{fu} and m_{ox}, which represent local instantaneous mass fractions for the fuel and oxygen, respectively. Now, if we apply to each one of them the decomposition (4.34), or its equivalent (4.35), we get,

$$m_{fu} = \langle \bar{m}_{fu} \rangle^i + {}^i\bar{m}_{fu} + \langle m'_{fu} \rangle^i + {}^i m'_{fu} \tag{4.36}$$

$$m_{ox} = \langle \bar{m}_{ox} \rangle^i + {}^i\bar{m}_{ox} + \langle m'_{ox} \rangle^i + {}^i m'_{ox} \tag{4.37}$$

For the sake of simplicity and manipulation, looking at only the product of the mass fractions ($m_{fu} m_{ox}$) in Eq. (4.26) and applying the decompositions Eqs. (4.36) and (4.37), we get,

$$\begin{aligned} m_{fu}\, m_{ox} = {} & \langle \bar{m}_{fu} \rangle^i \langle \bar{m}_{ox} \rangle^i + {}^i\bar{m}_{fu} \langle \bar{m}_{ox} \rangle^i + \left\langle m'_{fu} \right\rangle^i \langle \bar{m}_{ox} \rangle^i + {}^i m'_{fu} \langle \bar{m}_{ox} \rangle^i \\ & + \langle \bar{m}_{fu} \rangle^i {}^i\bar{m}_{ox} + {}^i\bar{m}_{fu}\, {}^i\bar{m}_{ox} + \left\langle m'_{fu} \right\rangle^i {}^i\bar{m}_{ox} + {}^i m'_{fu}\, {}^i\bar{m}_{ox} \\ & + \langle \bar{m}_{fu} \rangle^i \langle m'_{ox} \rangle^i + {}^i\bar{m}_{fu} \langle m'_{ox} \rangle^i + \left\langle m'_{fu} \right\rangle^i \langle m'_{ox} \rangle^i + {}^i m'_{fu} \langle m'_{ox} \rangle^i \\ & + \langle \bar{m}_{fu} \rangle^i {}^i m'_{ox} + {}^i\bar{m}_{fu}\, {}^i m'_{ox} + \left\langle m'_{fu} \right\rangle^i {}^i m'_{ox} + {}^i m'_{fu}\, {}^i m'_{ox} \end{aligned} \tag{4.38}$$

Applying the volume-average operator Eq. (4.28) to the instantaneous local product Eq. (4.38), we get,

$$\begin{aligned} \langle m_{fu}\, m_{ox} \rangle^i = {} & \left\langle \langle \bar{m}_{fu} \rangle^i \langle \bar{m}_{ox} \rangle^i \right\rangle^i + \left\langle {}^i\bar{m}_{fu} \langle \bar{m}_{ox} \rangle^i \right\rangle^i + \left\langle \left\langle m'_{fu} \right\rangle^i \langle \bar{m}_{ox} \rangle^i \right\rangle^i + \left\langle {}^i m'_{fu} \langle \bar{m}_{ox} \rangle^i \right\rangle^i \\ & + \left\langle \langle \bar{m}_{fu} \rangle^i {}^i\bar{m}_{ox} \right\rangle^i + \left\langle {}^i\bar{m}_{fu}\, {}^i\bar{m}_{ox} \right\rangle^i + \left\langle \left\langle m'_{fu} \right\rangle^i {}^i\bar{m}_{ox} \right\rangle^i + \left\langle {}^i m'_{fu}\, {}^i\bar{m}_{ox} \right\rangle^i \\ & + \left\langle \langle \bar{m}_{fu} \rangle^i \langle m'_{ox} \rangle^i \right\rangle^i + \left\langle {}^i\bar{m}_{fu} \langle m'_{ox} \rangle^i \right\rangle^i + \left\langle \left\langle m'_{fu} \right\rangle^i \langle m'_{ox} \rangle^i \right\rangle^i + \left\langle {}^i m'_{fu} \langle m'_{ox} \rangle^i \right\rangle^i \\ & + \left\langle \langle \bar{m}_{fu} \rangle^i {}^i m'_{ox} \right\rangle^i + \left\langle {}^i\bar{m}_{fu}\, {}^i m'_{ox} \right\rangle^i + \left\langle \left\langle m'_{fu} \right\rangle^i {}^i m'_{ox} \right\rangle^i + \left\langle {}^i m'_{fu}\, {}^i m'_{ox} \right\rangle^i \end{aligned} \tag{4.39}$$

Now, looking back at Eq. (4.31), all terms containing only one deviation factor in Eq. (4.39) will vanish, such that,

$$\begin{aligned} \langle m_{fu}\, m_{ox} \rangle^i = {} & \langle \langle \bar{m}_{fu} \rangle^i \langle \bar{m}_{ox} \rangle^i \rangle^i + \langle {}^i\bar{m}_{fu} \langle \bar{m}_{ox} \rangle^i \rangle^i + \langle \langle m'_{fu} \rangle^i \langle \bar{m}_{ox} \rangle^i \rangle^i + \langle {}^i m'_{fu} \langle \bar{m}_{ox} \rangle^i \rangle^i \\ & + \langle \langle \bar{m}_{fu} \rangle^i {}^i\bar{m}_{ox} \rangle^i + \langle {}^i\bar{m}_{fu}\, {}^i\bar{m}_{ox} \rangle^i + \langle \langle m'_{fu} \rangle^i {}^i\bar{m}_{ox} \rangle^i + \langle {}^i m'_{fu}\, {}^i\bar{m}_{ox} \rangle^i \\ & + \langle \langle \bar{m}_{fu} \rangle^i \langle m'_{ox} \rangle^i \rangle^i + \langle {}^i\bar{m}_{fu} \langle m'_{ox} \rangle^i \rangle^i + \langle \langle m'_{fu} \rangle^i \langle m'_{ox} \rangle^i \rangle^i + \langle {}^i m'_{fu} \langle m'_{ox} \rangle^i \rangle^i \\ & + \langle \langle \bar{m}_{fu} \rangle^i {}^i m'_{ox} \rangle^i + \langle {}^i\bar{m}_{fu}\, {}^i m'_{ox} \rangle^i + \langle \langle m'_{fu} \rangle^i {}^i m'_{ox} \rangle^i + \langle {}^i m'_{fu}\, {}^i m'_{ox} \rangle^i \end{aligned} \tag{4.40}$$

The following equation is left as,

$$\begin{aligned}\langle m_{fu}\, m_{ox}\rangle^i = {} & \langle \bar{m}_{fu}\rangle^i \langle \bar{m}_{ox}\rangle^i + \left\langle m'_{fu}\right\rangle^i \langle \bar{m}_{ox}\rangle^i + \langle {}^i\bar{m}_{fu}\ {}^i\bar{m}_{ox}\rangle^i + \left\langle {}^i m'_{fu}\ {}^i\bar{m}_{ox}\right\rangle^i \\ & + \langle \bar{m}_{fu}\rangle^i \langle m'_{ox}\rangle^i + \left\langle m'_{fu}\right\rangle^i \langle m'_{ox}\rangle^i + \langle {}^i\bar{m}_{fu}\ {}^i m'_{ox}\rangle^i + \left\langle {}^i m'_{fu}\ {}^i m'_{ox}\right\rangle^i \end{aligned} \tag{4.41}$$

Another way to write Eq. (4.41), using the equivalences shown in Eq. (4.32), is

$$\begin{aligned}\langle m_{fu}\, m_{ox}\rangle^i = {} & \overline{\langle m_{fu}\rangle^i}\ \overline{\langle m_{ox}\rangle^i} + \langle m_{fu}\rangle^{i'}\ \overline{\langle m_{ox}\rangle^i} + \langle \overline{{}^i m_{fu}}\ \overline{{}^i m_{ox}}\rangle^i + \langle {}^i m'_{fu}\ \overline{{}^i m_{ox}}\rangle^i \\ & + \overline{\langle m_{fu}\rangle^i}\ \langle m_{ox}\rangle^{i'} + \langle m_{fu}\rangle^{i'}\ \langle m_{ox}\rangle^{i'} + \langle \overline{{}^i m_{fu}}\ {}^i m'_{ox}\rangle^i + \langle {}^i m'_{fu}\ {}^i m'_{ox}\rangle^i \end{aligned} \tag{4.42}$$

If we now apply the time-averaging operator over Eq. (4.42) and note that, due to Eq. (4.30), all terms containing only one time fluctuation factor vanish, such that,

$$\begin{aligned}\overline{\langle m_{fu}\, m_{ox}\rangle^i} = {} & \overline{\overline{\langle m_{fu}\rangle^i}\ \overline{\langle m_{ox}\rangle^i}} + \overline{\langle m_{fu}\rangle^{i'}\ \overline{\langle m_{ox}\rangle^i}} + \overline{\langle \overline{{}^i m_{fu}}\ \overline{{}^i m_{ox}}\rangle^i} + \overline{\langle {}^i m'_{fu}\ \overline{{}^i m_{ox}}\rangle^i} \\ & + \overline{\overline{\langle m_{fu}\rangle^i}\ \langle m_{ox}\rangle^{i'}} + \overline{\langle m_{fu}\rangle^{i'}\ \langle m_{ox}\rangle^{i'}} + \overline{\langle \overline{{}^i m_{fu}}\ {}^i m'_{ox}\rangle^i} + \overline{\langle {}^i m'_{fu}\ {}^i m'_{ox}\rangle^i} \end{aligned} \tag{4.43}$$

we get the following time-and-volume averaged expression after dropping all null values,

$$\overline{\langle m_{fu} m_{ox}\rangle^i} = \overline{\langle m_{fu}\rangle^i}\ \overline{\langle m_{ox}\rangle^i} + \langle \overline{{}^i m_{fu}}\ \overline{{}^i m_{ox}}\rangle^i + \overline{\langle m_{fu}\rangle^{i'}\ \langle m_{ox}\rangle^{i'}} + \overline{\langle {}^i m'_{fu}\ {}^i m'_{ox}\rangle^i} \tag{4.44}$$

Again, we can make use of an alternative representation for the same terms in Eq. (4.44) when looking at equivalences (4.32). We then get,

$$\langle \overline{m_{fu}\, m_{ox}}\rangle^i = \langle \bar{m}_{fu}\rangle^i \langle \bar{m}_{ox}\rangle^i + \langle {}^i\bar{m}_{fu}\ {}^i\bar{m}_{ox}\rangle^i + \overline{\langle m'_{fu}\rangle^i \langle m'_{ox}\rangle^i} + \langle \overline{{}^i m'_{fu}\ {}^i m'_{ox}}\rangle^i \tag{4.45}$$

Including the full decomposition Eq. (4.45) back into the expression for S_{fu}, Eq. (4.26), we get,

$$\begin{aligned}\langle \overline{S_{fu}}\rangle^i &= \rho_f^2 A\, \langle \overline{m_{fu}\, m_{ox}}\rangle^i\ e^{-E/R\langle \bar{T}\rangle^i} \\ &= \rho_f^2 A \left(\underbrace{\langle \bar{m}_{fu}\rangle^i \langle \bar{m}_{ox}\rangle^i}_{I} + \underbrace{\langle {}^i\bar{m}_{fu}\ {}^i\bar{m}_{ox}\rangle^i}_{II} + \underbrace{\overline{\langle m'_{fu}\rangle^i \langle m'_{ox}\rangle^i}}_{III} + \underbrace{\langle \overline{{}^i m'_{fu}\ {}^i m'_{ox}}\rangle^i}_{IV} \right) e^{-E/R\langle \bar{T}\rangle^i} \end{aligned} \tag{4.46}$$

The four term on the rhs of Eq. (4.46), multiplied by the parameter $\rho_f^2 A\, e^{-E/R\langle \bar{T}\rangle^i}$, can be interpreted physically as follows:

I. **Reaction rate** due to volume-and-time averaged values of fuel and oxidant mass fractions. This is the standard rate of reaction commonly employed in the literature [8, 40, 41].
II. **Dispersive reaction rate** due to deviation of mean time-mean fuel and oxidant mass fractions. This rate occurs even is the flow in laminar and is due to fact that both mass fractions present a deviation value about their volume-averaged values.
III. **Turbulent reaction rate** due to time-fluctuation of volume-averaged values of fuel and oxidant mass flow rates, and represents additional fuel consumption rate because, inside a REV, the volume-averaged mass fraction of both oxygen and fuel fluctuate with time, giving rise to a non-null time correlation.
IV. **Turbulent dispersive reaction rate** due to simultaneous time fluctuations and volume deviations of both values of fuel and oxidant mass flow rates.

In light of Eq. (4.33), terms III and IV in Eq. (4.46), can be recombined to form,

$$\overline{\langle m'_{fu}\rangle^i \langle m'_{ox}\rangle^i} + \langle \overline{{}^i m'_{fu}\, {}^i m'_{ox}}\rangle^i = \langle \overline{m'_{fu}\, m'_{ox}}\rangle^i \tag{4.47}$$

giving,

$$S^t_{fu,\phi} = \rho_f^2 A \langle \overline{m'_{fu}\, m'_{ox}}\rangle^i \; e^{-E/R\langle \bar{T}\rangle^i} \tag{4.48}$$

which can be seen as the overall effect of turbulence on the fuel consumption rate. Likewise, the dispersive component reads,

$$S^{disp}_{fu,\phi} = \rho_f^2 A \langle {}^i\bar{m}_{fu}\, {}^i\bar{m}_{ox}\rangle^i \; e^{-E/R\langle \bar{T}\rangle^i} \tag{4.49}$$

and for the first term in Eq. (4.46),

$$S_{fu,\phi} = \rho_f^2 A \langle \bar{m}_{fu}\rangle^i \langle \bar{m}_{ox}\rangle^i \; e^{-E/R\langle \bar{T}\rangle^i} \tag{4.50}$$

finally giving,

$$\langle \overline{S_{fu}}\rangle^i = S_{fu,\phi} + S^{disp}_{fu,\phi} + S^t_{fu,\phi} \tag{4.51}$$

The models for Eqs. (4.48) and (4.49) and evaluation of their relative values when compared to Eq. (4.46) remains an open question and shall be the subject of further investigation. They might be related to physically controlled mechanisms associated with the full reaction rate Eq. (4.46).

4.7 Numerical Results

4.7.1 Simulation Details and Boundary Conditions

The two-temperature model given in Sect. 4.4.1 was applied. Figure 1.3e illustrates the case here analyzed with corresponding boundary conditions. The finite–volume technique was employed to discretize the transport equations and the resulting algebraic equation set was relaxed using the well-known segregated method SIMPLE [45]. Further, the flame front position was the sole outcome of the solution process and no artificial numerical set-up was implemented for holding the flame at some particular location.

For simulations using the geometry in Fig. 1.3e, the parameters and boundary conditions here used are those of the burner developed by Pereira [46]. Simulations assumed given temperatures (solid and gas) and fuel mass fraction at inlet ($x = 0\,\text{cm}$). At exit ($x = 8\,\text{cm}$), for the solid temperature, a balance between the energy conducted to the exit of the burner and the radiation leaving the porous material to the environment was applied. Further, an initial length of 2 cm was considered to be made of a material that prevents flash back of the flame, which is commonly referred to in the literature as "*flame trap*" [44]. Ignition, is existing, was then calculated for $x > 2\,\text{cm}$.

4.7.2 Grid Independence Study

The computational grid was generated with a concentration of points close to the beginning of the combustion section where steep temperature and species gradients were expected to appear. Two grids were employed with 120 and 240 nodes in the x direction, respectively. Figure 4.1 shows temperature profiles calculated with both mentioned grids and indicates that no detectable differences exists between the two sets of results. For this reason, all simulations in this work make use of the 120 node stretched grid.

4.7.3 One Dimensional Combustor

Figure 4.2 shows results for temperature of both the burning gas and solid porous matrix. Results can correctly predict the increase of the gas temperature when the excess ratio is reduced or the inlet mass flow rate is increased.

Figure 4.3a also shows the effect of excess air Ψ on the gas temperature, T_f, and solid temperature, T_p. Temperature levels for the stoichiometric case and for $\Psi = 0.8$ gave numerical values close to those from Kuo [42]. Likewise, mass fraction behavior of species CH_4, CO_2 (Fig. 4.3b) and H_2O, O_2 (Fig. 4.3c) follow closely

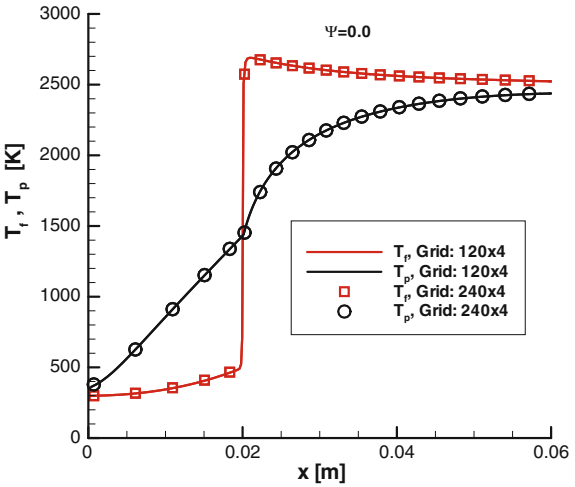

Fig. 4.1 Grid independence studies

those reported by Kuo [42], for the one-equation simple combustion model here presented. Excess air reduces the final mass fraction of CO_2 and water and raises the amount of oxygen not participating in the combustion reaction. These results are the outcome of the single step reaction (Sect. 4.5.2) that links the consumption and production rates of individual constituents of the mixture.

Figure 4.4 shows the dependence of temperature levels on inlet velocities U_{in}. As axial flow in increased, one can note a slight reduction of peak values of temperatures, followed by the movement of the flame towards the exit of the burner.

Although the movement of the flame front is in accordance with simulations by Trimis and Durst [44], here a reduction on the maximum values of temperatures was calculated here, which disagrees with that study's findings, where the temperature rises as the inlet mass flow rate is increased. One possible explanation for this contrary behavior is that there are a number of distinct parameters and assumptions in both calculations sets, here and in Trimis and Durst [44], spanning from mathematical to numerical modeling hypotheses, which might affect the final results.

Four different thermo-mechanical models are compared now: namely, Laminar, Laminar with Radiation Transport, Turbulent and Turbulent with Radiation Transport. The Radiation model is included by considering the radiation transport term in the T_p-Eq. (4.12). Turbulence modeling is handled by resolving the $k - \varepsilon$ model, Eqs. (4.3) and (4.4), in addition to solving for the macroscopic turbulent eddy viscosity μ_{t_ϕ}, Eq. (4.8). In all models, combustion is simulated via a unique simple closure, which is presented by Eqs. (4.22) and (4.26).

Numerical simulations obtained with different models are presented in Fig. 4.5 for two values of U_{in}. Figure 4.5a shows that for a low value of U_{in}, the flame (shown by solid lines) stabilizes close to the beginning of the burning section ($x = 2$ cm), independent of the mathematical model applied. Solid temperatures are

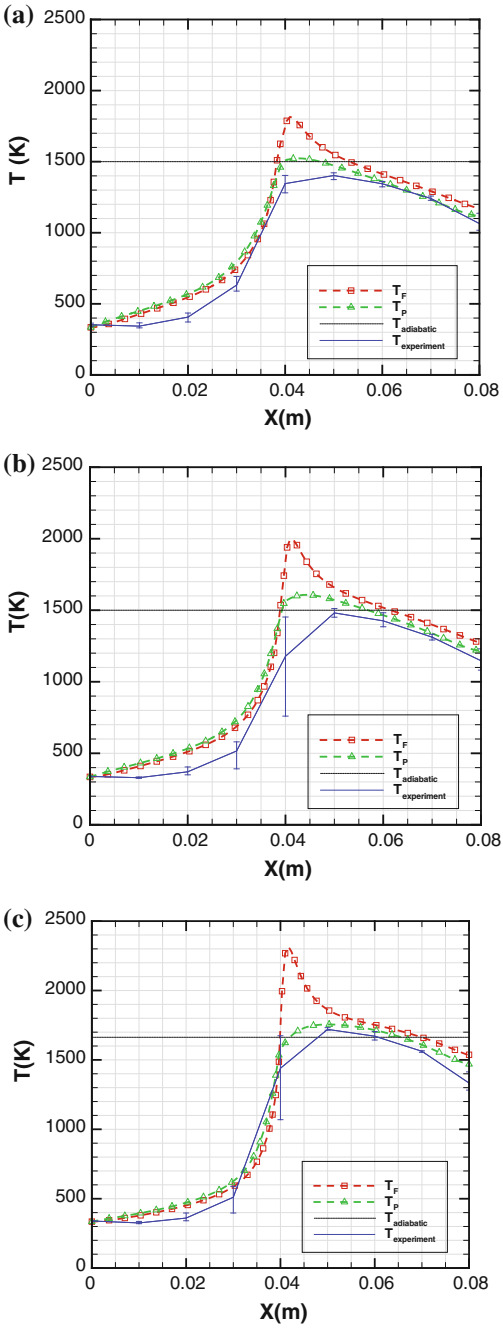

Fig. 4.2 Code validation, experiments by Pereira [46]: **a** Case 01 ($\psi = 1.0$, $U_{in} = 0.15$), **b** Case 02 ($\psi = 0.67$, $U_{in} = 0.21$), **c** Case 03 ($\psi = 0.67$, $U_{in} = 0.40$)

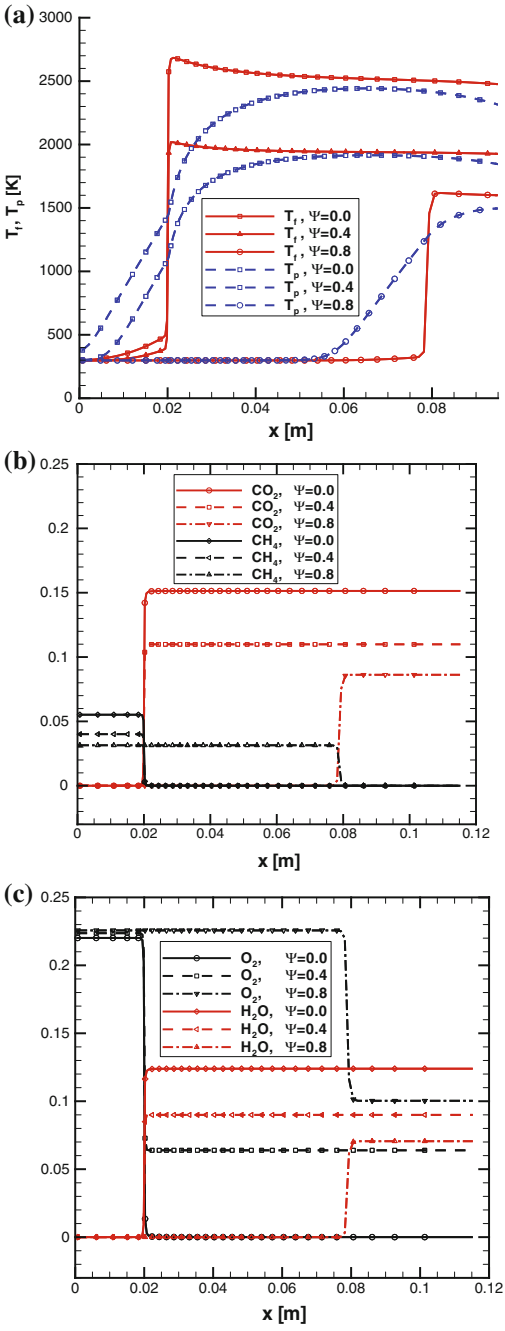

Fig. 4.3 Effect of excess air Ψ for U_{in} = 0.1 m/s and zero thermal radiation flux at exit, x = 12 cm: **a** Temperature fields. **b** Fuel and carbon dioxide. **c** Water and oxygen

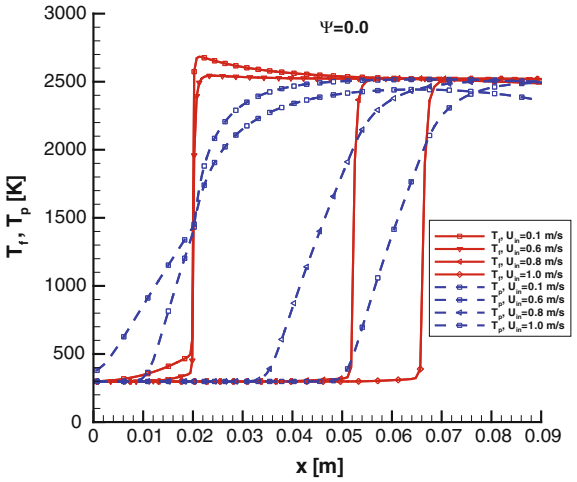

Fig. 4.4 Effect of inlet gas velocity on temperature fields

influenced by radiation transport, which tends to smooth out temperature differences within the solid matrix, enhancing, as such, the regenerative advantage of porous burners (shown by dashed lines). Regeneration is achieved by preheating the gas prior to the combustion zone. In fact, the use of a turbulence model in conjunction with radiation transport gives the higher temperature peak of the gas temperature at the flame position. Increasing the inlet mass flow rate (Fig. 4.5b), the flame is pushed towards the burners exit, regardless of the model used. Here also radiation transport substantially affects the solid temperature distribution, but definitive conclusions on the appropriateness of each model can be reached only after careful comparison to experimental measurements. This shall be the subject of future research efforts.

Further, four different thermo-mechanical models are now compared, namely Laminar, Laminar with Radiation Transport, Turbulent, Turbulent with Radiation Transport. Radiation model is included by considering the radiation transport term in the T_p-Eq. (4.12). Turbulence modeling is handled by resolving the $k - \varepsilon$ model (Eqs. 4.3–4.4) in addition to solving for the macroscopic turbulent eddy viscosity μ_{t_φ}, Eq. (4.8). In all models, combustion is simulated via a unique simple closure, which is presented by Eqs. (4.22) and (4.26).

4.8 Chapter Summary

This chapter presented one-dimensional simulations for a mixture of air and methane burning in a porous material. The LTNE models was applied and four different thermo-mechanical models were compared along with a unique simple closure for combustion. The Results indicate that a substantially different temperature distribution pattern is obtained depending on the model used. For high excess

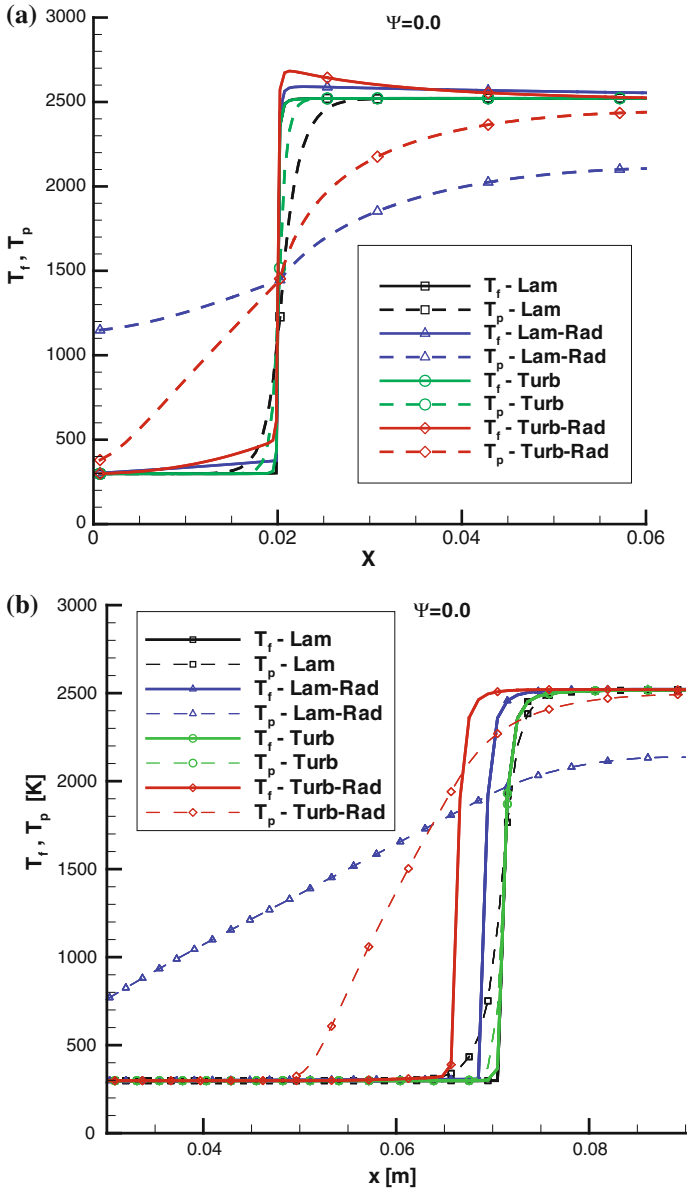

Fig. 4.5 Comparison of different model solutions: **a** U_{in} = 0.1 m/s, **b** U_{in} = 1.0 m/s

air or gas velocity, the flame front moves towards the exit of the burner. Results herein motivates further research work on the subject of reactive turbulent flow in porous burners and should be seen as a preliminary step towards reliable simulation of real porous combustors.

References

1. Pop I, Ingham DB (2001) Convective heat transfer: mathematical and computational modeling of viscous fluids and porous media. Pergamon, Oxford
2. Vafai K (ed) (2005) Handbook of porous media, 2nd edn. Taylor and Francis, New York
3. Ingham DB, Pop I (eds) (2005) Transport phenomena in porous media, vol 3. Elsevier, Oxford
4. Vadasz P (2008) Emerging topics in heat and mass transfer in porous media. Springer, New York
5. Nield DA, Bejan A (2013) Convection in porous media, 4th edn. Springer, New York
6. Vafai K (2010) Porous media: applications in biological systems and biotechnology. CRC Press, Tokyo
7. Babkin VS (1993) Filtration combustion of gases—present state of affairs and prospects. Pure Appl Chem 65(2):335–344
8. Mohamad AA, Ramadhyani S, Viskanta R (1994) Modeling of combustion and heat-transfer in a packed-bed with embedded coolant tubes. Int J Heat Mass Tran 37(8):1181–1191
9. Howell JR, Hall MJ, Ellzey JL (1996) Combustion of hydrocarbon fuels within porous inert media. Prog Energ Combust 22(2):121–145
10. Bouma PH, De Goey LPH (1999) Premixed combustion on ceramic foam burners. Combust Flame 119(1–2):133–143
11. Henneke MR, Ellzey JL (1999) Modeling of filtration combustion in a packed bed. Combust Flame 117(4):832–840
12. Oliveira AAM, Kaviany M (2001) Non equilibrium in the transport of heat and reactants in combustion in porous media. Prog Energ Combust 27(5):523–545
13. Lammers FA, De Goey LPH (2003) A numerical study of flash back of laminar premixed flames in ceramic-foam surface burners. Combust Flame 133(1–2):47–61
14. Leonardi SA, Viskanta R, Gore JP (2003) Analytical and experimental study of combustion and heat transfer in submerged flame metal fiber burners/heaters. J Heat Transf 125(1):118–125
15. Wood S, Harries AT (2008) Porous burners for lean-burn applications. Prog Energ Combust 34:667–684
16. Abdul Mujeebu M, Abdullah MZ, Abu Bakar MZ, Mohamad AA, Abdullaha MK (2009) A review of investigations on liquid fuel combustion in porous inert media. Prog Energ Combust 35:216–230
17. Hsu PF, Howell JR, Matthews RD (1993) A Numerical investigation of premixed combustion within porous inert media. J Heat Transf 115:744–750
18. Peard TE, Peters JE, Brewster MQ, Buckius RO (1993) Radiative heat transfer augmentation in gas-fired radiant tube burner by porous inserts: effect on insert geometry. Exp Heat Transf 6:273–286
19. Lim IG, Matthews RD (1993) Development of a model for turbulent combustion within porous inert media. In: Transport phenomena in thermal engineering. Begell House Inc Publications, New York, pp 631–636
20. Jones WP, Launder BE (1972) The prediction of laminarization with two-equation model of turbulence. Int J Heat Mass Transf 15:301–314
21. Sahraoui M, Kaviany (1995) Direct simulation vs time-averaged treatment of adiabatic, premixed flame in a porous medium. Int J Heat Mass Transf 18:2817–2834
22. Pedras MHJ, de Lemos MJS (2001) Simulation of turbulent flow in porous media using a spatially periodic array and a low re two-equation closure. Numer Heat Transf—Part A Appl 39:35–59
23. Pedras MHJ, de Lemos MJS (2003) Computation of turbulent flow in porous media using a low reynolds k- model and an infinite array of transversally-displaced elliptic rods. Numer Heat Transf Part A—Appl 43(6):585–602
24. de Lemos MJS (2005) Turbulent kinetic energy distribution across the interface between a porous medium and a clear region. Int Commun Heat Mass 32(1–2):107–115

25. Santos NB, de Lemos MJS (2006) Flow and heat transfer in a parallel plate channel with porous and solid baffles. Numer Heat Transf—Part A 49(5):471–494
26. Assato M, Pedras MHJ, de Lemos MJS (2005) Numerical solution of turbulent channel flow past a backward-facing step with a porous insert using linear and nonlinear k-models. J Porous Media 8(1):13–29
27. Braga EJ, de Lemos MJS (2004) Turbulent natural convection in a porous square cavity computed with a macroscopic k-ε model. Int J Heat Mass Tran 47(26):5639–5650
28. Kuznetsov AV, Cheng L, Xiong M (2002) Effects of thermal dispersion and turbulence in forced convection in a composite parallel-plate channel: Investigation of constant wall heat flux and constant wall temperature cases. Numer Heat Transf Part A-Appl 42:365–383
29. Kuznetsov AV (2004) Numerical modeling of turbulent flow in a composite porous/fluid duct utilizing a two layer k-epsilon model to account for interface roughness. Int J Therm Sci 43:1047–1056
30. de Lemos MJS (2009) Numerical simulation of turbulent combustion in porous materials. Int Commun Heat Mass Transf 36:996–1001
31. de Lemos MJS (2010) Analysis of turbulent combustion in inert porous media. Int Commun Heat Mass Transf 37(4):331–336
32. Coutinho JEA, de Lemos MJS (2012) Laminar flow with combustion in inert porous media. Int Commun Heat Mass Transf 39:896–903
33. de Lemos MJS (2005) Fundamentals of the double—decomposition concept for turbulent transport in permeable media. Materialwiss Werkstofftech 36(10):586
34. Saito M, de Lemos MJS (2005) Interfacial heat transfer coefficient for non-equilibrium convective transport in porous media. Int Commun Heat Mass 32(5):667–677
35. Saito M, de Lemos MJS (2006) A correlation for interfacial heat transfer coefficient for turbulent flow over an array of square rods. J Heat Transf 128(5):444–452
36. Slattery JC (1967) Flow of viscoelastic fluids through porous media. AICHE J 13:1066–1071
37. Whitaker S (1969) Advances in theory of fluid motion in porous media. Ind Eng Chem 61:14–28
38. Gray WG, Lee PCY (1977) On the theorems for local volume averaging of multiphase system. Int J Multiphase Flow 3:333–340
39. Kuwahara F, Shirota M, Nakayama A (2001) A numerical study of interfacial convective heat transfer coefficient in two-energy equation model for convection in porous media. Int J Heat Mass Transf 44:1153–1159
40. Malico I, Pereira JCF (1999) Numerical predictions of porous burners with integrated heat exchanger for household applications. J Porous Media 2(2):153–162
41. Mohamad AA, Viskanta R, Ramadhyani S (1994) Numerical prediction of combustion and heat transfer in a packed bed with embedded coolant tubes. Combust Sci Technol 96:387–407
42. Kuo KK (1986) Principles of combustion. John Wiley and Sons, New York
43. Turns SR (1996) An introduction to combustion: concepts and applications. McGraw-Hill, New York
44. Trimis D, Durst F (1996) Combustion in a porous medium—advances and applications. Combust Sci Technol 121:153–168
45. Patankar SV (1980) Numer Heat Transf and Fluid Flow. Hemisphere, Washington, DC
46. Pereira FM (2002) Medição de Características Térmicas e Estudo do Mecanismo de Estabilização de chama em Queimadores Porosos Radiantes, Federal de Santa Catarina (*in Portuguese*), Florianópolis, Brazil

Chapter 5
Double Diffusion

5.1 Introduction

Analyses of double-diffusive phenomena in free convection in permeable media has many environmental and industrial applications, such as in oil and gas extraction, movement of gas concentration into the ground, contaminant dispersion in soils, grain storage and drying, petrochemical processes, electrochemical processes, to mention a few [1–9]. In some specific applications, the voids are large enough and the fluid mixture may become turbulent. In such instances, difficulties arise in the proper mathematical modeling of the transport processes under both temperature and concentration gradients.

Usually, modeling of macroscopic transport for incompressible flows in rigid porous media has been based on the volume-average methodology for either heat or mass transfer [10–14]. If fluctuations in time are also of concern due the existence of turbulence in the intra-pore space, a variety of mathematical models have been published in the literature in the last decade. One of such views, which entails simultaneous application of both time and volume averaging operators to all governing equations, has been organized and published in a book [15] that describes, in detail, an idea known in the literature as the double-decomposition concept (see Chap. 3 in [15] for details).

In an earlier work [16], double-diffusive effects in porous media have been treated considering thermal equilibrium between the porous matrix and the permeating fluid. Or say, in [16] the fluid temperate was assumed to be the same of that of the solid when analyzing double-diffusive mechanisms. Later [17], buoyancy-free flows were investigated with the so-called Two-Energy-Equation Model, or 2EEM for short, which is based on the Local Thermal Non-equilibrium Hypothesis (LTNE) meaning that the average temperature of the fluid is not equal to the average temperature of the solid matrix. However, in [17] no double-diffusion was considered.

M.J.S. de Lemos, *Thermal Non-Equilibrium in Heterogeneous Media*,
SpringerBriefs in Computational Mechanics,
DOI 10.1007/978-3-319-14666-9_5

Therefore, the purpose of this contribution is to extend the work of [16] on turbulent double-diffusion using only one energy equation, assuming now the thermal non-equilibrium hypotheses of [17], which requires an independent energy balance for each phase. As such, the expectation herein is that, by combining now such two models that were developed on separate, a larger number of physical processes can now be more realistically tackled.

5.2 Mass Transport

The steady-state local (microscopic) instantaneous transport equations for an incompressible binary fluid mixture with constant properties flowing in an inert heterogeneous medium are given in details elsewhere and for that, they will be just repeated here. They read:

Within the fluid:

$$\text{Continuity } \nabla \cdot \mathbf{u} = 0 \tag{5.1}$$

$$\text{Momentum } \rho \nabla \cdot (\mathbf{uu}) = -\nabla p + \mu \nabla^2 \mathbf{u} + \rho\, \mathbf{g} \tag{5.2}$$

$$\text{Energy-Fluid Phase}: \ (\rho c_p)_f \left\{ \nabla \cdot (\mathbf{u} T_f) \right\} = \nabla \cdot (k_f \nabla T_f) + S_f \tag{5.3}$$

$$\text{Mass concentration}: \ \rho \nabla \cdot (\mathbf{u}\, m_\ell + \mathbf{J}_\ell) = \rho\, R_\ell \tag{5.4}$$

Within the solid:

$$\text{Energy-Solid Phase (Porous Matrix)}: \ 0 = \nabla \cdot (k_s \nabla T_s) + S_s \tag{5.5}$$

where $\mathbf{u}$ is the mass-averaged velocity of the mixture, $\mathbf{u} = \sum_\ell m_\ell \mathbf{u}_\ell$, $\mathbf{u}_\ell$ is the velocity of species ℓ, m_ℓ is the mass fraction of component ℓ, defined as $m_\ell = \rho_\ell / \rho$, ρ_ℓ is the mass density of species ℓ (mass of ℓ over total mixture volume), ρ is the bulk density of the mixture ($\rho = \sum_\ell \rho_\ell$), p is the pressure, μ is the fluid mixture viscosity, $\mathbf{g}$ is the gravity acceleration vector, c_p is the specific heat, the subscripts f and s refer to fluid and solid phases, respectively, T_f and T_s are the fluid and solid temperature, k_f and k_s are the fluid and solid thermal conductivities, c_p is the specific heat and S is the heat generation term. If there is no heat generation either in the solid or in the fluid, one has further $S_f = S_s = 0$. The generation rate of species ℓ per unit of mixture mass is given in (5.4) by R_ℓ. Also, as pointed out in [16], an alternative way of writing the mass transport equation is using the volumetric molar concentration C_ℓ (mol of ℓ over total mixture volume), the molar weight M_ℓ (g/mol of ℓ) and the molar generation/destruction rate R_ℓ^* (mol of ℓ/total mixture volume), giving:

$$M_\ell \nabla \cdot (\mathbf{u}\, C_\ell + \mathbf{J}_\ell) = M_\ell R_\ell^* \tag{5.6}$$

Further, the mass diffusion flux $\mathbf{J}_\ell$ (mass of ℓ per unit area per unit time) in (5.4) or (5.6) is due to the velocity slip of species ℓ,

$$\mathbf{J} = \rho_\ell(\mathbf{u}_\ell - \mathbf{u}) = -\rho_\ell D_\ell \nabla m_\ell = -M_\ell D_\ell \nabla C_\ell \tag{5.7}$$

where D_ℓ is the diffusion coefficient of species ℓ into the mixture. The second equality in Eq. (5.7) is known as Fick's Law, which is a constitutive equation strictly valid for binary mixtures under the absence of any additional driving mechanisms for mass transfer [10]. Therefore, no *Soret* or *Dufour* effects are here considered.Rearranging (5.6) for an inert species, dividing it by M_ℓ and dropping the index ℓ for a simple binary mixture, one has,

$$\nabla \cdot (\mathbf{u}\, C) = \nabla \cdot (D \nabla C) \tag{5.8}$$

If one considers that the density in the last term of (5.2) varies with fluid temperature and concentration, for natural convection flow, the Boussinesq hypothesis reads, after renaming this density ρ_T,

$$\rho_T \cong \rho\,[1 - \beta(T_f - T_{ref}) - \beta_C(C - C_{ref})] \tag{5.9}$$

where the subscript *ref* indicates a reference value and β and β_C are the thermal and salute expansion coefficients, respectively, defined by,

$$\beta = -\frac{1}{\rho}\frac{\partial \rho}{\partial T_f}\bigg|_{p,C},\ \beta_C = -\frac{1}{\rho}\frac{\partial \rho}{\partial C}\bigg|_{p,T_f} \tag{5.10}$$

Here, it is interesting to point out that in [15] the temperature used in Eq. (5.9) was the same of that of the solid, $T = T_f = T_s$. Further, it is important to note that, as it is going to be shown below, after volume averaging Eqs. (5.3) and (2.4), T_f is going to be related to T_s due to the exchange of heat between the two phases across the interstitial area. Also, Eq. (5.9) is an approximation of Eq. (5.10) and shows how density varies with the fluid temperature and mass concentration in the body force term of the momentum equation.

Substituting now (5.9) into (5.2), one has,

$$\rho \nabla \cdot (\mathbf{uu}) = -\nabla p + \mu \nabla^2 \mathbf{u} + \rho\, \mathbf{g}\,[1 - \beta\,(T_f - T_{ref}) - \beta\,(C - C_{ref})] \tag{5.11}$$

Thus, the momentum equation becomes after some rearrangement,

$$\rho \nabla \cdot (\mathbf{uu}) = -(\nabla p)^* + \mu \nabla^2 \mathbf{u} - \rho\, \mathbf{g}[(\beta(T_f - T_{ref}) + \beta_C(C - C_{ref})\,] \tag{5.12}$$

where $(\nabla p)^* = \nabla p - \rho\, \mathbf{g}$ is a modified pressure gradient.

5.3 Averaging Operators

For the sake of completeness, although the information below has been given in detail above and in a number of articles and books, including [15] for example, it is convenient to recall the definition of time average and volume average in this chapter.

The time average of a general quantity φ is defined as:

$$\bar{\varphi} = \frac{1}{\Delta t}\int_{t}^{t+\Delta t} \varphi \, dt \tag{5.13}$$

where the time interval Δt is small compared to the fluctuations of the average value, $\bar{\varphi}$, but large enough to capture turbulent fluctuations of φ. Time decomposition can then be written as,

$$\varphi = \bar{\varphi} + \varphi' \tag{5.14}$$

with $\overline{\varphi'} = 0$. Here, φ' is the *time fluctuation* of φ around its average $\bar{\varphi}$.

Further, the volume average of φ taken over a Representative Elementary Volume (REV) in a porous medium can be written as [18–20]:

$$\langle \varphi \rangle^{v} = \frac{1}{\Delta V}\int_{\Delta V} \varphi \, dV \tag{5.15}$$

The value $\langle \varphi \rangle^{v}$ is defined for any point $\boldsymbol{x}$ surrounded by a REV of size ΔV. This average is related to the *intrinsic* average for the fluid phase as:

$$\langle \varphi \rangle^{v} = \phi \, \langle \varphi \rangle^{i} \tag{5.16}$$

where $\phi = \Delta V_f / \Delta V$ is the medium porosity and ΔV_f is the volume occupied by the fluid in a REV. Furthermore, one can write:

$$\varphi = \langle \varphi \rangle^{i} + {}^{i}\varphi \tag{5.17}$$

with $\langle {}^{i}\varphi \rangle^{i} = 0$. In Eq. (5.17), ${}^{i}\varphi$ is the *spatial deviation* of φ with respect to the intrinsic average $\langle \varphi \rangle^{i}$.

Further, the local volume average theorem can be expressed as [17–19]:

$$\begin{aligned}
\langle \nabla \varphi \rangle^{v} &= \nabla(\phi \langle \varphi \rangle^{i}) + \frac{1}{\Delta V}\int_{A_i} \mathbf{n}_i \varphi \, dS \\
\langle \nabla \cdot \boldsymbol{\varphi} \rangle^{v} &= \nabla \cdot (\phi \langle \boldsymbol{\varphi} \rangle^{i}) + \frac{1}{\Delta V}\int_{A_i} \mathbf{n}_i \cdot \boldsymbol{\varphi} \, dS \\
\left\langle \frac{\partial \varphi}{\partial t} \right\rangle^{v} &= \frac{\partial}{\partial t}(\phi \langle \varphi \rangle^{i}) - \frac{1}{\Delta V}\int_{A_i} \mathbf{n}_i \cdot (\mathbf{u}_i \varphi) dS
\end{aligned} \tag{5.18}$$

where $\mathbf{n}_i$ is the unit vector normal to the fluid-solid interface, pointing from the fluid towards the solid phase, A_i is the fluid-solid interface area within the REV. It is important to emphasize that A_i should not be confused with the surface area surrounding volume ΔV. In [15] it is shown that for a rigid, homogeneous porous medium saturated with an incompressible fluid, the following relationships apply:

$$\begin{aligned} \overline{\langle\varphi\rangle^i} &= \langle\bar{\varphi}\rangle^i \\ \bar{\varphi} &= \overline{{}^i\varphi} \\ \langle\varphi'\rangle^i &= \langle\varphi\rangle^{i'} \end{aligned} \tag{5.19}$$

Therefore, a general quantity ϕ can be expressed by either,

$$\varphi = \overline{\langle\varphi\rangle^i} + \langle\varphi\rangle^{i'} + \overline{{}^i\varphi} + {}^i\varphi' \tag{5.20}$$

or

$$\varphi = \langle\bar{\varphi}\rangle^i + {}^i\bar{\varphi} + \langle\varphi'\rangle^i + {}^i\varphi' \tag{5.21}$$

Expressions (5.20) and (5.21) encompass what is recalled in the literature as the "double decomposition" concept where ${}^i\phi'$ can be understood as either the *time fluctuation of the spatial deviation* or the *spatial deviation of the time fluctuation*. Also, $\langle {}^i\varphi'\rangle^i = \overline{{}^i\varphi'} = 0$.

5.4 Time Averaging for Buoyant Flows

In order to apply the time average operator to Eqs. (2.4), (5.1), (5.3), (5.8) and (5.12), one considers,

$$\mathbf{u} = \bar{\mathbf{u}} + \mathbf{u}';\ T_f = \bar{T}_f + T_f';\ T_s = \bar{T}_s + T_s',\ C = \bar{C} + C',\ p = \bar{p} + p' \tag{5.22}$$

Substituting (5.22) into the governing equations and considering constant properties for both the fluid and the solid,

$$\nabla \cdot \bar{\mathbf{u}} = 0 \tag{5.23}$$

$$\rho\nabla\cdot(\bar{\mathbf{u}}\bar{\mathbf{u}}) = -(\nabla\bar{p})^* + \mu\nabla^2\bar{\mathbf{u}} + \nabla\cdot(-\rho\,\overline{\mathbf{u}'\mathbf{u}'}) - \rho\,\mathbf{g}\,[\beta\,(\bar{T}_f - T_{ref}) + \beta_C(\bar{C} - C_{ref})] \tag{5.24}$$

$$(\rho c_p)_f \nabla\cdot(\bar{\mathbf{u}}\overline{T_f}) = \nabla\cdot(k\nabla\bar{T}_f) + \nabla\cdot(-\rho\,c_p\overline{\mathbf{u}'T_f'}) \tag{5.25}$$

$$0 = \nabla \cdot (k_s \nabla \bar{T}_s). \tag{5.26}$$

$$\nabla \cdot (\bar{\mathbf{u}}\, \bar{C}) = -\nabla \cdot (D \nabla \bar{C}) + \nabla \cdot (-\overline{\mathbf{u}' C'}) \tag{5.27}$$

For clear fluid, the use of the eddy-diffusivity concept for expressing the stress–strain rate relationship for the Reynolds stress appearing in (5.24) gives,

$$-\rho \overline{\mathbf{u}'\mathbf{u}'} = \mu_t 2\overline{\mathbf{D}} - \frac{2}{3}\rho k \mathbf{I} \tag{5.28}$$

where $\overline{\mathbf{D}} = [\nabla \bar{\mathbf{u}} + (\nabla \bar{\mathbf{u}})^T]/2$ is the mean deformation tensor, $k = \overline{\mathbf{u}' \cdot \mathbf{u}'}/2$ is the turbulent kinetic energy per unit mass, μ_t is the turbulent viscosity and $\mathbf{I}$ is the unity tensor. Similarly, for the turbulent heat flux on the r.h.s. of (5.25) and (5.27) the eddy diffusivity concept reads,

$$-\rho\, c_p \overline{\mathbf{u}'\, T_f'} = c_p \frac{\mu_t}{\mathrm{Pr}_t} \nabla \bar{T}_f; \; -\rho \overline{\mathbf{u}'\, C'} = \frac{\mu_t}{\mathrm{Sc}_t} \nabla \bar{C} \tag{5.29}$$

where pr_t and Sc_t are known as the turbulent Prandtl and Schmidt numbers, respectively.

Further, a transport equation for the turbulent kinetic energy is obtained by multiplying first, by $\mathbf{u}'$, the difference between the instantaneous and the time-averaged momentum equations. Thus, applying further the time average operator to the resulting product, one has,

$$\rho \nabla \cdot (\bar{\mathbf{u}} k) = -\rho \nabla \cdot \overline{\left[\mathbf{u}' \left(\frac{p'}{\rho} + q\right)\right]} + \mu \nabla^2 k + P + G_T + G_C - \rho\varepsilon \tag{5.30}$$

where $P = -\rho \overline{\mathbf{u}'\mathbf{u}'} : \nabla \bar{\mathbf{u}}$ is the generation rate of k due to gradients of the mean velocity and

$$G_T = -\rho\, \beta\, \mathbf{g} \cdot \overline{\mathbf{u}' T_f'} = \beta \frac{\mu_t}{\mathrm{Pr}_t}\, \mathbf{g} \cdot \nabla \bar{T}_f \tag{5.31}$$

$$G_C = -\rho\, \beta_C\, \mathbf{g} \cdot \overline{\mathbf{u}' C'} = \beta_C \frac{\mu_t}{\mathrm{Sc}_t}\, \mathbf{g} \cdot \nabla \bar{C} \tag{5.32}$$

are the thermal and concentration generation rates of k due to temperature and concentration fluctuations, respectively. Also, $q = \mathbf{u}' \cdot \mathbf{u}'/2$ and, on the right of Eqs. (5.31) and (5.32), the models in (5.29) have been applied.

5.5 Volume Averaging

5.5.1 Mean Continuity Equation

This section presents first equations for buoyancy free flows. When the average operators (5.13)–(5.15) are simultaneously applied over Eqs. (2.1) and (2.2), macroscopic equations for turbulent flow are obtained. Volume integration is performed over a Representative Elementary Volume (REV) shown in resulting in,

$$\nabla \cdot \bar{\mathbf{u}}_D = 0. \tag{5.33}$$

where, $\bar{\mathbf{u}}_D = \phi \langle \bar{\mathbf{u}} \rangle^i$ and $\langle \bar{\mathbf{u}} \rangle^i$ identifies the intrinsic (liquid) average of the time-averaged velocity vector $\bar{\mathbf{u}}$.

For non-buoyant flows, macroscopic equations considering turbulence have been already derived in detail for momentum, heat, and mass transfer [15] and for this reason their derivation need not to be repeated here. They read:

5.5.2 Mean Momentum Transport

$$\rho \nabla \cdot \left(\frac{\bar{\mathbf{u}}_D \bar{\mathbf{u}}_D}{\phi} \right) = -\nabla (\phi \langle \bar{p} \rangle^i) + \mu \nabla^2 \bar{\mathbf{u}}_D + \nabla \cdot (-\rho \phi \langle \overline{\mathbf{u}' \mathbf{u}'} \rangle^i) - \left[\frac{\mu \phi}{K} \bar{\mathbf{u}}_D + \frac{c_F \phi \rho |\bar{\mathbf{u}}_D| \bar{\mathbf{u}}_D}{\sqrt{K}} \right] \tag{5.34}$$

$$-\rho \phi \langle \overline{\mathbf{u}' \mathbf{u}'} \rangle^i = \mu_{t_\phi} 2 \langle \bar{\mathbf{D}} \rangle^{\mathbf{v}} - \frac{2}{3} \phi \rho \langle k \rangle^i \mathbf{I} \tag{5.35}$$

$$\langle \bar{\mathbf{D}} \rangle^v = \frac{1}{2} \{ \nabla (\phi \langle \bar{\mathbf{u}} \rangle^i) + [\nabla (\phi \langle \bar{\mathbf{u}} \rangle^i)]^T \} \tag{5.36}$$

$$\langle k \rangle^i = \langle \overline{\mathbf{u}' \cdot \mathbf{u}'} \rangle^i / 2$$

$$\mu_{t_\phi} = \rho \, c_\mu f_\mu \frac{\langle k \rangle^{i2}}{\langle \varepsilon \rangle^i} \tag{5.37}$$

where c_μ is a constant, f_μ is damping function to be presented.

5.5.3 Macroscopic Turbulence Field

The intrinsic turbulent kinetic energy per unit mass and its dissipation rate are governed by the following equations,

$$\rho\left[\frac{\partial}{\partial t}\left(\phi\langle k\rangle^{i}\right)+\nabla\cdot\left(\bar{\mathbf{u}}_{D}\langle k\rangle^{i}\right)\right]=\nabla\cdot\left[\left(\mu+\frac{\mu_{t_{\phi}}}{\sigma_{k}}\right)\nabla\left(\phi\langle k\rangle^{i}\right)\right]-\rho\langle\overline{\mathbf{u}'\mathbf{u}'}\rangle^{i}:\nabla\bar{\mathbf{u}}_{D}+c_{k}\rho\frac{\phi\langle k\rangle^{i}\left|\bar{\mathbf{u}}_{D}\right|}{\sqrt{K}}-\rho\phi\langle\varepsilon\rangle^{i} \tag{5.38}$$

$$\rho\left[\frac{\partial}{\partial t}\left(\phi\langle\varepsilon\rangle^{i}\right)+\nabla\cdot\left(\bar{\mathbf{u}}_{D}\langle\varepsilon\rangle^{i}\right)\right]=\nabla\cdot\left[\left(\mu+\frac{\mu_{t_{\phi}}}{\sigma_{\varepsilon}}\right)\nabla\left(\phi\langle\varepsilon\rangle^{i}\right)\right]+c_{1}\left(-\rho\langle\overline{\mathbf{u}'\mathbf{u}'}\rangle^{i}:\nabla\bar{\mathbf{u}}_{D}\right)\frac{\langle\varepsilon\rangle^{i}}{\langle k\rangle^{i}}+c_{2}c_{k}\rho\frac{\phi\langle\varepsilon\rangle^{i}\left|\bar{\mathbf{u}}_{D}\right|}{\sqrt{K}}-c_{2}f_{2}\rho\phi\frac{\langle\varepsilon\rangle^{i2}}{\langle k\rangle^{i}} \tag{5.39}$$

where the c's are constants and f_2 is a another damping function. Usually, two forms of the k-ε model are employed, namely the High Reynolds (Launder and Spalding [20]) and Low Reynolds number (Abe et al. [21]) turbulence models. The constants and formulae used as damping functions were showed in Table 3.1.

5.6 Two-Energy Equation Model (2EEM)

Similarly, macroscopic energy equations are obtained for both fluid and solid phases by applying time and volume average operators to Eqs. (2.3) and (2.4). As in the flow case, volume integration is performed over a Representative Elementary Volume (REV), resulting in,

$$\left(\rho c_{p}\right)_{f}\nabla\cdot\left\{\phi\left(\langle\bar{\mathbf{u}}\rangle^{i}\langle\overline{T_{f}}\rangle^{i}+\underbrace{\langle{}^{i}\bar{\mathbf{u}}^{i}\overline{T_{f}}\rangle^{i}}_{\text{thermal disperson}}+\underbrace{\overline{\langle\mathbf{u}'\rangle^{i}\langle T_{f}'\rangle^{i}}}_{\text{turbulent heat flux}}+\underbrace{\langle{}^{i}\overline{\mathbf{u}'{}^{i}T_{f}'}\rangle^{i}}_{\text{turbulent thermal disperson}}\right)\right\}=\underbrace{\nabla\cdot\left[k_{f}\nabla\left(\phi\langle\overline{T_{f}}\rangle^{i}\right)+\frac{1}{\Delta V}\int_{A_{i}}\mathbf{n}_{i}\,k_{f}\overline{T_{f}}\,dA\right]}_{\text{conduction}}+\underbrace{\frac{1}{\Delta V}\int_{A_{i}}\mathbf{n}_{i}\cdot k_{f}\nabla\overline{T_{f}}\,dA}_{\text{interfacial heat transfer}} \tag{5.40}$$

where the expansion,

$$\langle \overline{\mathbf{u}'T_f'} \rangle^i = \langle \overline{(\langle \mathbf{u}' \rangle^i + {}^i\mathbf{u}')\,(\langle T_f' \rangle^i + {}^iT')} \rangle^i = \overline{\langle \mathbf{u}' \rangle^i \langle T_f' \rangle^i} + \langle \overline{{}^i\mathbf{u}'\,{}^iT_f'} \rangle^i \tag{5.41}$$

has been used in light of the double decomposition concept given by Eq. (5.19)–(4.35) (see [15] for details). For the solid phase, one has,

$$0 = \underbrace{\nabla \cdot \left\{ k_s \nabla \left[(1-\phi)\,\langle \overline{T_s} \rangle^i \right] - \frac{1}{\Delta V} \int_{A_i} \mathbf{n}_i\, k_s \overline{T_s}\, dA \right\}}_{\text{conduction}} - \underbrace{\frac{1}{\Delta V} \int_{A_i} \mathbf{n}_i \cdot k_s \nabla \overline{T_s}\, dA}_{\text{interfacial heat transfer}} \tag{5.42}$$

In (5.40) and (5.42), $\langle \overline{T_s} \rangle^i$ and $\langle \overline{T_f} \rangle^i$ denote the intrinsic time-average temperature of solid and fluid phases, respectively. These equations are the macroscopic energy balances for the fluid and the porous matrix (solid), respectively.

Also, in order to use Eqs. (5.40) and (5.42), the underscored terms have to be modeled as a function of $\langle \overline{T_s} \rangle^i$ and $\langle \overline{T_f} \rangle^i$. To accomplish this, a gradient type diffusion model is used for all terms not involving the interfacial heat transfer, in the form,

Turbulent heat flux:

$$-\left(\rho\, c_p\right)_f \left(\phi\ \overline{\langle \mathbf{u}' \rangle^i \langle T_f' \rangle^i} \right) = \mathbf{K}_t \cdot \nabla \langle \bar{T}_f \rangle^i \tag{5.43}$$

Thermal dispersion:

$$-\left(\rho\, c_p\right)_f \left(\phi\ \langle {}^i\bar{\mathbf{u}}\, {}^i\overline{T_f} \rangle^i \right) = \mathbf{K}_{disp} \cdot \nabla \langle \bar{T}_f \rangle^i \tag{5.44}$$

Turbulent thermal dispersion:

$$-\left(\rho\, c_p\right)_f \left(\phi\ \langle \overline{{}^i\mathbf{u}'\,{}^iT_f'} \rangle^i \right) = \mathbf{K}_{disp,t} \cdot \nabla \langle \bar{T}_f \rangle^i \tag{5.45}$$

Local conduction:

$$\begin{aligned} \nabla \cdot \left[\frac{1}{\Delta V} \int_{A_i} \mathbf{n}_i\, k_f \overline{T_f}\, dA \right] &= \mathbf{K}_{f,s} \cdot \nabla \langle \bar{T}_s \rangle^i \\ -\nabla \cdot \left[\frac{1}{\Delta V} \int_{A_i} \mathbf{n}_i\, k_s \overline{T_s}\, dA \right] &= \mathbf{K}_{s,f} \cdot \nabla \langle \bar{T}_f \rangle^i \end{aligned} \tag{5.46}$$

Finally, Eqs. (5.40) and (5.42) can be rewritten using the concept of overall effective conduction in the form,

$$\left(\rho\, c_p\right)_f \nabla \cdot \left(\mathbf{u}_D \langle T_f \rangle^i\right) = \nabla \cdot \left\{ \mathbf{K}_{eff,f} \cdot \nabla \langle T_f \rangle^i \right\} + \frac{1}{\nabla V} \int_{A_i} \mathbf{n}_i \cdot k_f \nabla T_f dA \tag{5.47}$$

$$0 = \nabla \cdot \left\{ \mathbf{K}_{eff,s} \cdot \nabla \langle T_s \rangle^i \right\} - \frac{1}{\Delta V} \int_{A_i} \mathbf{n}_i \cdot k_s \nabla T_s \, dA \tag{5.48}$$

where

$$\mathbf{K}_{eff,f} = \left[\phi\, k_f\right] \mathbf{I} + \mathbf{K}_{f,s} + \mathbf{K}_t + \mathbf{K}_{disp} + \mathbf{K}_{disp,t} \tag{5.49}$$

$$\mathbf{K}_{eff,s} = \left[(1-\phi)\, k_s\right] \mathbf{I} + \mathbf{K}_{s,f} \tag{5.50}$$

The turbulent heat flux and turbulent thermal dispersion terms, $\mathbf{K}_t$ and $\mathbf{K}_{disp,t}$, are here modeled through the Eddy diffusivity concept as [17]:

$$\mathbf{K}_t + \mathbf{K}_{disp,t} = \phi \left(\rho\, c_p\right)_f \frac{\nu_{t_\phi}}{\mathrm{Pr}_{t_\phi}} \mathbf{I} \tag{5.51}$$

where Pr_{t_ϕ} is the macroscopic turbulent Prandtl number for the fluid energy equation.

5.6.1 *Interfacial Heat Transfer,* $\mathbf{h_i}$

In Eqs. (5.40) and (5.42) the heat transferred between the two phases can be modeled by means of a film coefficient h_i such that,

$$h_i a_i \left(\langle T_s \rangle^i - \langle T_f \rangle^i \right) = \frac{1}{\nabla V} \int_{A_i} \mathbf{n}_i \cdot k_f \nabla T_f dA = \frac{1}{\Delta V} \int_{A_i} \mathbf{n}_i \cdot k_s \nabla T_s \, dA \tag{5.52}$$

where $a_i = A_i / \nabla V$ is the interfacial area per unit volume. In porous media, the high values of a_i make them attractive for transferring thermal energy via conduction through the solid followed by convection to a fluid stream.

$$\left(\rho\, c_p\right)_f \nabla \cdot \left(\mathbf{u}_D \langle \overline{T_f} \rangle^i\right) = \nabla \cdot \left\{ \mathbf{K}_{eff,f} \cdot \nabla \langle \overline{T_f} \rangle^i \right\} + h_i a_i \left(\langle \overline{T_s} \rangle^i - \langle \overline{T_f} \rangle^i \right), \tag{5.53}$$

$$0 = \nabla \cdot \left\{ \mathbf{K}_{eff,s} \cdot \nabla \langle \overline{T_s} \rangle^i \right\} - h_i a_i \left(\langle \overline{T_s} \rangle^i - \langle \overline{T_f} \rangle^i \right), \tag{5.54}$$

Wakao et al. [23] proposed a correlation for h_i for closely packed bed and compared results with their experimental data. This correlation reads,

$$\frac{h_i D}{k_f} = 2 + 1.1 Re_D^{0.6} Pr^{1/3} \tag{5.55}$$

Kuwahara et al. [24] also obtained the interfacial convective heat transfer coefficient for laminar flow, as follows,

$$\frac{h_i D}{k_f} = \left(1 + \frac{4(1-\phi)}{\phi}\right) + \frac{1}{2}(1-\phi)^{1/2} \mathrm{Re}_D \ \mathrm{Pr}^{1/3}, \text{ valid for } 0.2 < \phi < 0.9, \tag{5.56}$$

Equation (5.56) is based on porosity dependency and is valid for packed beds of particle diameter D.

Following this same methodology, in which the porous medium is considered an infinite number of solid square rods, Saito and de Lemos [16] proposed a correlation for obtaining the interfacial heat transfer coefficient for turbulent flow as,

$$\frac{h_i D}{k_f} = 0.08 \left(\frac{Re_D}{\phi}\right)^{0.8} Pr^{1/3}; \text{ for } 1.0x10^4 < \frac{Re_D}{\phi} < 2.0x10^7, \text{ valid for } 0.2 < \phi < 0.9, \tag{5.57}$$

Earlier, Table 2.1 had shown already the three abovementioned variant correlations for the fluid to solid heat transfer coefficient, h_i, and the specific surface area of the porous medium, a_i, which appears in both energy equations. In Table 2.1 Eq. (5.57) was presented as the proposed correlation obtained in Chap. 2 and described in detail by Saito and de Lemos [17].

5.7 Mass Transport

$$\nabla \cdot (\bar{\mathbf{u}}_D \langle \bar{C} \rangle^i) = \nabla \cdot \mathbf{D}_{eff} \cdot \nabla (\phi \langle \bar{C} \rangle^i) \tag{5.58}$$

$$\mathbf{D}_{eff} = \mathbf{D}_{disp} + \mathbf{D}_{diff} + \mathbf{D}_t + \mathbf{D}_{disp,t} \tag{5.59}$$

$$\mathbf{D}_{diff} = \langle D \rangle^i \mathbf{I} = \frac{1}{\rho} \frac{\mu_\phi}{Sc} \mathbf{I} \tag{5.60}$$

$$\mathbf{D}_t + \mathbf{D}_{disp,t} = \frac{1}{\rho} \frac{\mu_{t_\phi}}{Sc_{t\phi}} \mathbf{I} \tag{5.61}$$

where $Sc_{t\phi}$ is a macroscopic turbulent Schmidt number.

Coefficients $\mathbf{D}_{disp}, \mathbf{D}_t$ and $\mathbf{D}_{disp}, t$ in (5.58) appear due to the nonlinearity of the convection term. They come from the modeling of the following mechanisms:

Mass dispersion:

$$-\langle {}^i\bar{\mathbf{u}}\, {}^i\bar{C}\rangle^i = \mathbf{D}_{disp} \cdot \nabla \langle \bar{C}\rangle^i \tag{5.62}$$

Turbulent Mass Flux:

$$-\overline{\langle \mathbf{u}'\rangle^i \langle C'\rangle^i} = -\overline{\langle \mathbf{u}\rangle^{i'} \langle C\rangle^{i'}} = \mathbf{D}_t \cdot \nabla \langle \bar{C}\rangle^i \tag{5.63}$$

Turbulent Mass Dispersion;

$$-\langle \overline{{}^i\mathbf{u}'\, {}^iC'}\rangle^i = \mathbf{D}_{disp,t} \cdot \nabla \langle \bar{C}\rangle^i \tag{5.64}$$

Here also mechanisms (5.63) and (5.64) are added up as [15];

$$-\langle \overline{\mathbf{u}'C'}\rangle^i = \frac{1}{\rho}\frac{\mu_{t_\phi}}{Sc_{t\phi}} \nabla \langle \bar{C}\rangle^i = \langle D_t\rangle^i \nabla \langle \bar{C}\rangle^i = \ (\mathbf{D}_t + \mathbf{D}_{disp,t}) \cdot \nabla \langle \bar{C}\rangle^i \tag{5.65}$$

5.8 Double-Diffusion Effects with a 2EEM Model

5.8.1 Mean Flow

Focusing now attention to buoyancy effects only, application of the volume average procedure to the last term of (5.24) leads to,

$$\langle \rho\, \mathbf{g}\, [\beta(\bar{T}_f - T_{ref}) + \beta_C(\bar{C} - C_{ref})]\rangle^v = \frac{\Delta V_f}{\Delta V}\frac{1}{\Delta V_f}\int\limits_{\Delta V_f} \rho\, \mathbf{g}\, [\beta(\bar{T}_f - T_{ref}) + \beta_C(\bar{C} - C_{ref})]\, dV \tag{5.66}$$

Expanding the left hand side of (5.66) in light of (5.17), the buoyancy term becomes,

$$\begin{aligned} &\langle \rho\, \mathbf{g}\, [\beta\, (\bar{T}_f - T_{ref}) + \beta_C\, (\bar{C} - C_{ref})]\rangle^v \\ &\quad = \rho\, \mathbf{g}\, \phi[\, \beta_\phi(\langle \overline{T_f}\rangle^i - T_{ref}) + \beta_{C_\phi}(\langle \overline{C}\rangle^i - C_{ref})] \\ &\quad + \underbrace{\rho\, \mathbf{g}\beta\phi\, \overline{\langle {}^iT_f\rangle^i}}_{=0} + \underbrace{\rho\, \mathbf{g}\beta_C\phi\, \overline{\langle {}^iC\rangle^i}}_{=0} \end{aligned} \tag{5.67}$$

where the third and forth terms on the r.h.s. are null since $\langle {}^i\varphi\rangle^i = 0$

. Here, coefficients β_ϕ and β_{C_ϕ} are the *macroscopic* thermal and salute expansion coefficients, respectively. Assuming that gravity is constant over the REV, expressions for them based on (5.67) are given as,

$$\beta_\phi = \frac{\langle \rho\, \beta(\overline{T}_f - T_{ref})\rangle^v}{\rho\, \phi(\langle \overline{T}_f \rangle^i - T_{ref})};\ \beta_{C_\phi} = \frac{\langle \rho\, \beta_C(\overline{C} - C_{ref})\rangle^v}{\rho\, \phi(\langle \overline{C} \rangle^i - C_{ref})} \tag{5.68}$$

Including (5.67) into (5.34), the macroscopic time-mean Navier-Stokes (NS) equation for an incompressible fluid with constant properties is given as,

$$\begin{aligned}\rho\nabla\cdot\left(\frac{\bar{\mathbf{u}}_D\bar{\mathbf{u}}_D}{\phi}\right) =& -\nabla(\phi\langle\bar{p}\rangle^i) + \mu\nabla^2\bar{\mathbf{u}}_D + \nabla\cdot(-\rho\phi\langle\overline{\mathbf{u}'\mathbf{u}'}\rangle^i)\\ &-\rho\,\mathbf{g}\phi[\beta_\phi\,(\langle\overline{T}_f\rangle^i - T_{ref}) + \beta_{C_\phi}\,(\langle\overline{C}\rangle^i - C_{ref})]\\ &-\left[\frac{\mu\phi}{K}\bar{\mathbf{u}}_D + \frac{c_F\phi\rho\,|\bar{\mathbf{u}}_D|\bar{\mathbf{u}}_D}{\sqrt{K}}\right]\end{aligned} \tag{5.69}$$

where the superscript * on the pressure gradient that would appear in Eq. (5.69) by the volume-average of Eq. (5.24), has been dropped.

As pointed out by [15], it is interesting to comment on role of coefficients $^{\beta_\phi}$ and $^{\beta_{C_\phi}}$ on the overall mixture density value. Here, only fluids that became less dense with increasing temperature are considered. However, two situation might occurs when increasing $\langle\bar{C}\rangle^i$, namely the mixture might became less dense with the addition of a lighter solute, or else, a denser fluid may result by mixing a heavier component to it. Implications of that on the stability of the entire fluid system were discussed in [15] were more details can be found.

5.8.2 Turbulent Field

As mentioned, this work extends and combines earlier developments for turbulent double-diffusion using the thermal equilibrium model [16] with the hypothesis of thermal non-equilibrium [17]. For clear fluid, the buoyancy contribution to the k equation is given by Eqs. (5.31) and (5.32).

Volume averaging Eq. (5.31) in reference [16] has resulted in the term,

$$\langle G_T\rangle^v = G^i_\beta = \langle -\rho\beta\,\mathbf{g}\cdot\overline{\mathbf{u}'T'_f}\rangle^v = -\rho\beta^k_\phi\,\phi\,\mathbf{g}\cdot\langle\overline{\mathbf{u}'T'_f}\rangle^i = \beta^k_\phi\phi\frac{\mu_{t_\phi}}{\mathrm{Pr}_{t_\phi}}\mathbf{g}\cdot\nabla\langle\overline{T}_f\rangle^i \tag{5.70}$$

where the model in Eq. (5.29) has been applied. Equation (5.70) represents an additional macroscopic generation/destruction rate of $\langle k\rangle^i$ due to temperature variation in porous media, where β^k_ϕ is a macroscopic coefficient given by

$\beta_\phi^k = \frac{\langle \beta \overline{\mathbf{u}' T_f'} \rangle^v}{\phi \langle \overline{\mathbf{u}' T_f'} \rangle^i}$. In reference [15], coefficients β (Eq. 5.10), β_ϕ (Eq. 5.68) and β_ϕ^k (Eq. 5.70) were all assumed to be equal, for simplicity. Also, in [15] the temperature used in Eq. (5.70) was the same regardless of the phase. Here, however, it is the gradient of the intrinsic fluid temperature $\langle \overline{T_f} \rangle^i$ that is considered to promote the driving mechanism to generate/destroy turbulence.

In order to add the effect of concentration variation within the fluid, one applies the volume average operator to (5.32) such that,

$$\langle G_C \rangle^v = G^i_{\beta_C} = \langle -\rho \beta_C \, \mathbf{g} \cdot \overline{\mathbf{u}' C'} \rangle^v = -\rho \beta^k_{C_\phi} \, \phi \, \mathbf{g} \cdot \langle \overline{\mathbf{u}' C'} \rangle^i \tag{5.71}$$

where the coefficient $\beta^k_{C_\phi}$, for a constant value of $\mathbf{g}$ within the REV, is given by $\beta^k_{C_\phi} = \frac{\langle \beta_C \overline{\mathbf{u}' C'} \rangle^v}{\phi \langle \overline{\mathbf{u}' C'} \rangle^i}$, which, in turn, is not necessarily equal to β_{C_ϕ} given by (5.68). However, for the sake of simplicity and in the absence of better information, one can use a similar argument as in reference [15] and make use of the assumption $\beta_C = \beta_{C_\phi} = \beta^k_{C_\phi}$. Further, expanding the r.h.s. of (5.71) in light of (5.17) and (5.19), one has

$$\begin{aligned}
-\rho \, \beta^k_{C_\phi} \, \phi \, \mathbf{g} \cdot \langle \overline{\mathbf{u}' C'} \rangle^i &= -\rho \, \beta^k_{C_\phi} \, \phi \, \mathbf{g} \cdot \langle \overline{(\langle \mathbf{u}' \rangle^i + {}^i\mathbf{u}')(\langle C' \rangle^i + {}^i C')} \rangle^i \\
&= -\rho \, \beta^k_{C_\phi} \, \phi \, \mathbf{g} \cdot \left(\langle \langle \overline{\mathbf{u}' \rangle^i \langle C' \rangle^i} \rangle^i + \langle \overline{{}^i\mathbf{u}' \, {}^i C'} \rangle^i + \langle \langle \overline{\mathbf{u}' \rangle^i \, {}^i C'} \rangle^i + \langle \, \overline{{}^i\mathbf{u}' \langle C' \rangle^i} \rangle^i \right) \\
&= -\rho \, \beta^k_{C_\phi} \, \phi \, \mathbf{g} \cdot \left(\underbrace{\overline{\langle \mathbf{u} \rangle^{i'} \langle C \rangle^{i'}}}_{\mathbf{I}} + \underbrace{\langle \overline{{}^i\mathbf{u}' \, {}^i C'} \rangle^i}_{\mathbf{II}} + \underbrace{\overline{\langle \mathbf{u}' \rangle^i \langle {}^i C' \rangle^i}}_{=0} + \underbrace{\langle \overline{{}^i\mathbf{u}' \rangle^i \langle C' \rangle^i}}_{=0} \right)
\end{aligned} \tag{5.72}$$

The last two terms on the right of (5.72) are null since $\langle {}^i C' \rangle^i = 0$ and $\langle {}^i\mathbf{u}' \rangle^i = 0$. In addition, the following physical significance can be inferred to the two remaining terms, which were fully commented upon in [15] and for that they will be just listed:

I. Generation/destruction rate of turbulence energy due to macroscopic concentration fluctuations,
II. Generation/destruction rate due to turbulent concentration dispersion.

A model for (5.72) is still needed in order to solve an equation for $\langle k \rangle i$, which is a necessary information when computing $\mu_{t\phi}$ using (5.37). Consequently, terms I and II above have to be modeled as a function of average concentration, $\langle \bar{C} \rangle^i$. To accomplish this, a gradient type diffusion model is used, in the form,

Buoyancy generation of $\langle k \rangle^i$ due to turbulent salute fluctuations:

$$-\rho\,\beta^k_{C_\phi}\phi\,\mathbf{g}\cdot\overline{\langle\mathbf{u}\rangle^{i'}\langle C\rangle^{i'}} = \rho\,\beta^k_{C_\phi}\phi\,\mathbf{g}\cdot(\mathbf{D}_t\cdot\nabla\langle\bar{C}\rangle^i) \tag{5.73}$$

Buoyancy generation of $\langle k \rangle^i$ due to **turbulent salute dispersion**:

$$-\rho\,\beta^k_{C_\phi}\phi\,\mathbf{g}\cdot\langle\overline{{}^i\mathbf{u}'\,{}^iC'}\rangle^i = \rho\,\beta^k_{C_\phi}\phi\,\mathbf{g}\cdot(\mathbf{D}_{disp,t}\cdot\nabla\langle\bar{C}\rangle^i) \tag{5.74}$$

The buoyancy concentration coefficients seem above, namely $\mathbf{D}_t$ and $\mathbf{D}_{disp,t}$, were used before in (5.63) and (5.64), respectively. Note that the terms given by Eqs. (5.73) and (5.74) arise only if the flow is turbulent and if buoyancy is of importance.

Using then (5.65) the macroscopic buoyancy generation of k due to concentration fluctuations can be modeled as,

$$\begin{aligned} G^i_{\beta_C} &= -\rho\,\beta^k_{C_\phi}\,\phi\,\mathbf{g}\cdot\langle\overline{\mathbf{u}'C'}\rangle^i \\ &= \rho\,\beta^k_{C_\phi}\,\phi\,\mathbf{g}\cdot[(\mathbf{D}_t+\mathbf{D}_{disp,t})\cdot\nabla\langle\overline{C}\rangle^i] \;=\beta^k_{C_\phi}\,\phi\,\frac{\mu_{t_\phi}}{\mathrm{Sc}_{t_\phi}}\mathbf{g}\cdot\nabla\langle\bar{C}\rangle^i \end{aligned} \tag{5.75}$$

where μ_{t_ϕ}, Sc_{t_ϕ} and the two coefficients $\mathbf{D}_t$ and $\mathbf{D}_{disp,t}$ have been defined before.

Final transport equations for $\langle k\rangle^i = \langle\overline{\mathbf{u}'\cdot\mathbf{u}'}\rangle^i/2$ and $\langle\varepsilon\rangle^i = \mu\langle\overline{\nabla\mathbf{u}' : (\nabla\mathbf{u}')^T}\rangle^i\Big/\rho$, in their so-called High Reynolds number form can now include the buoyancy generation terms due to temperature and concentration fluctuations as,

$$\rho\nabla\cdot(\bar{\mathbf{u}}_D\langle k\rangle^i) = \nabla\cdot\left[\left(\mu+\frac{\mu_{t_\phi}}{\sigma_k}\right)\nabla(\phi\langle k\rangle^i)\right] + P^i + G^i + G^i_\beta + G^i_{\beta_C} - \rho\phi\langle\varepsilon\rangle^i \tag{5.76}$$

$$\begin{aligned} \rho\nabla\cdot(\bar{\mathbf{u}}_D\langle\varepsilon\rangle^i) &= \nabla\cdot\left[\left(\mu+\frac{\mu_{t_\phi}}{\sigma_\varepsilon}\right)\nabla(\phi\langle\varepsilon\rangle^i)\right] \\ &+ \frac{\langle\varepsilon\rangle^i}{\langle k\rangle^i}\left[c_1P^i + c_2G^i + c_1c_3(G^i_\beta + G^i_{\beta_C}) - c_2\rho\phi\langle\varepsilon\rangle^i\right] \end{aligned} \tag{5.77}$$

where, $\sigma_k = 1$, $\sigma_\varepsilon = 1.3$, $c_1 = 1.44$, $c_2 = 1.92$, $c_\mu = 0.09$ and $c_k = 0.28$ are non-dimensional constants (see [15]). The production terms have the following physical significance

1. $P^i = -\rho\langle\overline{\mathbf{u}'\mathbf{u}'}\rangle^i : \nabla\bar{\mathbf{u}}_D$ is the production rate of $\langle k\rangle^i$ due to gradients of $\bar{\mathbf{u}}_D$;
2. $G^i = c_k\rho\frac{\phi\langle k\rangle^i|\bar{\mathbf{u}}_D|}{\sqrt{K}}$ is the generation rate of the intrinsic average of $\langle k\rangle^i$ due to the action of the porous matrix;

3. $G_{\beta}^{i} = \beta_{\phi}^{k} \phi \frac{\mu_{t_\phi}}{\mathrm{Pr}_{t_\phi}} \mathbf{g} \cdot \nabla \langle \bar{T}_f \rangle^{i}$ is the generation of $\langle k \rangle^{i}$ due to mean temperature variation within the fluid, and
4. $G_{\beta_C}^{i} = \beta_{C_\phi}^{k} \phi \frac{\mu_{t_\phi}}{\mathrm{Sc}_{t_\phi}} \mathbf{g} \cdot \nabla \langle \bar{C} \rangle^{i}$ is the generation of $\langle k \rangle^{i}$ due to concentration gradients.

5.9 Chapter Summary

In this work, equations were derived for turbulent double-diffusive natural convection in porous media. Derivations were carried out under the light of the double decomposition concept [15]. Extra terms appearing in the equations needed to be modeled in terms of $\bar{\mathbf{u}}_D$, $\langle \bar{T}_f \rangle$ and $\langle \bar{C} \rangle$. Here, two different models were combined in order to broaden the ability to analyze more complex flow systems. The first model dealt with characterizing turbulent double-diffusive mechanism but was limited to situations were the so-called thermal equilibrium between phases applied [15]. In addition, the second description of turbulent flow in porous media made no consideration about buoyancy effects but was able to handle situations where the difference in both the fluid and the solid material was considerable [16]. By combining the two models in one single mathematical characterization, the work herein aims at extending the tool described in detail in [15] to solve an ever-broader range of practical problems in engineering.

References

1. Nithiarasu P, Sundararajan T, Seetharamu KN (1997) Double-diffusive natural convection in a fluid saturated porous cavity with a freely convecting wall. Int Commun Heat Mass Transf 24 (8):1121
2. Mamou M, Vasseur P, Bilgen E (1995) Multiple solutions for double-diffusive convection in a vertical porous enclosure. Int J Heat Mass Transf 38(10):1787
3. Goyeau B, Songbe J-P, Gobin D (1996) Numerical study of double-diffusive natural convection in a porous cavity using the Darcy-Brinkman formulation. Int J Heat Mass Transf 39(7):1363
4. Mohamad AA, Bennacer R (2002) Double diffusion natural convection in an enclosure filled with saturated porous medium subjected to cross gradients; stably stratified fluid. Int J Heat Mass Transf 45(18):3725
5. Bennacer R, Beji H, Mohamad AA (2003) Double diffusive convection in a vertical enclosure inserted with two saturated porous layers confining a fluid layer. Int J Therm Sci 42(2):141
6. Mamou M, Hasnaoui M, Amahmida A, Vasseur P (1998) Stability analysis of double diffusive convection in a vertical brinkman porous enclosure. Int Commun Heat Mass Transf 25(4):491
7. Bennacer R, Tobbal A, Beji H, Vasseur P (2001) Double diffusive convection in a vertical enclosure filled with anisotropic porous media. Int J Therm Sci 40(1):30
8. Moukalled F, Darwish M (2013) Double diffusive natural convection in a porous rhombic annulus. Numer Heat Transf Part A 64(5):378–399

9. Khadiri A, Amahmid A, Hasnaoui M, Rtibi A (2010) Soret effect on double-diffusive convection in a square porous cavity heated and salted, from below. Numer Heat Transf Part A, 57(1 I):848–868
10. Hsu CT, Cheng P (1990) Thermal dispersion in a porous medium. Int J Heat Mass Transf 33:1587
11. Bear J (1972) Dynamics of fluids in porous media. Dover, New York
12. Bear J, Bachmat Y (1967) A generalized theory on hydrodynamic dispersion in porous media. In: IASH symposium on artificial recharge and management of aquifers, P. N. 72. Haifa, pp 7–16
13. Whitaker S (1966) Equations of motion in porous media. Chem Eng Sci 21:291
14. Whitaker S (1967) Diffusion and dispersion in porous media. J Am Inst Chem Eng 3(13):420
15. de Lemos MJS (2012) Turbulence in porous media: modeling and applications, 2nd edn. Elsevier, Amsterdam
16. de Lemos MJS, Tofaneli LA (2004) Modeling of double-diffusive turbulent natural convection in porous media. Int J Heat Mass Transf 47(19–20):4221–4231
17. Saito MB, de Lemos MJS (2010) A macroscopic two-energy equation model for turbulent flow and heat transfer in highly porous media. Int J Heat Mass Transf 53(11–12):2424–2433
18. Slattery JC (1967) Flow of viscoelastic fluids through porous media Adv Chem Eng J 13:1066
19. Whitaker S (1969) Advances in theory of fluid motion in porous media. Indust Eng Chem 61:14
20. Gray WG, Lee PCY (1977) On the theorems for local volume averaging of multiphase system. Int J Multiph Flow 3:333
21. Launder BE, Spalding DB (1974) The numerical computation of turbulent flows. Comput Methods Appl Mech Eng 3:269–289
22. Abe K, Nagano Y, Kondoh T (1992) An improve k-ε model for prediction of turbulent flows with separation and reattachment. Trans JSME 58:3003–3010
23. Wakao N, Kaguei S, Funazkri T (1979) Effect of fluid dispersion coefficients on particle-to-fluid heat transfer coefficients in packed bed. Chem Eng Sci 34:325–336
24. Kuwahara F, Shirota M, Nakayama A (2001) A numerical study of interfacial convective heat transfer coefficient in two-energy equation model for convection in porous media. Int J Heat Mass Transf 44:1153–1159

Chapter 6
Final Remarks

This book presented, in a self-contained fashion, a series of studies on flow and heat transfer in porous media, in which distinct energy balances are considered for the porous matrix and for the permeating fluid. Detailed mathematical modeling was presented considering both volume and time averaging operators simultaneously applied to the governing equations [1–3]. System involving combustion in the gaseous phase [4–6], moving beds [7, 8] and double-diffusion mechanism [9] are analyzed. Numerical results where presented for each case.

A correlation for interstitial heat transfer was obtained by resolving flow and heat transfer at the pore scale. After numerically integrating the distributed results in a unit cell, a macroscopic model considering the Local Thermal Non-Equilibrium hypotheses (**LTNE**) was presented.

Future work may take into consideration practical numerical results using the combination of a two energy equation model including double diffusion effects, which was presented only in theory in Chap. 5. By that, a more complete and more general model would be available contributing to solution of a broader range of problems, in a more realistic fashion, including simulation of modern equipment for gasification of renewable fuels and for advanced materials production. In the end, this book contains the description of a tool that might benefit engineers in developing and designing more efficient thermal equipment.

References

1. Saito MB, de Lemos MJS (2006) A correlation for interfacial heat transfer coefficient for turbulent flow over an array of square rods. J Heat Transf 128:444–452
2. Saito MB, de Lemos MJS (2009) Laminar heat transfer in a porous channel simulated with a two-energy equation model. Int Commun Heat and Mass Transf 36:1002–1007
3. Saito MB, de Lemos MJS (2010) A macroscopic two-energy equation model for turbulent flow and heat transfer in highly porous media. Int J Heat Mass Transf 53(11–12):2424–2433
4. de Lemos MJS (2009) Numerical simulation of turbulent combustion in porous materials. Int Commun Heat Mass Transf 36(10):996–1001
5. Coutinho JEA, de Lemos MJS (2012) Laminar flow with combustion in inert porous media. Int Commun Heat Mass Transf 39:896–903

M.J.S. de Lemos, *Thermal Non-Equilibrium in Heterogeneous Media*,
SpringerBriefs in Computational Mechanics,
DOI 10.1007/978-3-319-14666-9_6

6. de Lemos MJS (2015) Advances in modeling turbulence phenomena in heterogeneous media: reactive systems. In: Vafai K (Org.). Chap. 13 Handbook of porous media, 3rd edn. CRC Press, Taylor & Francis, Boca Raton, pp 471–490
7. Pivem AC, de Lemos MJS (2012) Laminar heat transfer in a moving porous bed reactor simulated with a macroscopic two-energy equation model. Int J Heat Mass Transf 55(7–8):1922–1930
8. Pivem AC, de Lemos MJS (2013) Turbulence modeling in a parallel flow moving porous bed. Int Commun Heat Mass Transf 48(November):1–7
9. de Lemos MJS (2014) Analysis of turbulent double-diffusive free convection in porous media using the two-energy equation model. Int Commun Heat Mass Transf 52:132–139